Fall 1997

Enhanced terahertz pulse generation and detection using electric field singularities in photo-conducting antennas

Yi Cai
New Jersey Institute of Technology

ABSTRACT

ENHANCED TERAHERTZ PULSE GENERATION AND DETECTION USING ELECTRIC FIELD SINGULARITIES IN PHOTO-CONDUCTING ANTENNAS

by
Yi Cai

In recent years, generation of ultra-short electromagnetic pulses with frequency components in the terahertz (THz) range has been achieved by various techniques. Among those different methods, photo-conducting antennas have proven to be the most efficient source of THz radiation. THz spectrometers utilizing such photo-conducting antennas as transmitters and receivers are meanwhile routinely used for spectroscopic studies in the frequency regime between 0.1 to 5THz, which can be covered by neither conventional optical nor microwave spectrometers. However, THz emission power from the existing photo-conducting antenna is not sufficient for many applications (such as electro-optic sampling for real time THz detection and imaging, THz near field spectroscopy, remote chemical sensing, etc.).

This dissertation presents a systematic study of a new family of more efficient THz antennas, ranging from engineering simulation, device fabrication, system characterization and their applications. We, for the first time, have designed the THz dipole antennas with relatively sophisticated shapes to optimize the fringing electric field in the regime where the THz pulse is generated. We demonstrate that this is the most efficient THz emitters, to our knowledge, with a record high THz average power of 2-3μW with mW laser excitation. The previously reported state-of-the-art THz radiation power under similar condition are 38nW [39] and 10nW [25].

ENHANCED TERAHERTZ PULSE GENERATION AND DETECTION USING ELECTRIC FIELD SINGULARITIES IN PHOTO-CONDUCTING ANTENNAS

by
Yi Cai

A Dissertation
Submitted to the Faculty of
New Jersey Institute of Technology
in Partial Fulfillment of the Requirements of the Degree of
Doctor of Philosophy

Department of Electrical and Computer Engineering

January 1998

APPROVAL PAGE

ENHANCED TERAHERTZ PULSE GENERATION AND DETECTION USING ELECTRIC FIELD SINGULARITIES IN PHOTO-CONDUCTING ANTENNAS

Yi Cai

Dr. John F. Federici, Dissertation Advisor — Date
Associate Professor of Physics, NJIT

Dr. Haim Grebel, Co-advisor and Committee Chair — Date
Professor of Electrical and Computer Engineering, NJIT

Dr. Igal Brener, Committee Member — Date
Member of Technical Staff, Bell Laboratories, Murray Hill, NJ

Dr. Ken K. Chin, Committee Member — Date
Professor of Physics, NJIT

Dr. Marek Sosnowski, Committee Member — Date
Associate Professor of Electrical and Computer Engineering, NJIT

Dr. William N. Carr, Committee Member — Date
Professor of Electrical and Computer Engineering, NJIT
Professor of Physics, NJIT

BIOGRAPHYICAL SKETCH

Author: Yi Cai

Degree: Doctor of Philosophy in Electrical Engineering

Date: January 1998

Education:

- Doctor of Philosophy in Electrical Engineering
  New Jersey Institute of Technology, Newark, New Jersey, 1998

- Master of Science in Applied Physics
  New Jersey Institute of Technology, Newark, New Jersey, 1994

- Bachelor of Science in Electrical Engineering
  Beijing University, Beijing, People's Republic of China, 1992

Related Publications:

Y. Cai, I. Brener, J. Lopata, J. Wynn, L. Pfeiffer, and J. Federici,
"Design and Performance of Singular Electric Field Terahertz Photoconducting Antennas", Applied Physics Letters, October 1997.

Y. Cai, I. Brener, J. Lopata, J. Wynn, L. Pfeiffer, and J. Federici,
"Singular Electric Field Terahertz Emitters and Detectors", Trends in Optics and Phtotonics Series, volume 13, pp. 237-240, 1997.

I. Brener, Y. Cai, J. Lopata, J. Wynn, L. Pfeiffer, and J. Federici,
"Singular Electric Field Terahertz Emitters and Detectors", Ultrafast Electronics and Optoelectronics Conference, OSA Technical Digest, p54, Incline Village, Nevada, 1997

I. Brener, Y. Cai, J. Lopata, J. Wynn, L. Pfeiffer, and J. Federici,
"Design and Performance of Singular Electric Field Terahertz Emitters and Detectors", Conference on Lasers and Electro-Optics (CLEO), OSA Technical Digest Series, vol. 11, p66, Baltimore, Maryland (1997)

I. Brener, Q. Wu, Y. Cai, X. C. Zhang, J. Lopata, J. Wynn, L. Pfeiffer, J. Stark, and J. Federici,

"Coherent Terahertz Detection: Free Space Eletric-optic Sampling Versus Antennas Detection", Conference on Lasers and Electro-Optics (CLEO), OSA Technical Digest Series, vol.11, p136, Baltimore, Maryland, 1997

Y. Cai, I. Brener, Q. Wu, X. C. Zhang, J. Lopata, J. Wynn, L. Pfeiffer, J. Stark, and J. Federici,

"Coherent Terahertz Detection: Direct Comparison Between Free Space Electro-Optic Sampling and Antenna Detection ", Applied Physics Letters, (submitted)

S. Hunsche, Y. Cai, I. Brener, M. C. Nuss, J. Wynn, J. Lopata, and L. Pfeiffer,

"Near Field Time-resolved Imaging with Far-infrared Dipole Sources", Conference on Lasers and Electro-Optics (CLEO), San Francisco, California, 1998 (submitted)

This dissertation is dedicated to my beloved wife and parents

ACKNOWLEDGMENT

I would like to express my deepest appreciation to Dr. Igal Brener at Bell Labs Lucent Technologies and Dr. John Federici at NJIT, who not only served as my research supervisors, providing valuable and countless resources, insight, and intuition, but also constantly gave me support, encouragement, and reassurance. Special appreciation is given to Dr. Chin at NJIT for his inspiration, guidance and support through out my entire graduate studies.

Appreciation is also extended to the committee chair Dr. Haim Grebel, and committee members, Dr. William Carr and Dr. Marek Sosnowski for active participation and guidance.

Special thanks to the following five persons at Bell-Labs Lucent Technologies: Dr. J. Lopata, Dr. J. Wynn, Dr. L. Pfeiffer, Dr. S. Hunsche, Dr. M. C. Nuss, and two persons at RPI: Dr. Q. Wu, Dr. X. C. Zhang, for their technical collaboration and co-authoring the publications. Finally, special thank goes to my wife and my parents for their support and encouragement in every aspect.

TABLE OF CONTENTS

Chapter	Page
1. INTRODUCTION	1
1.1 Background Information	1
1.1.1 Importance of Terahertz Spectroscopy and Imaging	1
1.1.2 Typical Terahertz Generation and Detection Systems	4
1.2 A Review on the Techniques of Terahertz Generation and Detection	10
1.2.1 Previous Research	10
1.2.2 Limitations on the Previous Terahertz Generators and Detectors	13
1.3 Scope of Our Research	16
1.3.1 Design, Fabrication and Characterization of More Efficient Terahertz Generators and Detectors	16
1.3.2 New Phenomena Discovered in the New Terahertz Radiation Structures	18
1.3.3 Improvement on the Sensitivity of a Terahertz Spectroscopy Systems	19
1.3.4 Applications of the Improved Terahertz TDS System	21
2. DESIGN APPROACHES OF THE SINGULAR ELECTRIC FIELD TERAHERTZ GENERATORS AND DETECTORS	22
2.1 Theoretical Justifications for the New Terahertz Antenna Designs	22
2.1.1 Current Surge Model	23
2.1.2 Optical Rectification Effect: Second-order-like Nonlinear Optical Process Model	24
2.1.3 Effects of the Photo-Generated Carriers Transient Properties	27
2.1.4 Partial (Nonuniform) Gap Illumination Effect	30
2.2 New Approaches to Optimize the Fringing Electric Field in the Photoconductive Antennas	33
2.2.1 Generate Singular Electric Field By Using Sharp Electrodes and Lateral Offset Dipoles	35
2.2.2 Overcome the Gap Size Saturation Effect of the Terahertz Radiation	45
2.2.3 Dipole Length Optimization	45
2.2.4 The Final Testing Patterns	46
2.3 New Approaches to High Resolution Terahertz Imaging Near Field Terahertz Probes	47

TABLE OF CONTENTS
(Continued)

Chapter	Page
3. FABRICATION OF SINGULAR ELECTRIC FIELD TERAHERTZ ANTENNAS	51
3.1 Semiconductor Material Preparation	51
3.1.1 Low Temperature GaAs Growth and Post Annealing	51
3.1.2 Carrier Life Time and Photo-Conductivity Measurement	52
3.2 Device Fabrication	56
3.2.1 Metal Deposition	56
3.2.2 Packaging and Wiring	57
3.2.3 Silicon Hyperhemispherical Lens	61
4. CHARACTERIZATION OF THE SINGULAR ELECTRIC FIELD TERAHERTZ ANTENNAS	65
4.1 Characterization System Setup with Dual Detection Schemes	65
4.2 Performance Comparison in Terahertz Radiation Power of Various Designs	68
4.3 Calibration of the Absolute Average Terahertz Radiation Power	70
4.4 Performance as Detectors and System Bandwidth Calibration	78
4.5 New Phenomena Discovered in the Characterization of the New Structures	81
4.5.1 Symmetric/Asymmetric Excitation Patterns as a Function of Gap Size	81
4.5.2 Polarization of the THz Radaition as a Function of Emitter Structures	82
4.6 Summary	86
5. IMPROVEMENTS TO THE TERAHERTZ SYSTEMS BY USING SINGULAR ELECTRIC FIELD TERAHERTZ ANTENNAS	87
5.1 High Frequency Modulated Lockin Free Space Electro-optic Sampling: A Real Time Delay Scanning Ultra Wide Band Terahertz Imaging System	88
5.2 Near Field Probes: the Highest Spatial Resolution for Terahertz Imaging	97
5.3 Highest Terahertz Sensitivity in Visible Pump and Terahertz Pump Measurement	108
5.4 Compact Terahertz System Using All Solid State Diode Pumped Laser	110
5.5 Summary	113

TABLE OF CONTENTS
(Continued)

Chapter	Page
6. APPLICATIONS DEMONSTRATIONS	115
6.1 Volatile Organic Chemical Sensors	115
6.2 Photo Induced Conductivity Measurement	120
6.3 Summary	122
7. CONCLUSION REMARKS	123
7.1 Summary of Research Results	123
7.2 Direction for Future Research	126
REFERENCES	129

LIST OF TABLES

Table **Page**

2.1 Dimension information for each electrode structure, and plot range. Note: the bias voltage is scale by the minimal gap size for each design..... 37

2.2 Test Pattern Dimensions..... 47

5.1 Comparison Between Free Space Electro-optic Sampling Versus Photoconducting Antenna Detection..... 96

5.2 THz Photo-conductive Antenna Excitation Efficiency comparison of GaAlAs Diode pumped LiSaF Laser vs. Argon Ion Laser Pumped Ti-Sapphire Laser at Comparable Power..... 112

6.1 VOC emitted during thermoplastics processing and their FIR peak absorption..... 118

LIST OF FIGURES

Figures **Page**

1.1 Schematic diagram of a THz-TDS spectrometer using a femtosecond laser source and photoconductive THz transmitters and receivers..... 5

1.2 a) A photoconductive switch Integrated in a transmission line. Optical pulses are focused onto the gap in the transmission line and inject carriers into the semiconductor, leading to a current transient *J(t)* flowing across the gap in the line. b) Typical current response *J(t)* of a photoconductive switch (on long carrier life time semiconductor) to a short optical excitation pulse. The radiated field is dominated by the rising edge of the photocurrent transient. b) Typical current response *J(t)* of a photoconductive switch (on subpicosecond short carrier life time semiconductor) to a short optical excitation pulse. Both rising and decay edge of the photocurrent transient are relevant to the terahertz radiation. The short lifetime is achieved with high defect density..... 8

1.3 Principle of photoconductive sampling. The photoconductive switch acts as a sampling gate that measures the waveform voltage v(t) within the sampling time τ. By changing the delay between the optical pulse triggering the sampling gate and the waveform, the entire waveform can be mapped out sequentially in time. a) , b) and c) show the sampling at three different delays..... 9

1.4 Optical setup of a THz-TDS spectrometer. The THz radiation is coupled in and out of the photoconducting dipole antenna using substrate lenses, and collimated to a parallel and diffraction-limited beam with off-axis paraboloid mirrors..... 10

1.5 Optical setup of a THz-TDS spectrometer for potentially small samples or T-ray imaging. The THz radiation is coupled in and out of the photoconducting dipole antenna using substrate lenses, and collimated to a parallel and diffraction-limited beam with off-axis paraboloid mirrors. A pair of lenses or paraboloids (dotted box) is used to focus the THz beam to a diffraction-limited spot at the sample..... 11

1.6 Three different substrate lens designs. A) the non-focusing hemispherical design, b) the hyperhemispherical lens, and c) the collimating substrate lens..... 11

1.7 Previous art photoconductive switch terahertz generator and detector designs..... 14

1.8 Schematic diagram of the metal electrodes used in the new THz emitters and detectors..... 18

2.1 Energy-band diagram near a semiconductor surface. The band bending is due to surface depletion field. When electron hole pairs are created by vertical transitions, electrons are accelerated by the surface depletion field that give the terahertz radiation. In the non vertical transition case, the radiation is rooted from the second time derivative of the instantaneous polarization..... 25

LIST OF FIGURES
(Continued)

Chapter **Page**

2.2 Sketch of sample and measurement setup for nonuniform gap illumination with the numerical model reported by Zhou. The simulation region is the cross section at the excitation spot shown by the enclosed box..... 33

2.3 Electrode designs investigated by electrostatic electric field simulation. The text is served as a label for each structure. The dimension including the width and height for each triangular tip is listed in Table.2.1..... 36

2.4 Two dimensional electric field mapping for structure U1. One singular field region is created near every corner of the rectangular electrodes..... 38

2.5 Two dimensional electric field mapping for structure A1. One singular field region is created near the tip of the triangle anode, and two smaller singular field regions close to the rectangular corners..... 39

2.6 Two dimensional electric field mapping for structure A_A1. One singular field extreme is created near the triangular tip near the anode and as well as the cathode..... 40

2.7 Two dimensional electric field mapping for structure A_A2. One singular field extreme is created near the triangular tip near the anode and as well as the cathode. The extreme field is slightly stronger and spreading in a larger area than that of A_A1 due to the lateral offset..... 41

2.8 A schematic diagram of the test patterns for the new terahertz emitter and detector designs..... 45

2.9 Three new designes of near-field terahertz probes: a) Integrated Backside Aperture (IBSA) integrates the aperture for near field imaging on the THz photoconductive antenna; b) Thin Wafer No Aperture (TWNA) using a 100μm thin wafer to reduce the distance between the short antenna and sample for near-field operation. c) using SOS substrate to enable Backside Optical Excitation (BSOE) to reduce the distance between the antenna and the sample..... 50

3.1 Theory of time-resolved reflectivity measurement..... 53

3.2 Time-resolved reflectivity measurement setup..... 54

3.3 Time resolved reflectivity transients of low temperature grown GaAs depends on annealing time (2-minute and 5-minute). The long tail make the photoconductive switch takes longer to shut off..... 55

3.4 Time resolved reflectivity transients of low temperature grown GaAs exhibits a overshooting behavior that also makes a switch shuts off slowly..... 55

LIST OF FIGURES
(Continued)

Chapter **Page**

3.5 Time resolved reflectivity transients of low temperature grown GaAs with subpicosecond response. The optimal the material growth preparation condition is found to be 300°C and 1 minute rapid thermal annealing at 600°C, for the fastest photo-response (0.25ps)..... 56

3.6 A schematic diagram of the test patterns for the new terahertz emitter and detector designs..... 58

3.7 Three new designs of near-field terahertz probes: a) Integrated Backside Aperture (IBSA) integrates the aperture for near field imaging on the THz photoconductive antenna; b) Thin Wafer No Aperture (TWNA) using a 100μm thin wafer to reduce the distance between the short antenna and sample for near-field operation. c) using SOS substrate to enable Backside Optical Excitation (BSOE) to reduce the distance between the antenna and the sample..... 59

3.8 Package diagram. a) Top view of a package in a half IC chip carriers, the antenna stick out of the chip carrier; b) Side view of a antenna with a Si lens attached on the back; c) Top view of a package in a whole IC chip carriers, the antenna in placed in the center of the hole on the chip carrier..... 60

3.9 Better support for near field substrate using backside bonding..... 61

3.10 A simplified schematic diagram of the operation of the substrate lens, when the substrate is made of the same material of the lens..... 62

3.11 The lens is used together with a paraboloid mirror to collect and collimate terahertz radiation out of the emitter, and focus the terahertz beam on to the detector..... 63

3.12 a) Si hyperhemispherical lens design for GaAs wafer (account for the difference in refractive indexes) b) The final dimensions of the lens..... 63

4.1 Experimental setup for the characterization of terahertz generation and detection using photoconductive antennas with scanning capabilities on the emitter side..... 66

4.2 Experimental setup: (a) free space electro-optic sampling; (b) photoconductive antenna. In both cases the THz source is a singular electric field emitter with 20mW pump and 40V bias (~80μA)..... 67

4.3 THz radiation power as a function of dipole structures measured in a 60μm dipole, 5μm gap, under 20V bias and 20mW excitation. Shown in the inset is a schematic diagram of the metal electrodes used in the new THz emitters and detectors..... 70

LIST OF FIGURES
(Continued)

Chapter **Page**

4.4 (a) peak THz field as a function of dipole length and gap distance with a fixed bias of 60V and 5mW excitation. The slope of this dependence varies with dipole length, but not electrode shape; The solid lines are fits to the experimental data; (b) a typical THz transient and spectrum when both emitter and detector have offset sharp shapes (TT0, 60μm long and 20μm wide dipole with 5μm gap)..... 71

4.5 Operation principle of a electro-optic crystal: (a) the polarization of the incoming light remains unchanged through the unbiased EO crystal; (b) the polarization of the incoming light is rotated through the EO electrically biased EO crystal..... 75

4.6 Operation principle of a free space electro-optic sampling for terahertz detection: (a) the polarization of the incoming light remains unchanged through the unbiased EO crystal, and therefore no current flow in the balanced diode pair; (b) the polarization of the incoming light is rotated through the terahertz transient biased EO crystal, therefore light intensities on the diode pair are different. Current follow detected which indicting the presence of the terahertz signal..... 76

4.7 The THz signal detected using (a) offset dipole singular electric field detector; (b) regular dipole detector. The offset singular detector yields ~40% improvement over the regular dipole already using its singularity at the edge of the electrode..... 79

4.8 Comparison of time and frequency domain of the terahertz waveforms for (a) antenna detection with a 75μm LT GaAs dipole; (b) free space eletrio-optic smapling detection with a ZnTe crystal. A *60μm* dipole singular electric field emitter with a 5μm gap, under 40V DC bias and 20mW optical excitation, is used as the THz source..... 80

4.9 Two dimensional scans of the THz emission intensity from several singular electric field offset dipole emitters with gaps of (a) 5, (b) 10, (c) 30, (d) 90μm. The small-gap emitters in (a) and (b) show perfectly symmetrical THz emission; the 30μm gap emitter (c) shows a slight asymmetry, and the THz emission from large gap emitters (d) is clearly asymmetrical, enhanced near the anode..... 83

4.10 A comparison of the polarization of the THz emission from stripline, conventional dipole and offset dipole emitters. The percentage of the lateral electric field is relative to the vertical electric field in each structure. The difference is related to the direction of the carriers' flow in the semiconductor. It indicates that the THz generation in biased photoconducting antennas is determined to a large extent by carrier dynamics rather than nonlinear effects..... 84

LIST OF FIGURES
(Continued)

Chapter **Page**

4.11 The polarization of the THz emission from stripline and offset dipole emitters is related to the directions of the carriers' flow in the semiconductor. The THz radiation from the offset dipole has a considerable (~25%) orthogonal component..... 85

5.1 Experimental setup: (a) free space electro-optic sampling; (b) photoconductive antenna. In both cases the THz source is a singular electric field emitter with 20mW pump and 40V bias (~80μA photo current)..... 89

5.2 Comparison of time and frequency domain of the terahertz waveforms for (a) antenna detection with a 75μm LT GaAs dipole; (b) free space eletrio-optic smapling detection with a ZnTe crystal. A *60μm* dipole singular electric field emitter with a 5μm gap, under 40V DC bias and 20mW optical excitation, is used as the THz source..... 91

5.3 Comparison of time and frequency domain of the terahertz waveforms for (a) antenna detection with a 75μm LT GaAs dipole; (b) free space eletrio-optic smapling detection with a ZnTe crystal. A *45μm* dipole singular electric field emitter with a 5μm gap, under 40V DC bias and 20mW optical excitation, is used as the THz source..... 93

5.4 Experimental setup using mixer based MHz chopping and fast phase sensitive detection for real time free space electro-optic sampling. The frequency synthesizer generates two synchronized frequency at 0.9MHz and 0.9007MHz. The AOM modulate the pump beam at 0.9MHz. The lockin amplifier is referenced at the difference of the two frequencies through RF mixing, and operates at a low time constant ≤1ms. The real time waveform is captured on an oscilloscope. This radio frequency narrow band detection method can eliminate the 1/f low frequency noises and achieve shot noise limited detection..... 95

5.5 Three new designs of near-field terahertz probes: a) Integrated Backside Aperture (IBSA) integrates the aperture for near field imaging on the THz photoconductive antenna; b) Thin Wafer No Aperture (TWNA) using a 100μm thin wafer to reduce the distance between the short antenna and sample for near-field operation. c) using SOS substrate to enable Backside Optical Excitation (BSOE) to reduce the distance between the antenna and the sample..... 99

5.6 An image of a razor blade taken with conventional terahertz antenna probe made on a regular 500μm thick wafer. A strong frequency dependence on the image resolution is illustrated. Only above 1.25 THz, the image of the blade becomes clear but still limited by diffraction. Image obtained at lower frequency is hampered by the diffraction pattern. A spatial resolution of about 400 μm has been achieved at frequency above 1.25 THz..... 103

LIST OF FIGURES
(Continued)

Chapter **Page**

5.7 An image of a 50μm gold wire taken with TWNA near-field probe. A strong frequency dependence on the image resolution is illustrated. A spatial resolution of less than 100 μm has been achieved at frequency 1 THz..... 104

5.8 A pulse delay caused by diffraction: The thin wafer no aperture (TWNA) emitter is used. Terahertz transient obtained in 1-D scan with a razor blade is presented in 3-D and 2D. The dipole antenna is placed almost in contact with the sample. The THz pulse delay increases with the progressive intrusion of a razor blade sample. Terahertz transient obtained in 1-D scan with a razor blade is presented in 3-D and 2D..... 105

5.9 The ultimate spatial resolution is obtained with the IBSA structures using a pin hole. The probe (60μm long dipole with a 10μm gap in the middle) is fabricated on a 100μm thin wafer with a 25 μm × 25 μm aquare aperture on the back aligned with the front side emitter. An shown in Fig.5.2.5, a spatial resolution of <50 μm is achieved..... 106

5.10 Two lines scans (vertical and horizontal respectively) with SOS emitter using backside excitation. The dipole antenna is placed almost in contact with the sample. Terahertz transient obtained in 1-D scan with a razor blade is presented in 3-D and 2D. In the 3-D plot, the x direction is scanning direction, y axis is time, and z axis is terahertz transient field intensity. The spatial resolution is better when the polarization is parallel to the edge..... 107

5.11 Experimental setup for visible pump and terahertz probe experiment for extremely dilute photo generated carrier density..... 109

5.12 Terahertz transient waveforms and spectrums obtained from the same pair of photoconductive antennas excited by argon ion laser pumped Ti:sapphire mode-locked laser and diode pump Cr:LiSaF laser under comparable laser power. The time constant is 100ms for both waveforms..... 112

6.1 Terahertz waveform and spectrum through free space and empty VOC cell with quartz widows. The bandwidth is reduced because of the high frequency cut of quart..... 117

6.2 Terahertz waveform and spectrum through a 54mm and a 139mm VOC cell filled with saturated acetone gas at room temperature..... 118

6.3 Terahertz absorption spectrum through a 54mm and a 139mm VOC cell filled with saturated acetone gas at room temperature, normalized by the background spectrum. a) is in logarithmic scale and b) in linear scale..... 119

LIST OF FIGURES
(Continued)

Chapter **Page**

6.4 Signal obtained while the visible beam pumping the SI-GaAs is chopped for lockin detection, therefore the measured signal strength is the indication of the photo-generated carrier density. The photo-excited carrier density in the semi-insulating SI-GaAs is estimated to be ~$3*10^{13}$ cm^{-3}..... 121

7.1 Conceptual integration of terahertz antennas with fiber optics..... 128

CHAPTER 1

INTRODUCTION

In this chapter we introduce some background information, including the significance of terahertz spectroscopy and typical terahertz generation and detection systems. We make a brief review of the previous research in terahertz generation and its applications, and then briefly introduce the research work we have done in improving the terahertz system performance.

1.1 Background Information

1.1.1 Importance of Terahertz Spectroscopy and Imaging

Continued progress in novel semiconductor materials has led to the fabrication of electronic devices with intrinsic speeds of a few picoseconds, and we can expect that sub-picosecond electronic device will soon be possible. The development of high-speed electronic material techniques is consequently very important to characterize these devices and to understand the physical principles of the materials and structures that are used to make them.

In recent years, generation of ultra-short electromagnetic pulses with frequency components in the terahertz (also known as far infra-red) range has been achieved by various techniques. Among those different methods, photo-conducting antennas have proven to be the most efficient source of terahertz radiation. [18,23,25] Terahertz spectrometers utilizing such photo-conducting antennas as transmitters and receivers are

meanwhile routinely used for spectroscopic studies in the frequency regime between 0.1 to 5THz which can be covered by neither conventional optical nor microwave spectrometers.

The terahertz, or far-infrared, region of the electromagnetic spectrum is of critical importance in the spectroscopy of condensed matter systems. The electronic properties of semiconductors and metals are greatly influenced by bound states whose energies are resonant with terahertz photons. The terahertz regime also coincides with the rates of inelastic processes in solids, such as tunneling and quasiparticle scattering. As a final example, confinement energies in artificial synthesized nanostructures, like quantum wells and micro cavities, lie in the terahertz regime.

In spite of its importance, terahertz spectroscopy has been hindered by the lack of suitable tools. Swept-frequency synthesizers for millimeter- and submillimeter-waves are limited to below roughly 100GHz, with higher frequencies only available using discrete frequency sources. Fourier transform infrared (FTIR) spectroscopy, on the other hand, is hampered by the lack of brightness of incoherent sources. In addition, FTIR methods are not useful if the real and imaginary part of response functions must be measured at each frequency.

Terahertz Time-Domain Spectroscopy (THz-TDS) is a new spectroscopic technique that overcomes these difficulties in a radical way. Its advantages have resulted in rapid proliferation within the last few years from a handful of ultrafast laser experts to researchers in a wide range of disciplines. THz-TDS is based on electromagnetic transients generated opto-electronically with the help of femtosecond duration laser pulses. These THz transients are single-cycle bursts of electromagnetic radiation of typically less than 1ps duration. Their spectral density spans the range from below 100GHz to more than

5THz. Optically gated detection allows direct measurement of the terahertz electric field with a time resolution of a fraction of a picosecond. From this measurement both the real and imaginary part of the dielectric function of a medium may be extracted, without having to resort to Kramers-Kronig relations. Furthermore, the brightness of the THz transients exceeds that of conventional thermal sources, and the gated detection is orders of magnitude more sensitive than bolometric detection.

THz pulse devices operating in the 10^{10}Hz to 10^{13}Hz frequency regime have been described in various forms. These pulsed devices have been used in time resolved infrared spectroscopy to characterize a variety of properties of solid state materials such as refractive index, photoconductivity, absorption, and dispersion.

Recent developments have shown that THz-TDS has capabilities that go far beyond linear far-infrared spectroscopy. Because the THz transients are perfectly time-synchronized with the optical pulses that generate them, THz-TDS is ideally suited for "visible-pump, THz-probe" experiments. In these measurements, the optical pulse is used to optically excite a sample and the THz pulse probes the change in dielectric function (or conductivity) as a function of time after optical excitation. Another powerful nonlinear technique is the detection of THz emission following pulsed laser excitation. In many cases, these nonlinear techniques are proving even more powerful than linear THz-TDS spectroscopy and yield complementary information that maybe otherwise difficult to obtain.

Beyond the characterization of new materials and the study of basic physical phenomena, the impact of THz spectroscopy in the commercial world is growing. More recently, significant applications in optical imaging have become practical.[26] Terahertz

imaging (T-ray imaging) shows promise in a variety of analytical imaging applications such as chemical mapping, and a host of commercial applications such as safe package inspection, industrial process control, food inspection, biology and medicine. The T-ray imaging is a good candidate to replace X-ray imaging in many areas because of its safety. As radiation sensors, these devices are effective for analysis of solids, liquids or gases. Analysis of gases is particularly effective since gases have characteristically strong absorption lines in the THz frequency range. Accordingly, these devices can be used effectively for environmental studies and environmental monitoring. Use of these devices for ultrafast pulse generation and detection in digital data communications is also envisioned.

1.1.2 Typical Terahertz Generation and Detection in Spectroscopic Systems

Figure 1.1 is a schematic diagram of a terahertz generation and detection system for terahertz time domain spectrometer applications. It consists of a femtosecond laser source (1), a beam spliter that divides the laser beam into two, an optically gated terahertz transmitter (2), focusing and collimating optics (3), the sample under investigation (4), an optically-gated terahertz detector (5), a variable delay line (6) that varies the optical delay between the pulses gating the transmitter and detector, a current amplifier (7), and a lockin amplifier (8). A computer (9) controls the variable delay line and displays the detector photocurrent versus path length. The function of each of these components is discussed in the following paragraphs.

In the past, only dye lasers were capable of generating optical pulses of roughly 100fs duration. [1] Today, solid-state lasers like the Ti:sapphire laser [2] [3], delivering

pulses with a wavelength near 800nm, have largely displaced dye lasers and are commercially availiable. The typical repetition rate of these lasers is about 100 MHz. Not more than 10-50mW of laser power is required for either THz transmitter or detector. In the foreseeable future, progress in diode-pumped solid-state laser sources [4] [5] [6] will make femtosecond lasers more practical, compact, and cost effective. Recent developments promise that a complete THz time-domain spectrometer will soon fit into a smaller box than a commercial FTIR spectrometer.

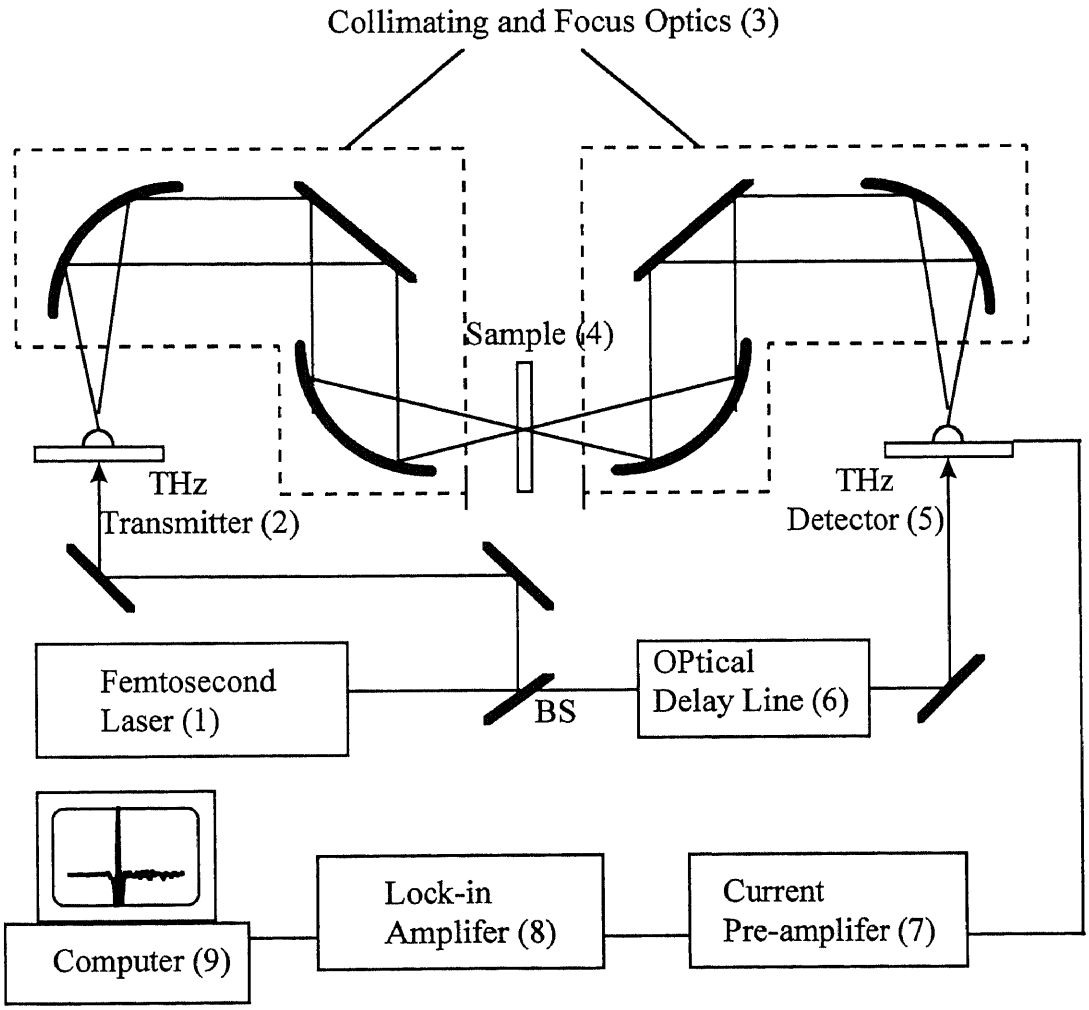

Fig.1.1 Schematic diagram of a THz-TDS spectrometer using a femtosecond laser source and photoconductive THz transmitters and receivers.

The truly elegant aspect of the THz time-domain linear spectrometer is that the sources and detectors consist of the same building block. Both are based on the photoconductive switch [7] [8] on a semiconductor substrate (Fig.1.2a). The response of the voltage-biased photoconductive switch to a short optical pulse focused onto the gap between the two contacts is illustrated in Fig.1.2b for long lifetime materials and Fig.1.2c for short lifetime materials. The current through the switch rises very rapidly after injection of photocarriers by the optical pulse, and then decays with a time constant given by the carrier lifetime of the semiconductor. The transient photocurrent J(t) induces THz radiation into free space according to Maxwell's equations, $E(t) \propto \partial J(t)/\partial t$. Because of the time derivative, the radiated field in long lifetime semiconductor material is dominated by the rising edge of the photocurrent transient, which is invariably much faster than the decay. Long tails of the photocurrent decay are largely irrelevant to the radiated field. But in the subpicosecond lifetime ultrafast semiconductors, both the rising and decay edges contribute to the terahertz radiation. Such materials, including low temperature GaAs and radiation damaged silicon on sapphires (SOS), are the most efficient photoconducting materials for terahertz radiation.

To convert the potoconductive switch for use as a detector of short electrical pulses, an current ammeter (in experimental setup a current-to-voltage transimpedance amplifier) is connected across the photoconductor, replacing the transmitter voltage bias. The electric field of an incident THz pulse now provides the driving field for the photocarriers. Current flows through the switch only when both the THz field and photocarriers are present. Since electronics is not fast enough to measure the THz transients directly, repetitive photoconductive sampling is used (Fig.1.3). If the

photocarrier lifetime, τ is much shorter than the THz pulse, the photoconductive switch acts as a sampling gate which samples the THz field within a time τ. Because the laser pulses which trigger the transmitter and gate the detector originate from the same source, the photoconductive gate can be moved across the THz waveform with an optical delay line (Fig.1.1). Using this technique, the entire THz transient is mapped without the need for fast electronics.

To perform spectroscopic measurements, the THz transmitter and receiver are incorporated into an optical system. The optical system must guide the radiation from source to detector, and focus the radiation to a diffraction limited spot on a potentially small sample. Such an optical system is shown in Fig.1.4. Off-axis paraboloid mirrors are used to collimate and focus the THz radiation. In the system shown in Fig.1.4, the full emission angle of the terahertz radiation emerging from the hyperhemispherical substrate lenses is about 30 degrees. Using off-axis paraboloids with 6.6cm focal length, the far-infrared radiation is collimated to a parallel, Gaussian beam of roughly 25mm diameter. This beam can be focused to a diffraction-limited spot size of 0.5mm at a peak frequency of 1THz by inserting a pair of focusing lenses or off-axis paraboloids into the system (Fig.1.5).

Although the paraboloids are somewhat difficult to align, they offer high reflectivity and achromatic operation over the entire THz range. As an alternative, fused quartz lenses may be used at frequencies below 1THz, and silicon lenses up to 10THz. Unfortunately, optical alignment with visible laser beams is impossible with fused quartz lenses because the refractive index is very different at visible and THz frequencies. Another useful lens material is TPX (poly-4-methyl-pentene-1), a polymer which has low

absorption and dispersion throughout the THz range [9], but is difficult to polish because of its softness. Some groups have dispensed with optics beyond the substrate lens and use large diameter (25mm) substrate lenses of the design shown in Fig.1.6c to form a collimated beam. [10]

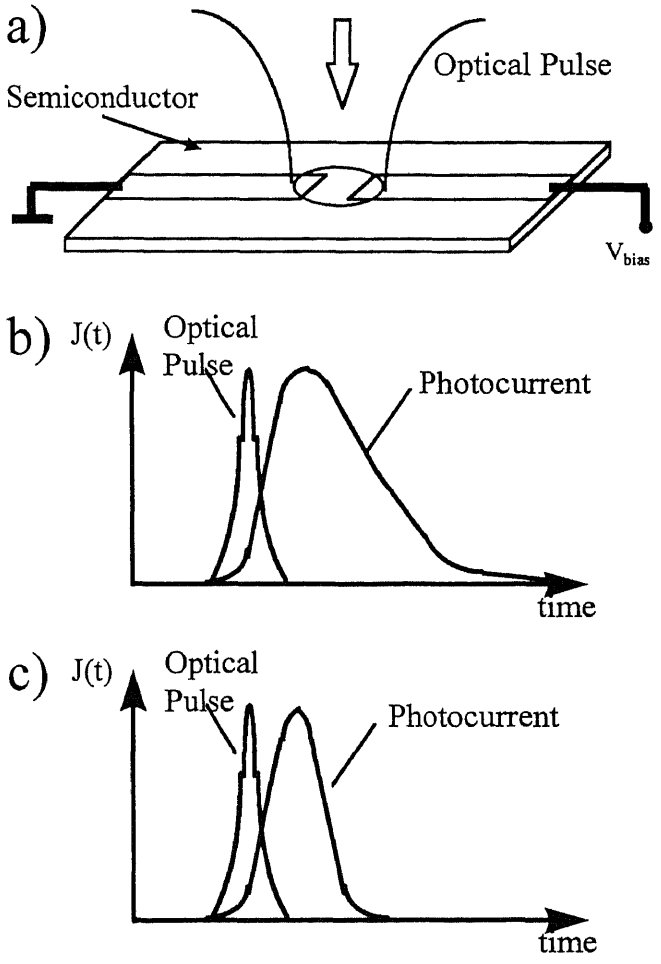

Fig.1.2 a) A photoconductive switch integrated in a transmission line. Optical pulses are focused onto the gap in the transmission line and inject carriers into the semiconductor, leading to a current transient *J(t)* flowing across the gap in the line. b) Typical current response *J(t)* of a photoconductive switch (on long carrier life time semiconductor) to a short optical excitation pulse. The radiated field is dominated by the rising edge of the photocurrent transient. c) Typical current response *J(t)* of a photoconductive switch (on subpicosecond short carrier life time semiconductor) to a short optical excitation pulse. Both rising and decay edge of the photocurrent transient are relevant to the terahertz radiation. The short lifetime is achieved with high defect density.

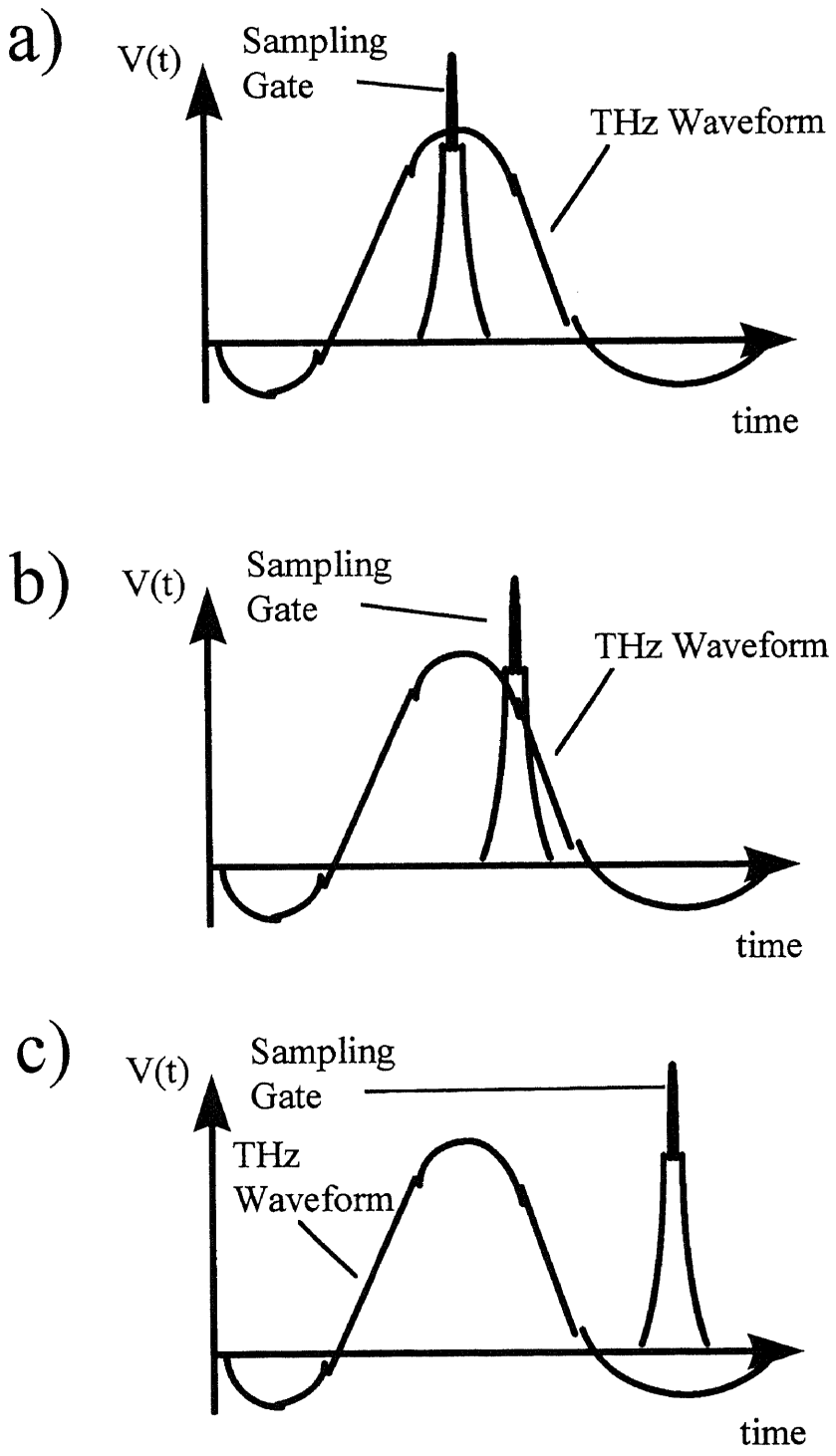

Fig.1.3 Principle of photoconductive sampling. The photoconductive switch acts as a sampling gate that measures the waveform voltage v(t) within the sampling time τ. By changing the delay between the optical pulse triggering the sampling gate and the waveform, the entire waveform can be mapped out sequentially in time. a) , b) and c) show the sampling at three different delays.

1.2 A Review on the Techniques of Terahertz Generation and Detection

1.2.1 Previous Research

THz-TDS is barely 16 years old. Unlike other spectroscopic techniques that have evolved more incrementally, we can clearly identify the technological breakthroughs that have enabled the technique to flourish. Femtosecond laser sources have become widely available commercially within the last few years and can now be operated by a relative novice in laser technology. Developments in materials, such as low-temperature GaAs, electro-optic crystals, *etc.*, have helped to unify optics and electronics. Advances in microelectronics allow the fabrication of micro optoelectronic devices without loss of bandwidth.

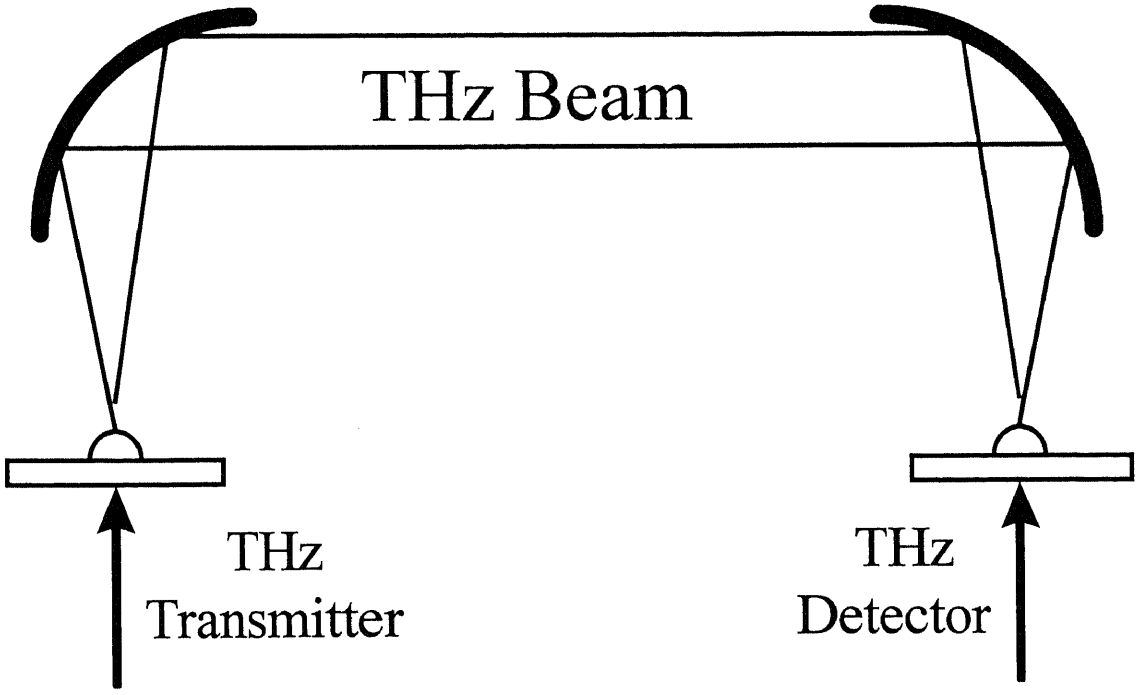

Fig.1.4 Optical setup of a THz-TDS spectrometer. The THz radiation is coupled in and out of the photoconducting dipole antenna using substrate lenses, and collimated to a parallel and diffraction-limited beam with off-axis paraboloid mirrors.

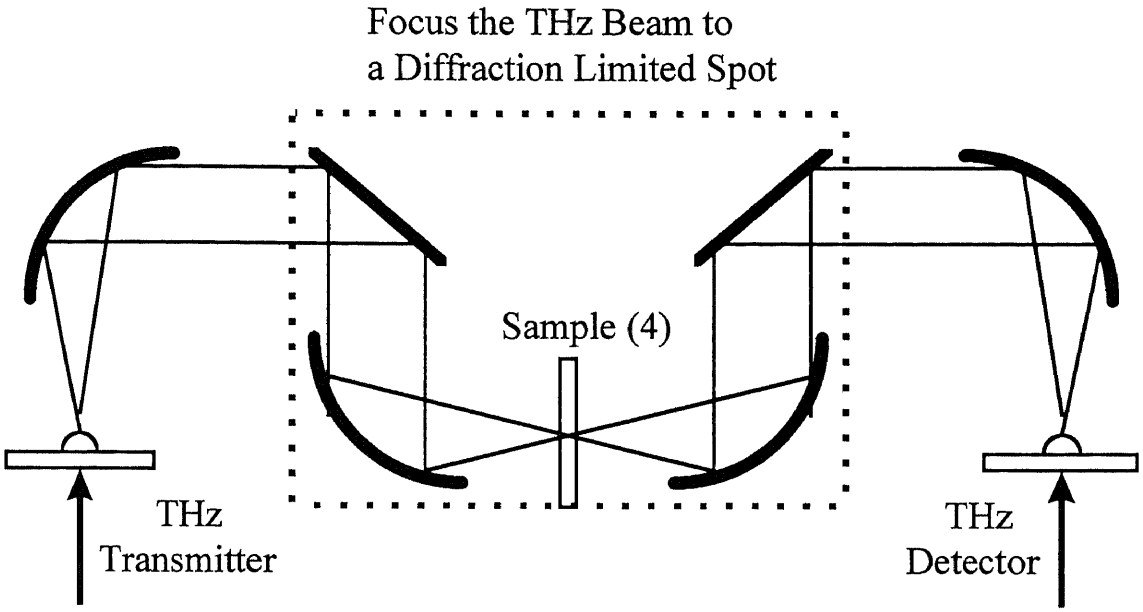

Fig.1.5 Optical setup of a THz-TDS spectrometer for potentially small samples or T-ray imaging. The THz radiation is coupled in and out of the photoconducting dipole antenna using substrate lenses, and collimated to a parallel and diffraction-limited beam with off-axis paraboloid mirrors. A pair of lenses or paraboloids (dotted box) is used to focus the THz beam to a diffraction-limited spot at the sample.

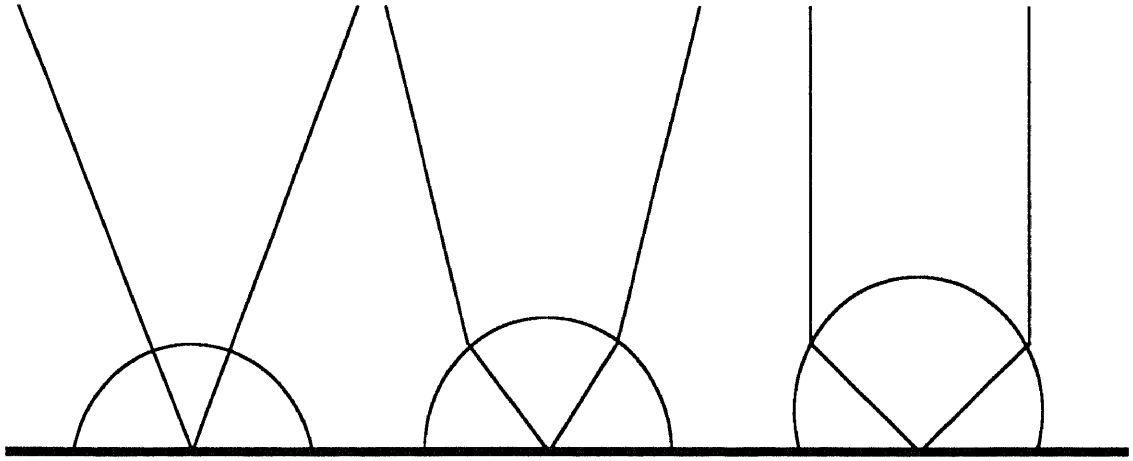

Fig.1.6 Three different substrate lens designs. A) the non-focusing hemispherical design, b) the hyperhemispherical lens, and c) the collimating substrate lens.

The union of these enabling optical and electronic technologies is commonly referred to as "ultrafast optoelectronics" by D. H. Auston. [11] The historical development of THz-TDS is intimately tied to that of ultrafast optoelectronics. Initially, electrical pulses were generated and detected on transmission lines using photoconductors excited by laser pulses. [12] Picosecond microwave pulses in free space were first generated by coupling these electrical pulses to a microwave antenna. [13] Simultaneously with the development of shorter and shorter laser pulses, advances in VLSI lithographic techniques allowed fabrication of smaller radiating structures and consequently higher frequency electromagnetic radiation. [14] [15] [16] This development culminated in the generation of terahertz band width single-cycle pulses by photoconducting dipole antennas in the late 80s. [17] [18] A breakthrough came with the addition of substrate lenses to couple the radiation in and out the photoconducting dipole chip more directionally and efficiently. [19] This opened the way to "Terahertz Beams" [20], which could be collimated and focused as easily as light beams in a spectrometer.

It is interesting to note that prior to the development of THz bandwidth photoconductive dipole antennas, THz electromagnetic transients were generated by optical rectification in electro-optic crystals like $LiTaO_3$, which also allowed for simultaneous electro-optic detection of the transients in the same crystal [21] [22] [23]. Because of the difficulty in coupling the THz radiation in and out of the electro-optic crystals, this technique has now been displaced by the photoconductive antenna approach.

1.2.2 Limitations on the Previous Terahertz Generators and Detectors

The original design of the terahertz generator and detector is described by Smith et al, "Subpicosecond photoconducting dipole antennas", IEEE Journal of Quantum Electronics, vol. 24, pp. 255-260, 1988. The device uses a coplanar stripline terminating in a dipole antenna consisting of a small electrode gap formed over radiation damaged silicon on sapphire as shown in Fig.1.7a. The electrode gap produces the high field photoconductor region. The pump beam was a mode locked dye laser pumped with an argon laser and operating with a pulse duration of 120fs at 620nm. The gap forming the high field region is rectangular shaped, and so is the gap. Smith et al used an optical pump spot of 6μm focused on a 5μm gap.

Another terahertz device is described by Van Exter et al [24]. Van Exter et al describe a device that uses a dipole antenna formed in the middle portion of a stripline as shown in Fig.1.7b. The substrate forming the photoconductive region in their device is also silicon on sapphire and they also use a colliding-pulse mode-locked dye laser as the pump source. The electrode gap in the Van Exter et al device is a conventional slot with a rectangular shape, and the spot of the optical pump is focused on two edges of the rectangular gap.

A somewhat more recent analysis of these devices is given by Ralph et al [25]. Ralph et al analyzed the effect of the semiconductor properties on the electric field profile between the electrodes forming the gap. They found that semi-insulating semiconductors produce enhanced field profiles. The desired semi-insulating property may be obtained through choice of a material with high trap density or traps may be created in a normal semiconductor by ion beam damage. Since the optoelectric interaction that produces the

THz radiation occurs at the semiconductor surface where the trap density at and near the semiconductor surface is controlling, and the ion beam induced traps are at least as effective as material prepared with high trap density. The device of Ralph et al used a semi-insulating substrate (GaAs) and their high field region is formed by relatively widely spaced (80μm) parallel electrode strips. They found a trap enhanced field effect near the anode of the device and only a small part, the enhanced part, of the gap was pumped and thus active as shown in Fig.1.7c. Again the gap of their device is rectangular in shape, and the optical pump spot is incident on one electrode edge of the gap.

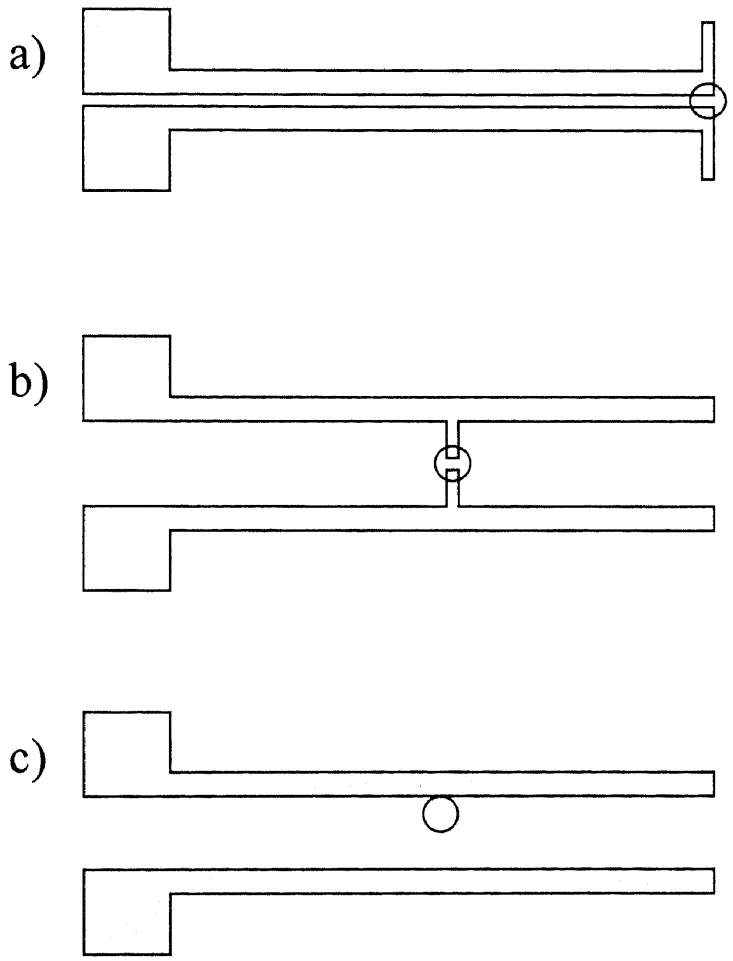

Fig.1.7 Previous photoconductive switch terahertz generator and detector designs.

A very recent development in this technology was the proposal and demonstration of T-ray (terahertz ray) imaging [26]. In this T-ray imaging devcie, the generator is a pair of 50μm spaced parallel striplines, and the detector is an antenna with a 5μm gap on silicon on sapphire (SOS). Because both the generation and detection is optically gated and coherent, this imaging device produces a very high signal to noise ration (SNR) and simplifying the output signal processing with realtime digital signal processing (DSP) card.

The terahertz generator / detector in all of these devices is relatively simple in structure. Basically they are comprise of a semiconductor substrate with electrodes on the substrate and a small gap in between the electrodes. With an appropriate DC bias applied to the electrodes a field is established across the gap which produces a small high field photoconductor region at the surface of the semiconductor in the electrode gap. When this region is excited by fast pulses of light, very rapid changes in conductivity occur. In the presence of the DC electric field these changes in conductivity result in ultrafast pulses of electric current, and ultrafast bursts of electromagnetic radiation are emitted from the gap region. The dipole antenna formed by the metal striplines enhance the terahertz radiation into the free space dramatically. Much of this radiation is emitted into the substrate. But since it has a photon energy well below the direct bandgap of the semiconductor, it can be collected by suitable lens arrangement on the back side of the semiconductor. The radiated beam can be collimated and focused using suitable mirrors, and can be detected by a device operating in a reverse mode to that just described.

Recent studies of these device structures have established that the pulsed laser pump can be replaced with two CW laser signals that are wavelength tuned very slightly

apart. When mixed in the active region of the semiconductor / photoconductor they produce a mixed signal also in the THz range.[]

While advances in these devices have been significant, they still operate with a very low conversion efficiency. The excitation is also limited by device saturation or breakdown. Previously reported THz radiation powers of photoconductive switches are 38nW by M. V. Exter and D. Grischkowsky [39] and 10nW by S. E. Ralph and D. Grischkosky [25]. The power limits the dynamic range, signal to noise ratio, and delectability of these prior art terahertz devices, which makes it extremely difficult to be used in some applications (i.e. conductivity measurements of semi-insulating materials, like semiconductor nano-clusters and conducting polymers), or too slow to be implemented for practical purposes (i.e. T-ray imaging) while maintaining satisfactory signal to noise ratio. That is one of the main reason why the THz system is still one step away from being commercialized. Continued advances in the technology of terahertz generator / detectors requires the conversion process to have improved efficiency.

1.3 Scope of Our Research

1.3.1 Design, Fabrication and Characterization of More Efficient Terahertz Generators and Detectors

We observed that the terahertz generation is to an extent proportional to the DC biased field and laser pumping power in the gap of the terahertz antenna. But the DC bias and the laser pumping is limited by the device breakdown. We also observed the saturation effects on pumping power and DC bias which have been reported by S. E. Ralph and D. Grischkosky [25]. In our typical small gap devices the breakdown threshold is set by the

photo current limit which is directly related to the bias and laser pumping. This result shows that the terahertz radiation power of the conventional devices have reached their limit, and can not be improved simply by increasing the DC bias or laser pumping. New design is required to achieve higher radiation power.

We have analyzed the high field region in the electrode gap of the above described devices and have developed techniques for significantly enhancing the field intensity. We achieve this by introducing localized extreme fields at selected spots in the dipole region. The interaction of these enhanced localized field regions, either singly or preferably when integrated over the whole region, produce a total signal that is greater than that produced by prior devices. The key to producing the local extreme fields is in the electrode structure forming the gap i.e. that shape of the gap, and the position of the optical pump. The boundary of the gap, according to the broadest aspect of our design, has at least one sharp feature, and the pumping laser pulses are directed on that sharp feature. [27] In a preferred form of our design, the boundary of gap has a relatively complex shape in comparison to the prior art gaps shapes, and the optical pump signal is incident on one or more than one sharp features as those shown in Fig.1.8 [28].

Further variations in the geometry, including offset dipole electrodes as structure TT0 and TT45 shown in Fig.1.8, provides an additional dimension of control to the fringing field in the gap. The dipole length and gap size are also optimized to produce the strongest terahertz radiation.

We also observed that a saturation in the THz emission intensity was reached for a given electrode spacing, thus limiting the efficiency of these emitters. In this work we describe more powerful THz emitters and detectors by using new electrode geometries in

the limit of small gaps that optimize the singular electric fields experienced by the photogenerated carriers. We compare the relative THz radiation power of various new dipole designs, and calibrate the absolute average power of the THz beam using free space electro-optic sampling.

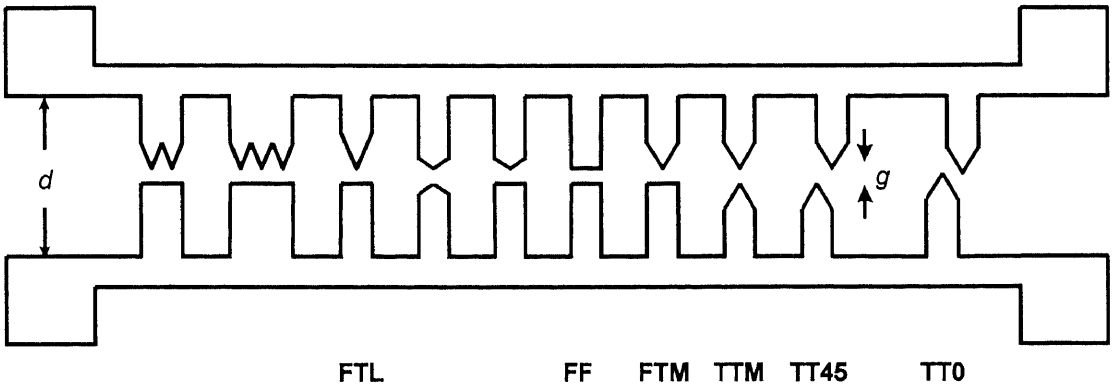

Fig.1.8 Schematic diagram of the metal electrodes used in the new THz emitters and detectors.

We have achieved an average THz radiation power of 3μW under 20mW excitation, calibrated by free space electro-optic sampling. [29] This is the most efficient emitter to our knowledge for excitation power in the mW range. Previously reported THz radiation powers of photoconductive switches are 38nW [39] and 10nW [25]. And we also demonstrated that the antenna when used as detector also outperforms that conventional dipole detectors.

1.3.2 New Phenomena Discovered in the New Terahertz Radiation Structures

Two new phenomena have been observed in terahertz generation in our experiments which provide as much insights as puzzles in terahertz generation mechanism.[30]

We measured the dependence of the polarization of the THz radiation as a function of the offset angle and for different gap sizes. Due to the lateral offset of the electrodes, the carrier transport direction will be different in each structure. We found that the polarization varies in different structures. Since we are the first group using offset dipole structures in terahertz antennas, this is a new phenomena that supports the well known current surge model for terahertz generations at least for resonant antenna structures.

It was previously observed by many groups that the process of THz generation in biased structures (with gaps ranging from several tens of μm to a few cm) becomes particularly efficient when excited close to the anode.[31,32,33,34] This enhancement has been termed the "positive electrode effect" [32] and has been observed by a number of groups both in THz emission [31,32,34] and short electrical pulse generation[33] and in different semiconductors.[31,32,33,34,36]. However, a symmetrical THz emission intensity was reported for very large gap (3cm) structures.[35] The two-dimensional scans of the THz emission in our small gap structures also show an absence of this asymmetry, but our large gap structures show a clear asymmetry. This gap size dependence is a very interesting new phenomena, and can not be explained by any existing theories.

1.3.3 Improvement on the Sensitivity of a Terahertz Spectroscopy Systems

With the these new state of the art powerful terahertz generators and detectors, combined with other new techniques borrowed from optical systems, we improved not only the conventional photoconductive antenna based terahertz spectroscopic system, but also the new free space electro-optic crystal detector based systems.

Free space electro-optic sampling is a new detection method for terahertz detection [25]. It has a much wider bandwidth (up to 3-7 THz) than photoconductive antenna detectors (up to 2-3 THz), as the electro-optic crystal sensor is not restricted by the photoconductive dipole antenna response. But the trade-off is that its signal to noise ratio (SNR) which is not as good as that of using photoconductive dipole antenna sensors. We compare the use of free space electro-optic sampling (FSEOS) with that of photoconductive antennas for terahertz detection. [40]. A dual detection system also allows us to calibrate the power emitted from singular electric-field emitters. Using our powerful emitters that produce an average power of 3μW, combined with 1MHz radio frequency modulation and very small time constant in the lock-in amplifier, we demonstrate the significantly improved SNR and the feasibility of terahertz (T-ray) imaging using real time delay scanning with free space electro-optic sampling.

Similarly, we have improved the traditional photoconductive dipole antenna based terahertz system with our powerful THz generator and detector, combined with fast (100KHz) modulation, fast current pre-amplifier, and lock-in detection. We achieved a record high signal to noise ratio of nearly 10^6 when using a 300ms time constant on the lock-in amplifier. This advance makes the photoconductive measurement at extremely dilute photo-excitation densities ($<10^{14}cm^{-3}$) and ultra short lifetime (<400fs) possible. For example, terahertz spectroscopy enabled the measurement of the conductivity of nano-cluster thin films – the conventional approach of using metal contacts could not be used in this case. This is a very important non-contact approach for characterizing the ultrafast dynamics of semiconductor materials. This advance can also be used to increase the terahertz (T-ray) imaging speed. Because of the ultra high SNR of the system, the time

constant for the lock-in detection of each pixel can be reduced with the same image quality.

1.3.4 Applications of the Improved Terahertz TDS System

In the last chapter, we demonstrate several applications empowered by this record high sensitivity, including chemical sensing, real time THz imaging with wide band electro-optic crystal THz sensors, photo induced conductivity measurement of Si nano-structure thin film, and semi-insulating GaAs.

We will present the proposal and demonstration of a terahertz airborne organic chemical sensor. The improved terahertz spectrometer is a good candidate to replace the FTIR systems to provide low-cost, compact and in-situ detection of chemicals in the air.

A demonstration of photoconductive characterization of materials with extremely dilute photo-excitation densities ($\sim 10^{14} cm^{-3}$), low carrier mobility, or ultra short lifetime (~400fs) is another aspect of application discussed in the last chapter. As examples, the photo-conductivity measurement of silicon nano-cluster thin films and semi-insulating GaAs are presented. This is a very important non-contact approach for characterizing the ultrafast dynamics of semiconductor materials.

CHAPTER 2

DESIGN APPROACHES OF THE SINGULAR ELECTRIC FIELD TERAHERTZ GENERATORS AND DETECTORS

The design of optimum emitters requires an understanding of the terahertz generation mechanism in a device, and how the terahertz radiation scales with bias field and optical excitation fluence and position (when partial illumination of a transmission line gap is used). Unfortunately, as pointed out by Zhou *et al.* [41,42,43], a rigorous model for this problem should include a simultaneous solution of the Boltzmann transport equation, the Poisson's equation, and the Maxwell curl equations, all in three dimensions, which are exceedingly difficult to model. The many existing models are aimed at the understanding of the physical mechanisms, rather than establishing a quantitatively accurate model. [44] In this chapter we review the research work in terahertz generation theory and numerical modeling. Because of the relatively complex geometry of our device and the current status on the terahertz generation modeling techniques, we only performed a somewhat over simplified electrostatic simulation. Although it can not provide much information on the peak power and bandwidth of our devices, it served as a guideline for the designs of the dipole electrodes.

2.1 Theoretical Justifications for the New Terahertz Antenna Designs

The THz generation mechanism involves a nonlinear optical effect, carrier transportation properties and a effect of electric static fields in semiconductor. There are currently two models for the THz generation at semiconductor surface: current surge model, and second-order-like nonlinear optical process model.

Several numerical models have been reported, and we will introduce some of them in this section. However, an accurate simulation of our current new designs is extremely difficult. According to the recent research work on terahertz generation modeling, some of the difficulties lie in the nature of the carrier's transient behavior in the ultrafast materials. The fact that the device dimension is comparable or even smaller than the radiated wavelength, the three dimensional nature of the problem (not only to account for light penetration, but also the electric field distribution), and partial non-uniform gap illumination further complicate the analysis. As pointed out earlier [41,42,43], a rigorous model for this problem should include a simultaneous solution of the Boltzmann transport equation, the Poisson's equation, and the Maxwell equations, all in three dimensions, which is exceedingly difficult to model. Moreover, the transient parameters for most ultrafast materials are not readily available.

2.1.1 Current Surge Model

A current surge of photo-injected carriers in the surface depletion field, enhanced by external electric field bias, feeds the dipole antenna. The response of the voltage-biased photoconductive switch to a short optical pulse focused onto the gap between the two contacts is illustrated in chapter 1, Fig.1.2b. The current through the switch rises very rapidly after injection of photocarriers by the optical pulse, and then decays with a time constant determined by the carrier lifetime of the semiconductor. The transient photocurrent J(t) radiates into free space according to Maxwell's equations, $E(t) \propto \partial J(t)/\partial t$. The carrier dynamics induce the terahertz radiation. And subsequently, the radiated field feeds into the dipole antenna which helps to couple the wave into free space.

In this model, the optical pulse generates the carriers and the bias applied induces the carrier transport. Therefore, higher electric fields and higher excitation energy densities (increased carrier concentrations) enhance the radiation.

2.1.2 Optical Rectification Effect Second-order-like Nonlinear Optical Process Model

The generation process of picosecond and subpicosecond far infrared (FIR) transients, utilizing photoconductive media coupled to antenna structures, has been explained as Hertian radiation from time-varying electric current surge. Until recently, it has been shown experimentally that ultra short pulses of FIR radiation can also be generated from ultra short optical pulses incident on a semiconductor surface [48,49,50,51]with no external bias or antenna structures. This observation opens up new possibilities for terahertz spectroscopy and characterization of electronic properties of semiconductor surfaces. These studies have culminated in the observation of FIR transients as short as 120 fs by Greene, Federici, Dykaar, Levi, Pfeiffer, Jones, and Bucksbaum in 1991 [50,51]. This phenomena was first explained as an effect remaining in the domain of "current surges" occuring in the surface depletion field [48,49]. In 1992 Chuang, Schmitt-Rink, Greene, Saeta and Levi reexamined this most recent phenomenon in the original context of optical rectification and second-order optical nonlinearities. Their model takes into account both the above band-gap (resonant) nature of the excitation process as well as the presence of a surface depletion field. [52] In so doing, they can satisfactorily explain several experimental observations, most importantly the absolute intensity of the detected light and its dependence on crystallographic orientation.

The phenomenon designated as "optical rectification" or " difference frequency mixing" originates from the experiments using pulsed visible-light sources and electro-optic materials to generate FIR radiation, before the photoconductive antenna is used for FIR radiation.[21] The high excitation of the femto-second laser induced the second-order-like nonlinear optical process. In such materials, the nonlinear interaction between two optical fields produces an electric field at the beat frequency, with the intensity determined by the instantaneous intensity of the optical fields.

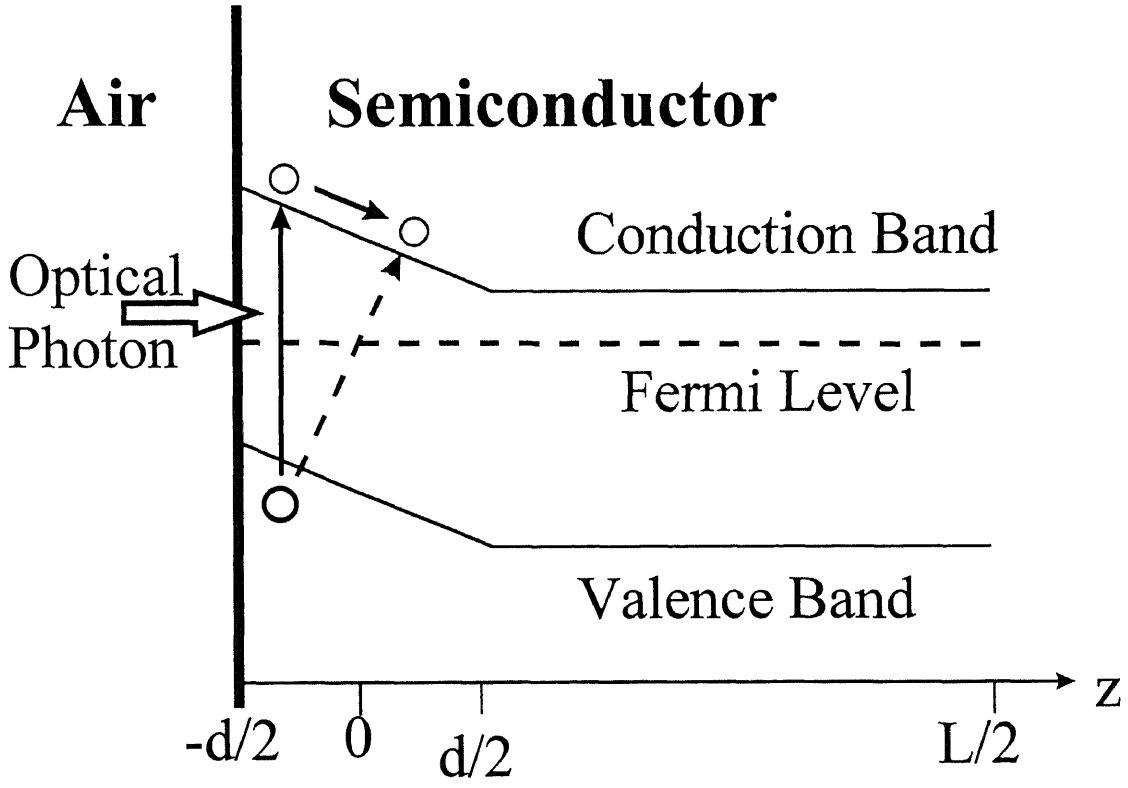

Fig.2.1 Energy-band diagram near a semiconductor surface. The band bending is due to surface depletion field. When electron hole pairs are created by vertical transitions, electrons are accelerated by the surface depletion field that give the terahertz radiation. In the non vertical transition case, the radiation is rooted from the second time derivative of the instantaneous polarization.

Fig.2.1 shows a simple representation of the energy-band extrema of a semiconductor near the surface. In a conventional transport picture one assumes that electron-hole (e-h) pairs are created by vertical transitions in real space with the penetration depth of the incident optical field. Subsequently, as indicated by the solid arrows in Fig.2.1, electrons are accelerated by the surface depletion field, while holes remain confined to the surface. The resulting current surge $\partial J / \partial t$ then gives rise to terahertz radiation, where J is proportional [8,9] to the photoelectron population n and the material mobility μ. However, as indicated by the dashed arrow in Fig.2.1, there exists an alternative non-vertical transitions in real space. Because of spatial separation of final electron and hole states, this process leads to an instantaneous FIR polarization P_0 whose second order time derivative $\partial^2 P_0 / \partial t^2$ determines the radiation signal.

In lowest order in the optical field E_o and neglecting nonlocal effects, the FIR (static) polarization P_o induced perpendicular to the surface may be written as

$$P_o = \chi^{(2)}(0;-\omega, \omega) |E_o|^2$$

where $\chi^{(2)}$ is the second-order nonlinear optical susceptibility. Usually, the latter quantity is strictly equal to zero in systems with inversion symmetry, such as semiconductors with diamond structure. However, the surface depletion field breaks this symmetry and makes $\chi^{(2)}$ nonzero over the depletion width. The most striking evidence for the $\chi^{(2)}$ process is a strong modulation of the detected terahertz intensity from the unbiased semiconductor wafer as the sample is rotated about its surface normal. The calculated values of $\chi^{(3)}$ between 10^{-6} and 10^{-5} esu [52], depending on the detailed doping parameters, lead to terahertz field strengths on the order of 10 V/cm, assuming as incident optical power density of approximately 10^3 W/cm^2. Therefore, it is not negligible even in small gap

photoconductive antennas. In order to establish an accurate terahertz radiation estimate, both current surge contribution and optical rectification contributions have to be included. We will discuss the current surge model for our partially illuminated gap later in this section.

In summary, in this model the radiation originates from the polarization P, because we can always write the radiation field as the first time derivative of a current $J=dP/dt$ or the second time derivative of a polarization. Since $P_o=\chi^{(2)}E_o(\omega_1)E_o(\omega_2)$ and $\chi^{(2)}=\chi^{(3)}E_s$, the nonlinear effect is proportional to the electric field E_s and optical excitation field E_o. In conclusion, higher electric field and higher excitation enhance the radiation.

Apparently higher electrical field can be achieved by higher bias, but it may increase the current which produces more Johnson noise. Most importantly, the dielectric breakdown of the photoconductive switch sets the limit on the bias field strength. The optical excitation level is also limited by semiconductor material saturation and damage threshold. That justifies our attempt to create very high electric field only in a localized region and lower the field intensity in the adjacent regions to avoid breakdown. Naturally this suggests the use of partially illuminating the gap. We will discuss the effect of this nonuniform illumination later in this chapter.

2.1.3 Effects of the Photo-Generated Carriers Transient Properties

Theoretical modeling of terahertz radiation from large aperture, biased photoconductors has to be performed in the near and far fields, assuming a current-surge mechanism (as opposed to a nonlinear-optical mechanism). In most of these calculations the carriers instantaneously acquire their final velocity after photoexcitation instead of accelerating to

a saturation velocity in a finite time. Since optical pulse widths used for terahertz generation experiments (100fs) are shorter than acceleration times in typical photoconductors such as GaAs, [26] we expect transient carrier velocity effects to be important in the the terahertz generation process.

The effort of transient carrier velocity dynamics in modeling the far field terahertz radiation from a large-aperture biased photoconductor triggered by an ultra short optical pulse has been reported by Rodrigues *et al.* [45] in 1995. In this work, the geometry used in this calculation is as follows: a photoconductor is biased with a uniform electric field E_b across a gap spacing L (not applicable in our design), thereby defining an optically excited area A in the x-y plane. The emitter is excited at normal incidence (z direction) by an above-band-gap pulse with an intensity profile $I_{opt}(t)$. The gap spacing is assumed to be larger than the radiated wavelength (not applicable in our design). The transmitted radiation is detected on axis, a distance z away from the emitter, where z is in the far field. It was found that, when the optical pulse width is shorter than the acceleration time, the radiated pulse width is much longer than the optical pulses, and saturation occurs at lower optical fluence. That explains the observed broadening of the terahertz waveforms with respect to the optical pulse as well as the observed difference in saturation fluence as the optical excitation energy is varied. [50,51]

The transient velocity effect suggests that a material with short acceleration time will not only produce shorter terahertz pulses, but also higher optical fluence saturation level. Obviously, a higher electrical bias field and carrier mobility will reduce the carrier acceleration time.

But on the other hand, in order to increase the bias without breakdown, a high resistivity photoconductor is desired. Short carrier lifetime is also essential for the photoconductive switch to turn on and off ultrafast to produce the ultra short current surge. The response of the voltage-biased photoconductive switch to a short optical pulse focused onto the gap between the two contacts is illustrated in chapter one Fig.1.2b for long lifetime materials and Fig.1.2c for short lifetime materials. The current through the switch rises very rapidly after injection of photocarriers by the optical pulse, and then decays with a time constant given by the carrier lifetime of the semiconductor. The transient photocurrent J(t) radiates into free space according to Maxwell's equations, $E(t) \propto \partial J(t)/\partial t$. Because of the time derivative, in long lifetime semiconductor material, the radiated field is dominated by the rising edge of the photocurrent transient, which is invariably much faster than the decay. Long tails of the photocurrent decay are largely irrelevant to the radiated field. But in the subpicosecond lifetime ultrafast semiconductors, both the rising and decay edges contribute to the terahertz radiation. Such materials, including low temperature GaAs, InP and radiation damaged silicon on sapphire (SOS), are the very efficient photoconducting materials for terahertz radiation. Short life time is also the determining factor for the detection bandwidth, when the antenna is used as detector.

Obviously, there must be a trade off in the acceleration time and lifetime (defect density). In our case, we use low temperature GaAs. By controlling the growth temperature and post annealing time, we can achieve the best trade off.

2.1.4 Partial (Nonuniform) Gap Illumination Effect

Ultrashort (subpicosecond) electrical pulse generation by partial illumination of a transmission-line gap has attracted a lot of interest since the first experimental work of Krokel *et al.* [32]. Most recently, it has been demonstrated by Brener *et al.* [31] that proper partial gap illumination can improve the terahertz radiation efficiency over the full-gap photoexcitation. The first theoretical understanding of the mechanism of this pulse generation technique was first proposed by Sano and Shibata [36] based on full-wave analysis [47], who attributed the phenomenon to the displacement current due to modified-field distribution. A recent Monte Carlo investigation of the intrinsic mechanism of this short-pulse production by Zhou et al. [41], [42] confirmed the above theory of photocarrier-induced field redistribution from first principles. The above two theories explained the observed ultrafast electrical pulses with the interrogation of the transient electric field distribution, although from different prospective. The major difference between the two models is that the three-dimensional (3-D) full-wave analysis accounts for pulse propagation but simplifies carrier transport using the drift-diffusion approximation; while the one-dimensional (1-D) Monte Carlo model solves the transport problem from first principles but neglects light penetration as well as pulse dispersion effects. One common aspect that was not accounted for by both theories, however, is the strong pulse amplitude dependence on the excitation location [31,32,46] which influences the efficiency of pulse generation. This dependence has been thoroughly studied experimentally [46] by a complete spatial mapping of the electrical transient across the gap. The effect of non-uniform initial field distribution has has been examined by Ralph and Grischkowsky [25] based on a two dimensional (2-D) numerical simulation, and they

attributed the enhanced ultrafast terahertz radiation to the trap-enhanced electric field at the anode. Another model is proposed by Zhou [44], emphasizing the effect of the nonlinear initial field distribution on the generated electrical pulse, which has been ignored in other theories. One major approximation in this model is the macroscopic modeling of carrier transport, which uses a field-dependent mobility to model high-field transport. This work is a 2-D model with simple transmission line structures, as shown in Fig.2.2. The simulation region is the cross section at the plane of the photoexcitation. The author used the MEDICI device simulator from Technology Modeling Associates, Inc. The physical models are based on the drift-diffusion equations implemented in MEDICI, in conjunction with the current continuity equations and the Poisson's equation

$$\varepsilon \nabla^2 \psi = -q\,(p - n + N_D^+ - N_A^-)$$

$$\partial n/\partial t = q^{-1}\,\nabla \bullet \mathbf{J}_n - U_n + G_n$$

$$\partial p/\partial t = -q^{-1}\,\nabla \bullet \mathbf{J}_p - U_p + G_p$$

$$\mathbf{J}_n = q\,\mu_n\,n\,\mathbf{E} + q\,D_n\,\nabla n$$

$$\mathbf{J}_p = q\,\mu_p\,p\,\mathbf{E} - q\,D_p\,\nabla p$$

where the symbols have their familiar meanings. The photo-generation rate is expressed in terms of the photon flux Φ and the absorption coefficient α

$$G = \Phi\,\alpha\,\exp\{-\alpha y\}\,\exp\{-(x-x_0)^2/\sigma_x^2\}\,\exp\{-(t-t_0)^2/\sigma_t^2\}$$

where the first exponential term represents the radial dependence of the beam, which is centered at $x = x_{x0}$ with a diameter D related to σ_x as

$$\sigma_x = D/2\sqrt{2}$$

This term models the non-uniform shape of the excitation beam in the z direction, although it is based on a 2-D simulator. The third exponential term describes the temporal

shape of the optical pulse where t_0 is the time at which the optical power peaks, and σ_t is related to the pulse width t_w FWHM (full-width at half maximum) as

$$\sigma_t = t_w / 2\sqrt{\ln 2}$$

The following empirical expressions are used for the absorption coefficient:

$$\alpha = (10^{3-2.8\lambda}) / 10 \qquad \text{(for GaAs)}$$

$$\alpha = 10^{1.73-3.45\lambda} \qquad \text{(for Si)}$$

where α in μm^{-1} and λ in μm. The substrate is uniformly doped p-type with a concentration N_{sub}. The two electrodes are assumed to be Schottky contacts with a work function of 4.67 eV. Concentration-dependent Schockley-Read-Hall (SRH) and Auger recombination are included. Field-dependent mobility models for Si and GaAs are used to model high-field transport effects. For all the simulations, the author use a optical width t_w = 140 fs, and it peaks at t_0 = 300 fs. The wavelength assumed to be λ = 620 nm by Zhou *et al.*[12].

Actually, all the theoretical work mentioned above uses simple transmission line geometry without dipole antenna structures, and did not include the optical rectification effect. However, the debate between the current surge model and the nonlinear optical rectification model is gradually winding down with a consensus that both effects contribute to the terahertz generation. Needless to say, further research work is necessary before a device simulation tool can handle our relatively complex structures (plus antennas responses for various shaped dipoles).

Based on existing theories of 3-D full-wave analysis, 1-D Monte Carlo model, and 2-D numerical simulation as well as the experimental data, it is recognized that the major effect on the physical mechanism is the transient field redistribution or space charge

redistribution across the gap as well as light penetration into the substrate. It should be emphasized that these existing theories are all aimed at the understanding of the physical mechanisms of non-uniform gap illumination, rather than establishing a quantitatively accurate model.

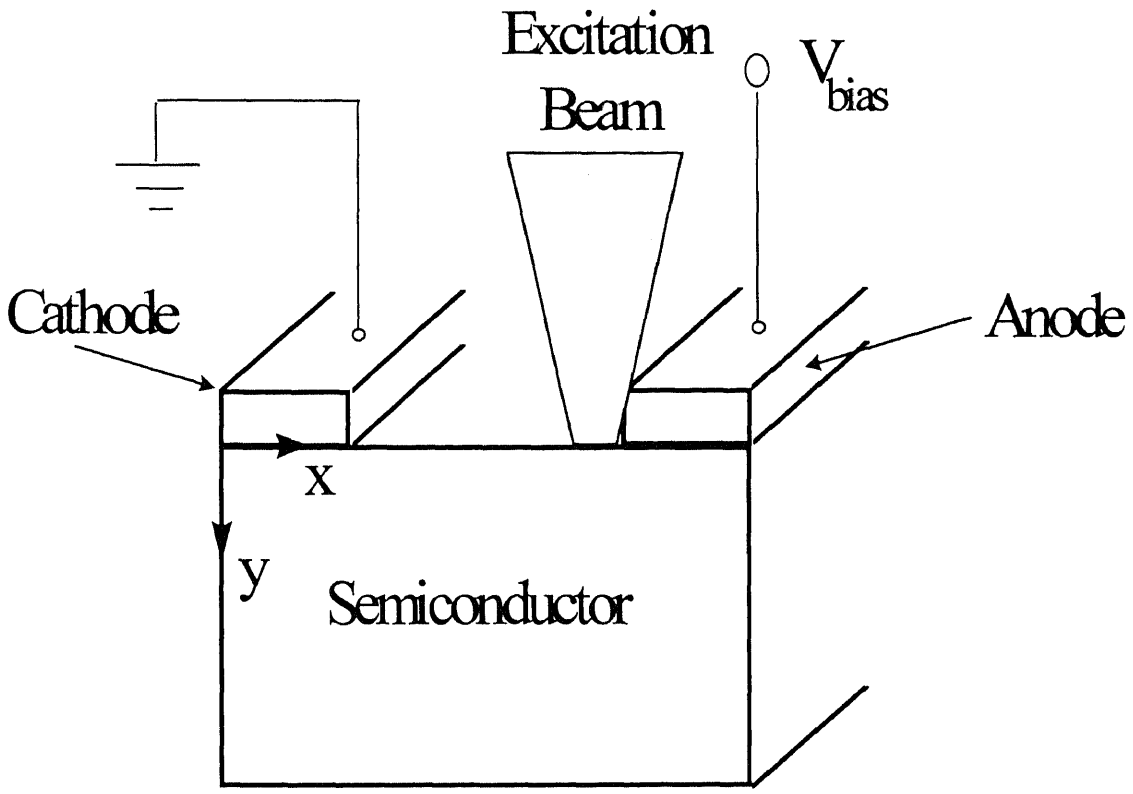

Fig.2.2 Sketch of sample and measurement setup for nonuniform gap illumination with the numerical model reported by Zhou.

2.2 New Approaches to Optimize the Fringing Electric Field in the Photoconductive Antennas

Our idea to enhance the THz radiation is to create a local high electric field regime using triangular tips. The peak value and the spreading of the high field regime depends on the shape of the antenna and the proper positioning of the positive and negative electrodes. When the optical excitation is focused onto this high field regime near the positive

electrode, stronger radiation is expected. Since the electric field is only very high in a small regime like a singularity, the current will not increase dramatically. Therefore, a high power low noise emitter can be achieved.

In summary of the previous section, it has been shown that partial illumination can improve the terahertz radiation efficiency. This enhancement is a result of transient electric field redistribution or space charge redistribution, regardless of which mechanism is responsible for this redistribution phenomena. The key feature of this redistribution is the creation of a region with the transient electric field higher than normal (if the electric fields were uniform within the gap). A localized high field results from transients can enhance the terahertz radiation, we can certainly incorporate a localized static high field region for the same purpose. Our way to achieve that is by using sharp electrodes. Although the absolute field distribution will be changed by the carrier's screening, and trapped charge redistribution, this change can be used to our favor by a geometry effect. For example, by making the anode a sharp triangle, we create a singular electric field region next to the anode tip. When we use partial gap illumination to excite this singular field region, the transient field redistribution further enhance the electric field. With the combined enhancements, a extremely high field is created in a localized region. The redistribution will reduce the field intensity in other areas, such as near the cathode. This can not be achieved by increasing the electrostatic bias in a simple shaped transmissions line antennas. Due to the lack of localization, the electric field in the whole gap rise up resulting in a breakdown at a much lower bias level.

2.2.1 Generate Singular Electric Field by Using Sharp Electrodes and Lateral Offset Dipoles

We have analyzed the high field region in the electrode gap of the previously described devices and have developed techniques for significantly enhancing the field intensity. We achieve this by inducing localized extreme field concentrations at selected spots in the dipole regions. The interaction of these enhanced localized extreme field region, produces a total signal that is greater than that produced by prior devices. The key to producing the local extreme field is in the electrode structure forming the gap i.e. the shape of the gap, and the position of the optical pump. The boundary of the gap has at least one sharp feature, and the pump signal is directed at that sharp feature. In a preferred form of this design, the boundary of the gap has a relatively complex shape in comparison to the prior art gaps shapes, and the optical pump signal is incident on one or preferably more than one sharp feature. The term complex is a comparative term and is intended to define any shape that has more sides than a rectangle. While in normal practice, the sides will be straight, combinations of straight and curved sides can be envisioned.

The most straightforward and thus likely implementation will have one or more sharp features on the gap edge of the anode, the cathode, or both. The sharp features in the electrode gap concentrate the field lines at the apex of the angle and result in increased effectiveness of terahertz generation / detection when the optical pump signal is made incident on one or more of these sharp features. In the broadest sense of our design, the electrode gap geometry is either rectangular or triangular and optical pump beam is incident on at least one apex of the geometry.

The term sharp feature, for the purpose of this description means an angle of less than 135 degrees. The angle that constitutes the sharp feature may be the angle found in a normal polygon or may be a re-entrant angle.

The effectiveness of various electrode designs to maximize the electric fringing field, designated as "singular electric field", were studied. Fig.2.3 illustrates the studied structures. The results shown are electrostatic simulations. Although it may over simplify the problem, it provides a starting point for our design. In most cases, the results qualitatively predicted the terahertz radiation efficiency. In all the simulations the bias voltage is scaled to the minimal gap distance to yield a comparable electric field intensity results for all structures.

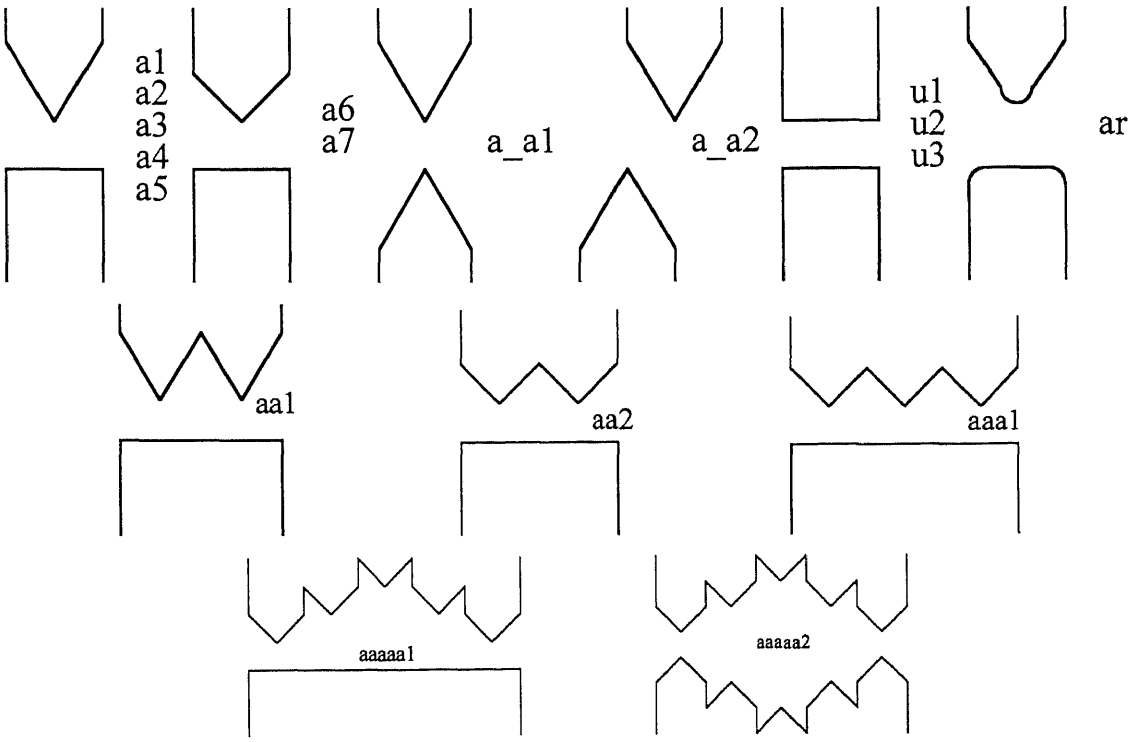

Fig.2.3 Electrode designs investigated by electrostatic electric field simulation. The text is served as a label for each structure. The dimension including the width and height for each triangular tip is listed in Table.2.1.

Table.2.1 Dimension information for each electrode structure, and plot range. Note: the bias voltage is scaled by the minimum gap size for each design.

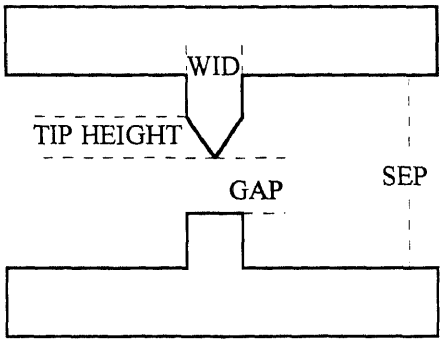

TYPE	FILE	GAP (um)	WID (um)	SEP (um)	RANGE (um*um)	TIP HEIGHT (um)
one tip	A1	5	10	30	30*40	9
	A2	20	10	45	45*40	9
	A3	40	10	65	65*40	9
	A4	60	10	85	85*40	9
	A5	100	10	110	110*40	9
	A6	5	10	30	30*40	5
	A7	20	10	45	45*40	5
0.3um round Corner	AR	5	10	30	30*40	9
one tip on each side	A_A1	5	10	30	30*40	9
	A_A1	5	10	30	30*40	9
two tips (offset)	AA1	20	20	45	45*40	9
	AA2	20	20	45	45*40	5
three tips	AAA1	20	30	45	45*40	5
five tips	AAAAA1	20,25,30,25,20		50	65 65*60	10
	AAAAA2	10,20,30,20,20		50	65 65*60	10
flat end	U1	5	20	30	30*40	---
	U2	5	20	50	50*40	---
	U3	5	20	70	70*40	---

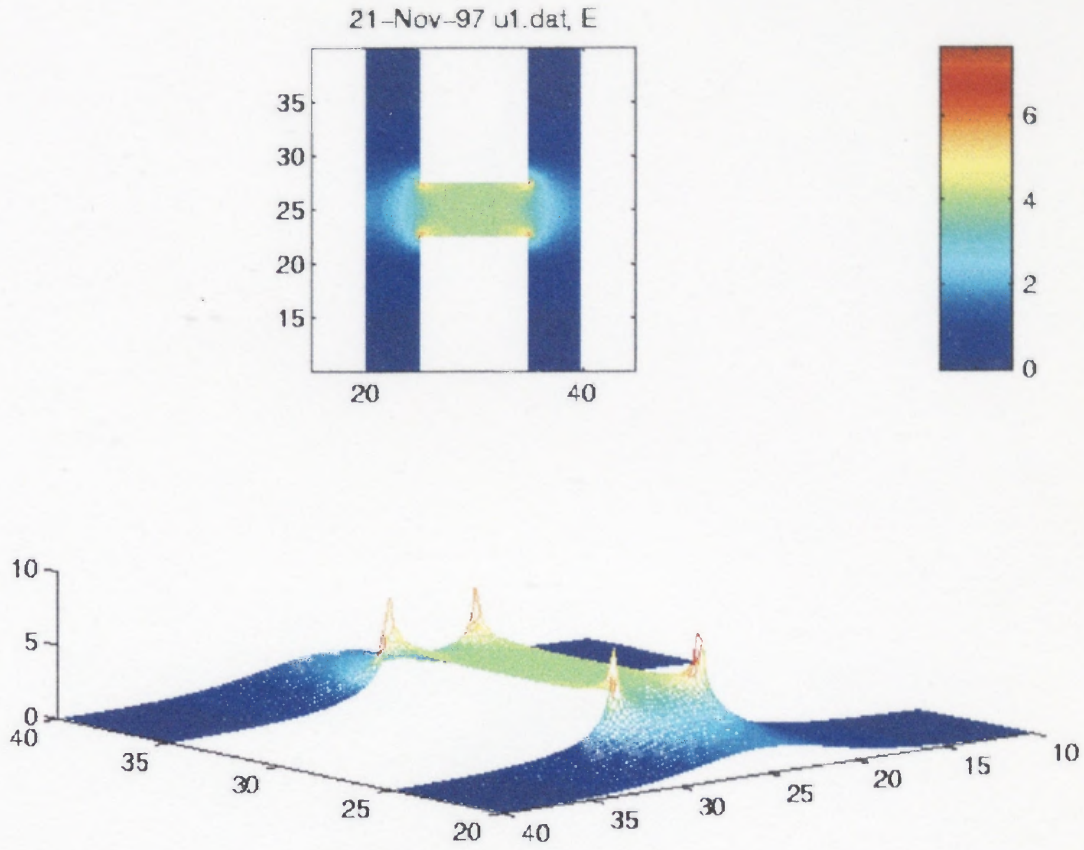

Fig.2.4 Two dimensional electric field mapping for structure U1. One singular field region is created near every corner of the rectangular electrodes.

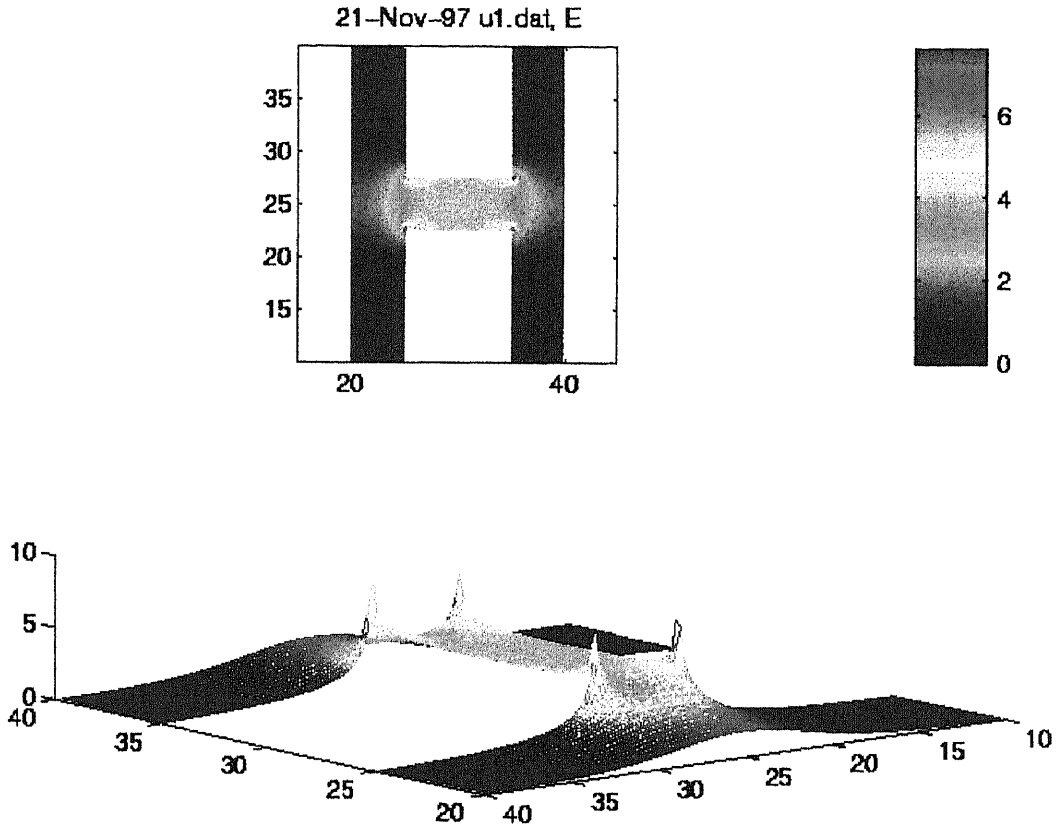

Fig.2.4 Two dimensional electric field mapping for structure U1. One singular field region is created near every corner of the rectangular electrodes.

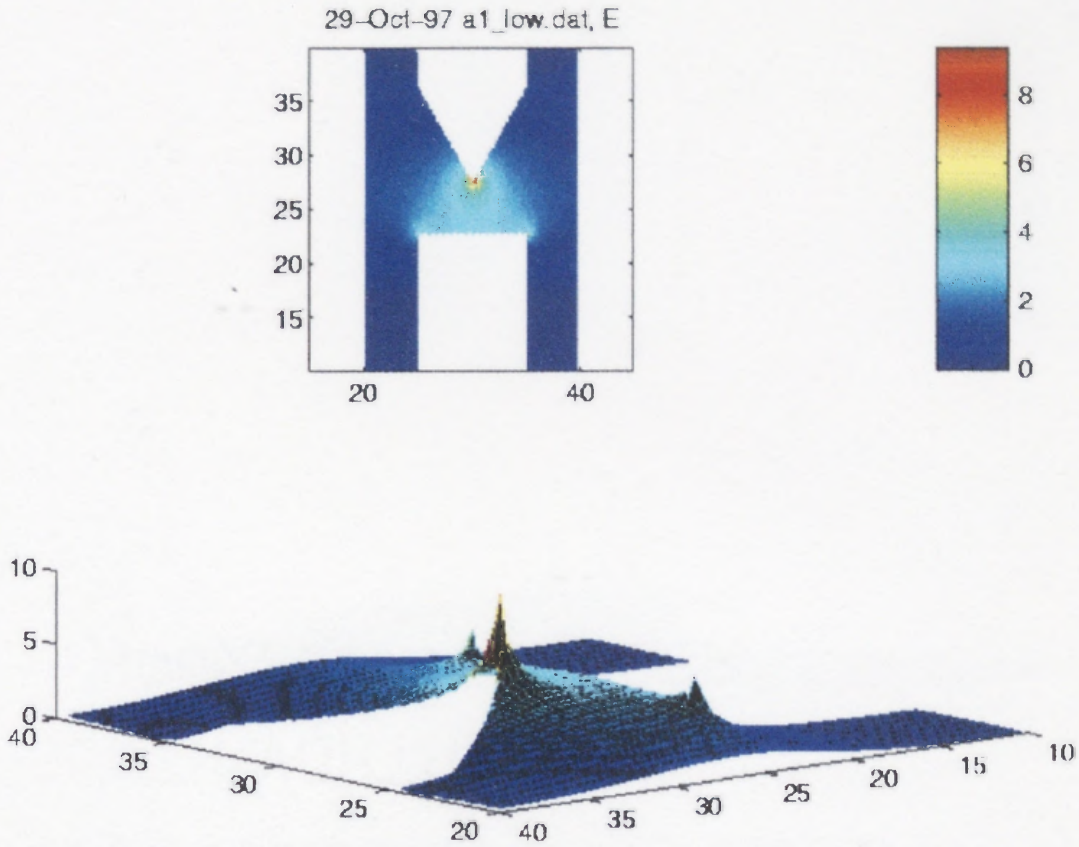

Fig.2.5 Two dimensional electric field mapping for structure A1. One singular field region is created near the tip of the triangle anode, and two smaller singular field regions close to the rectangular corners.

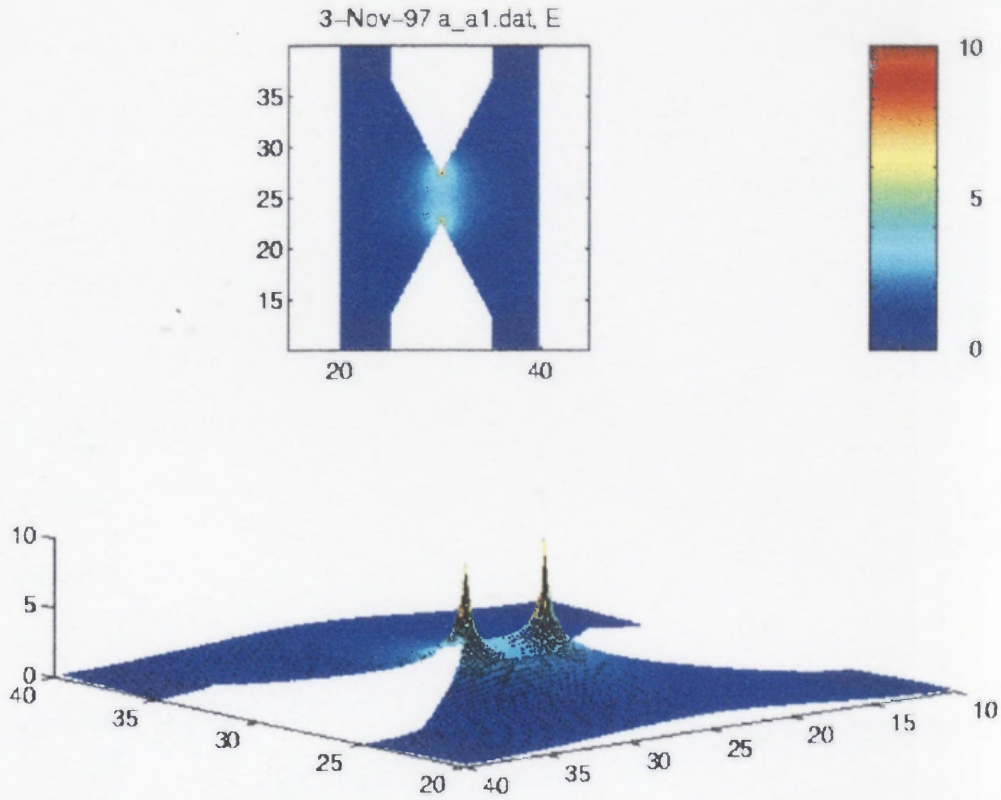

Fig.2.6 Two dimensional electric field mapping for structure A_A1. One singular field extreme is created near the triangular tip near the anode and as well as the cathode.

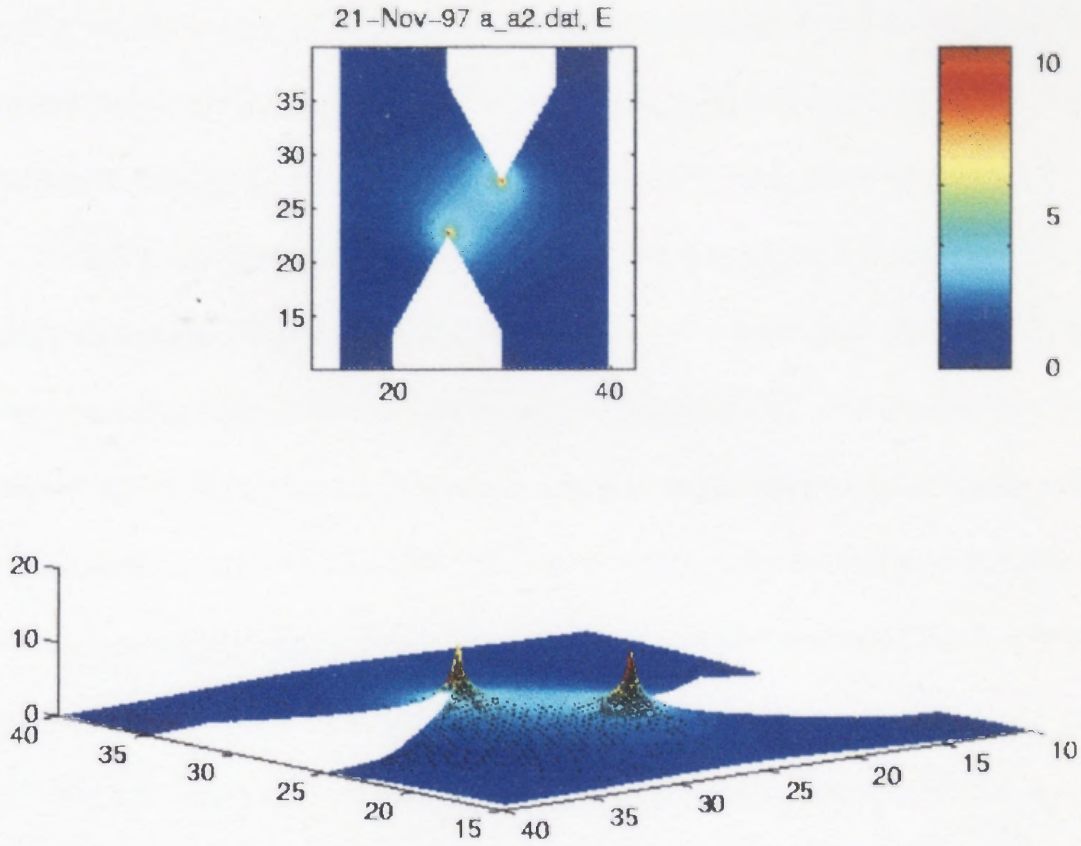

Fig.2.7 Two dimensional electric field mapping for structure A_A2. One singular field extreme is created near the triangular tip near the anode and as well as the cathode. The extreme field is slightly stronger and spreading in a larger area than that of A_A1 due to the lateral offset.

The software used for all the two dimensional simulation is Electric and Magnetic Field Design Package (Version 2.) developed by Field Precision Inc.. The core programs for conformal mesh generation and the finite difference solution of the Poisson equation were developed for Los Alamos National Laboratory. The images of the 2-D field mapping is post processed with Matlab, a high performance numeric computation and visualization software by the Math Works Inc.. Fig.2.4, Fig.2.5, Fig.2.6, and Fi2.7 are the electric field mapping for structure U1, A1, A_A1, and A_A2 respectively.

Fig.2.4 shows a two dimensional electric field mapping for structure U1. One singular field region is created near every corner of the rectangular electrodes. Fig.2.5 shows a two dimensional electric field mapping for structure A1. One singular field region is created near the tip of the triangle anode, and two smaller singular field regions close to the rectangular corners. The singular field near the triangle tip is much higher than that of the rectangular edge in structure U1. The testing of the device confirmed this enhancement that will be discussed in the later chapter.

Fig.2.6 shows a two dimensional electric field mapping for structure A_A1. One singular field extreme is created near the triangular tip near the anode and as well as the cathode. Fig.2.7 shows a two dimensional electric field mapping for structure A_A2. One singular field extreme is created near the triangular tip near the anode and as well as the cathode. The extreme field is slightly stronger and spread to a larger area than that of A_A1 due to the lateral offset. The testing of the device confirmed this enhancement that will be discussed in the later chapter. We actually found the A_A2 design give the most efficient terahertz radiation.

The simulation results are summarized as follows, in comparing the extreme field strengths, the conclusions are served as guidelines for the design of our final electrode testing patterns. Note that in this simple electrostatic simulation, the asymmetrical excitation effect is not included. Therefore the simulation can not distinguish the anode from the cathode. In real terahertz emitters the anode side is greatly enhanced, while the cathode side is greatly suppressed. Several explanation has been proposed for this asymmetrical excitation pattern, but it is still an active area of research. We will discuss our contributions to this research in later chapters. Besides the carrier's screening, the charge redistribution, the 3-D nature of the problem and other fast transient analysis are not included.

Summary of effect of various device parameters are listed as following: (1) Gap sizes may have little effect on field maximum, if the applied voltage is scaled by the gap size. (2) The sharper the triangle tip is, the higher maximum field is achieved close to it. (3) Shape of the antenna has great effect on field maximum. (4) Dipole length has no effect on field maximum. (5) The field maximum not only determined by the sharpness of the tip, the direction of the tip counts. (6) There is no advantage to use triangular tips on both sides because the presence of an additional high field region induce more voltage drop, which in turn makes each of them lower. However, this prediction is opposite to the results of experimental calibration. (7) When the sharp corner is round off, the shape of the field distribution plot stays the same. The field maximum is reduced a little bit because of the round corner. The 0.3 um radius of the corner is close to the reality if 1 or 2 um lithography is used. (8) Multiple high field peaks of equal or unequal values can be found

in these structures. But the problem is how to handle the focusing so that all of them can be useful.

As pointed out earlier, the over simplified simulation can not provide very accurate prediction on the device performance. But the modeling does correctly predicted the following: (1) The triangular tip design A1, A_A1, and A_A2 (as shown in Fig.2.5, Fig.2.6, and Fig.2.7) are far more efficient than the rectangular electrode design U1 (as shown in Fig.2.4); (2) The strongest maximum electric field comes from the structures with the sharpest electrode; (3) The offset electrodes provide further enhancement. The marginal difference between structure A_A1 (shown in Fig.2.6) and A_A2 (shown in Fig.2.7) was first suspected by us at the design stage, but late the A_A2 structures with offset sharp electrodes was found experimentally to be the best antenna design ever.

On the other hand, the simulation results falsely predicted one aspect. The simulation predicted structure A1 (shown in Fig.2.5) is better than A_A1 (shown in Fig.2.6), which is opposite to the experiment demonstration. The A_A1 structure with both sharp anode and cathode is a more efficient design. The argument, which suggested by the simulator, that creating two extreme field region on each side of the gap (A_A1) will reduce the strength of each one of them comparing to the structure with just one extreme field spot (A1). This discrepancy, we believe, is due to the failure to include the carrier redistribution effect that in favor of the anode. The suppression on the cathode side singular field, somehow further enhanced the singular field on the anode side. In principle, the reason why the simulation is very limited is because of the presence of the semiconductor and air interface.

2.2.2 Overcome the Gap Size Saturation Effect on Terahertz Radiation

Another effect which has not been taking into account in the simulation is the radiation power saturation for a particular gap size. As observed by Brener *et al.* [5 in chapter 4], radiation power reaches a saturated value. Further increase of the bias or the optical excitation power will not increase the terahertz radiation. Without prior understanding to predict the optimal gap size, we had to design the antenna with various gap sizes (5, 10, 20, 30, 45 μm and etc.). The optimal size is found experimentally.

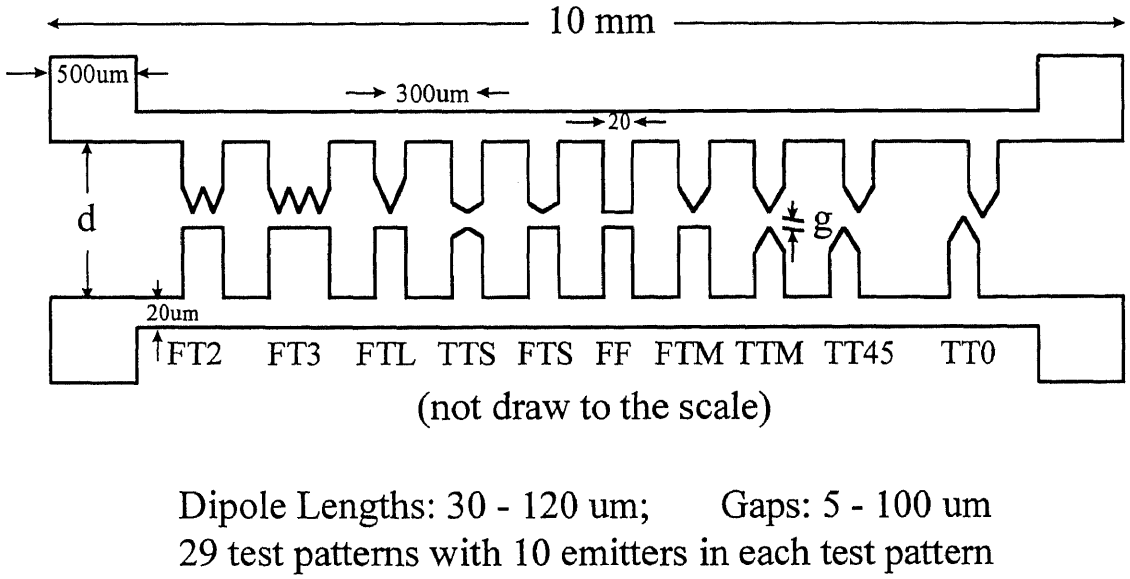

Fig.2.8 A schematic diagram of the test patterns for the new terahertz emitter and detector designs.

2.2.3 Dipole Length Optimization

Still another effect that has not been taken into account is the dipole antenna response. It is controlled by adjusting the dipole length. As a ultra short pulse with subpicosecond duration, the frequency band width is as broad as 1THz (1000 GHz) or more. Both the center frequency and bandwidth may vary for different semiconductor parameters.

Consequently, the proper antenna response is important for coupling the most terahertz power from the semiconductor substrate into the air. To achieve this, antennas with various dipole length (30, 45, 60, 75, 90, and 105 μm) are made. The ultimate efficiency is determined through experiments.

2.2.4 The Final Testing Patterns

Taking into account all the factors discussed in this chapter the final testing patterns made are illustrated in Fig.2.8. The d is the separation between the transmission lines. When the gap is small d is equal to the dipole length. The g is the minimal separation between the anode and cathode. The gap can be in the perpendicular to the triplines (as in most structures in Fig.2.8), parallel to the triplines (as in Fig.2.8 structure TT0), or tilted (as in Fig.2.8 structure TT45). We vary the d and g. Table 2.2 shows all the dimensions of the test pattern we made. And for one particular d and g, ten different designs are made available on the same test pattern for the ease of accurate performance comparison. Each device is made 300 μm apart to avoid any interaction. Since the device is activated by laser excitation, only the antenna under illumination is active. But putting too many device between one pair of transmission lines may have the risk of introduce higher leakage current. As to our knowledge, we are the first doing so, and find no effect on the device performance. That is because the very high resistance of our LTG substrate, the dark current is very low even with 10 devices in parallel.

Table.2.2 Test Pattern Dimensions

Dipole Length (μm)	Gap size (μm)	Dipole Length (μm)	Gap size (μm)
30	5	90	30
45	5	105	5
45	10	105	10
45	20	105	20
60	5	105	30
60	10	120	5
60	20	120	10
60	30	120	20
75	5	120	30
75	10	Single electrode	
75	20	105	50
75	30	105	75
90	5	120	50
90	10	120	75
90	20	120	100

2.3 New Approaches to High Resolution Terahertz Imaging using Near Field Terahertz Probe

With new developments on real-time T-ray imaging, Time-domain Terahertz Spectroscopy (THz-TDS) has extended his applications from a valuable and sensitive tool for materials studies to a variety of analytical imaging applications such as: chemical mapping and a host of commercial applications (safe package inspection, industrial process control, food inspection, as well as biological and medical imaging). But due to the long wavelength of the THz radiation, the spatial resolution is essentially limited by diffraction to several hundred micrometers, and is frequency dependent over the large

bandwidth of the THz pulses. We have recently shown a near field imaging approach to create high-resolution "T-ray" images. In the previous work, the near field probe is made with a small conical aluminum tip with a Cr/Ni alloy. Removal of the aluminum cone and polishing of the Cr/Ni tip result in the small, circular aperture. The probe is then place at the focal point of the THz beam. A resolution of 140 μm has been observed with the tip probe. [53] In this work we describe three kinds of new designs of near field probes. The first new design integrates the aperture for near field imaging on the THz photoconductive antenna. We name this configuration as Integrated Backside Aperture (**IBSA** as shown in Fig2.9a), an analogy to the optical near-field probes. The second design uses a 100μm thin wafer to reduce the distance between the short antenna and sample for near-field operation. It is called Thin Wafer No Aperture (**TWNA** as shown in Fig.2.9b). The last design is using SOS substrate to enable backside optical excitation (**BSOE** as shown in Fig.2.9c) to reduce the distance between the antenna and the sample. The IBSA and TWNA designs are analogies to microwave near-field probes. All designs eliminate the needs for refocusing the THz beam to incorporate the near field tip. The sample can be conveniently scanned on the back of the integrated THz near field emitter for high resolution images. Therefore the setup is simpler and easier to align than using near field tips.

The IBSA integrated near field probes (as shown in Fig.2.9a) are fabricated on annealed low temperature GaAs (LTG). The metal patterns are deposited on both the front and the back side of the wafer by conventional lithography. The front side metal patterns define the photoconducting antenna for terahertz generation. On the back side the metal patterns construct an aperture (25μm×25μm square) for near field imaging. A

regular GaAs wafer is as thick as 500μm. To insure near field operation at all THz frequencies, the wafer is ground to 100 μm thin.

It is a well known principle of microwave engineering that the most efficient way to couple far-field radiation to a device of dimension much smaller than the photon wavelength is to attach the device across the terminals of an antenna. [54,55] It is easy to apply this rule to near-field terahertz probes, considering the terahertz generation principle in photoconductive switches. The terahertz wave is originated in the semiconductor from the current surge induced by the femtosecond optical excitation, and then coupled into the dipole antenna. We make near field emitters simply by using a dipole antenna with a dipole length shorter than 100μm. In the TWNA structure (as shown in Fig.2.9b), the wafer is grind to 100 μm thick. Or alternatively in the BSOE structure (as shown in Fig.2.9c), we use a short dipole antenna (60μm long dipole with a 10μm gap in the middle) fabricated on silicon on sapphire (SOS). Because the sapphire substrate is transparent to the 800 nm excitation pulses from Ti:sapphire mode locked laser, we can excite the antenna through the back side. In that way, the dipole antenna can be placed very close to the sample without the wafer in between. Although these approaches do not provide the ultimate imaging resolution as the near-field probe with apertures, they require less sophisticated device processing and are more towards a unity efficiency.

In the later chapters, we will present the performance of these three types of integrated near-field probes for sub-wavelength spatial resolution terahertz imaging. We demonstrated a 30μm THz image resolution using a device on thin wafer with integrated backside aperture. Simpler designs also yield a spatial resolution of ~100μm. These

resolutions are much below the diffraction limit of the terahertz wave. To our knowledge, they are the best spatial resolution for T-ray imaging.

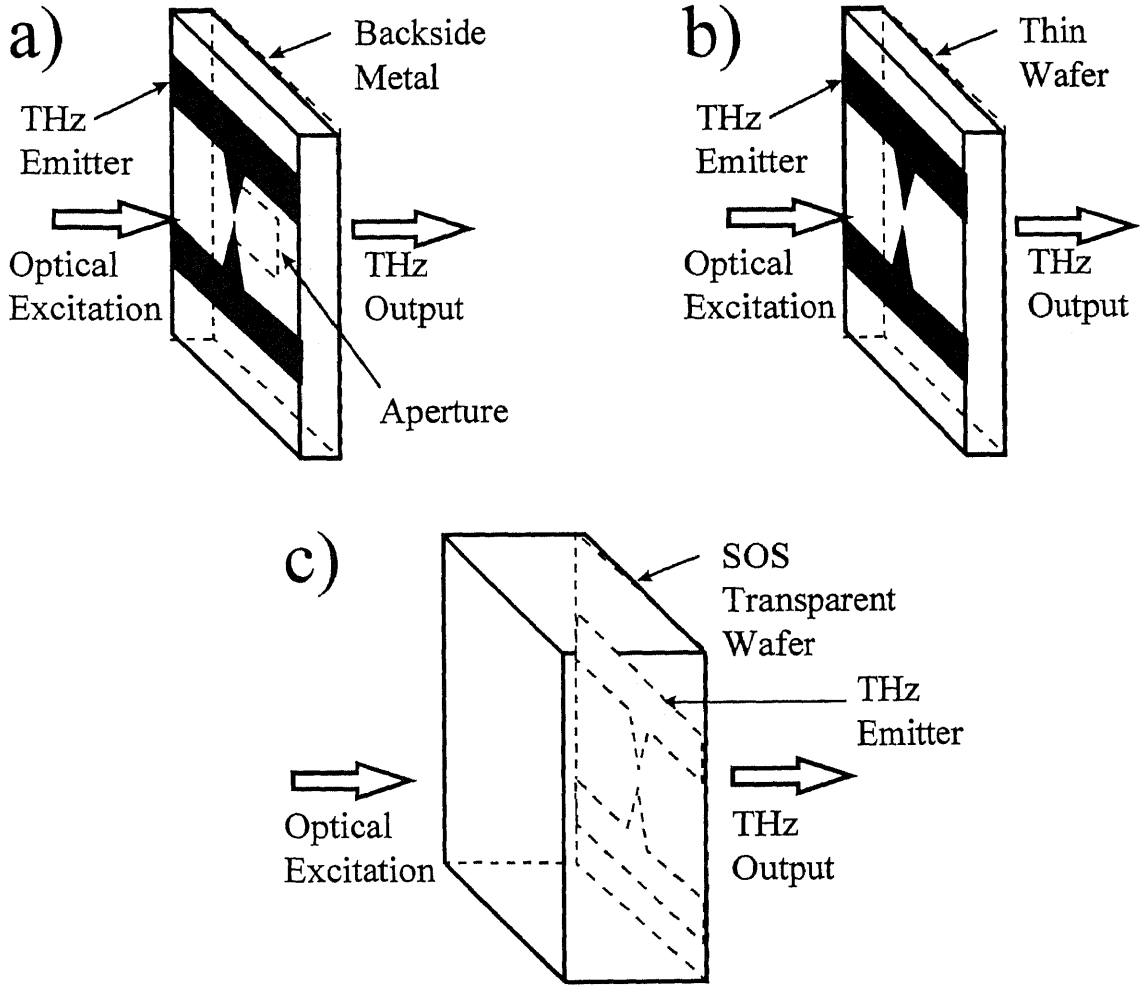

Fig.2.9 Three new designes of near-field terahertz probes: a) Integrated Backside Aperture (**IBSA**) integrates the aperture for near field imaging on the THz photoconductive antenna; b) Thin Wafer No Aperture (**TWNA**) using a 100μm thin wafer to reduce the distance between the short antenna and sample for near-field operation. c) using SOS substrate to enable Backside Optical Excitation (**BSOE**) to reduce the distance between the antenna and the sample.

CHAPTER 3

FABRICATION OF SINGULAR ELECTRIC FIELD TERAHERTZ ANTENNAS

3.1 Semiconductor Material Preparation

3.1.1 Low Temperature GaAs Growth and Post Annealing

It has been discovered that optical excitation near the anode produces a stronger electrical current surge and therefore stronger THz radiation. [31,32,33,34] A material of very short lifetime, high resistivity, and high mobility is desired. The first THz antenna was made with irradiation damaged silicon on sapphire (SOS) with a subpicosecond short lifetime, and the surrounding Si need to be etched away for lower leakage current. The low temperature grown GaAs (LT GaAs) on semi-insulating substrate is used for our THz antennas.

The high resisitivity requirement is for the ability to bias the device with higher voltage, since high electric field is desired for efficient terahertz radiation. Semi-insulating substrate is used to reduce any substrate conduction. Because of the excessive defects, the low temperature grown GaAs thin film also has a very high resistivity.

As discussed in chapter 1, short life time is a very important factor for efficient terahertz radiation, and the determinant factor for terahertz detectors. A high mobility is also desired for a short acceleration time of the photo generated carriers. We chose low temperature GaAs, owing to this superior carrier mobility in GaAs. The short carrier lifetimes have been shown to result from excess As in the form of As antisite and Ga vacancy point defects [56,57]. Annealing leads to the formation of As-precipitates [58], yielding high resistivity and high carrier mobility material.

The GaAs samples are grown on the semi-insulating GaAs substrate at 250°C, 300°C, and 350°C, in about 90 minutes. The thin film is 1.45 μm thick.

Rapid thermal annealing is conducted when the sample faces down towards the lamp on a semi-insulating GaAs wafer, and another GaAs wafer is placed on top of the sample for the best results. Annealing times of 1 ~ 10 minutes are tried for samples grown under 250°C, 300°C and 350°C. According to the our experience, the samples are annealed under 600°C, and flushed with forming gas (N_2 and H_2).

Carrier lifetime and photo-conductivity measurements are conducted, as described later in this section. The optimal material preparation conditions are found to be 300°C MBE growth and 1 minute post rapid thermal annealing at 600°C, for the fastest photo-response with a high breakdown field.

3.1.2 Carrier Life Time and Photo-Conductivity Measurement

In order to make a state of the art THz antenna, the material is carefully characterized. LT GaAs samples grown at different temperatures (250°C - 350°C) and rapid thermal annealed (RTP) for different time (1 minute - 10 minute) are studied.

Time-resolved reflectivity measurements are used for the ultra short lifetime measurement to insure that the THz antenna is made on the material with sub-pico-second responds. The physical mechanism behind this technique is depicted in Fig.3.1. An optical pumping pulse generates the carriers in the semiconductor, the presence of the carriers changes the reflection of the probe beam. Since this effect is directly related to the carrier density, it exhibits a exponential decay at a time constant equal to the carriers' lifetime. By varying the timing of the incoming probe beam, we sample the reflection changes before

and after the pump point by point. The speed of this decay reflects the carrier lifetime. The probe beam is limited to a much lower power level, so that itself will not generate too much carriers in addition to those generated by the pump beam. The experiment setup is illustrated in Fig.3.2. The time resolved reflectivity measurement of lifetime has a resolution limited by the laser pulse width. In our case, a 100fs mode-locked Ti:Sapphire laser is used, which provides a 0.1ps time resolution.

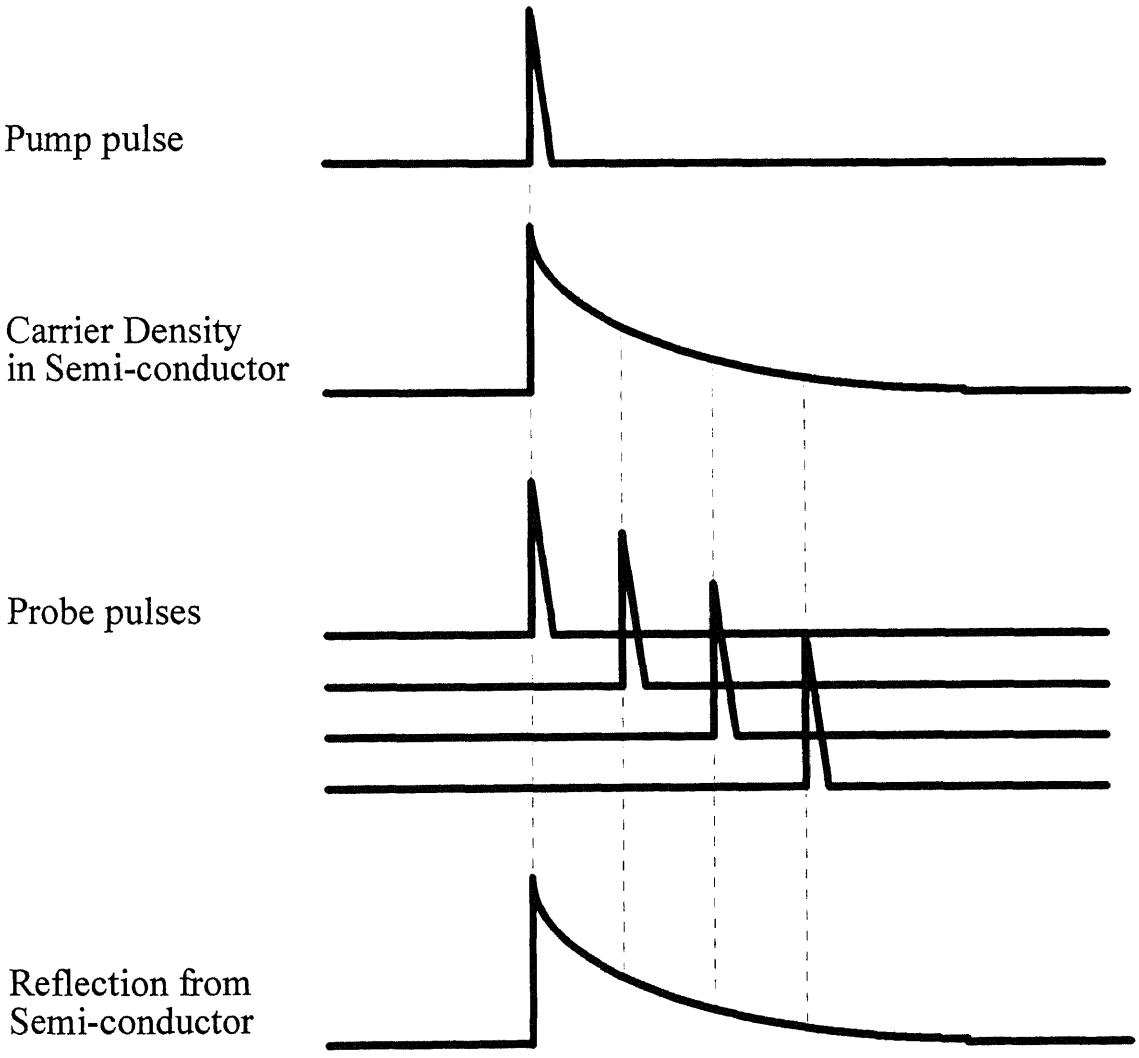

Fig.3.1 Theory of time-resolved reflectivity measurement

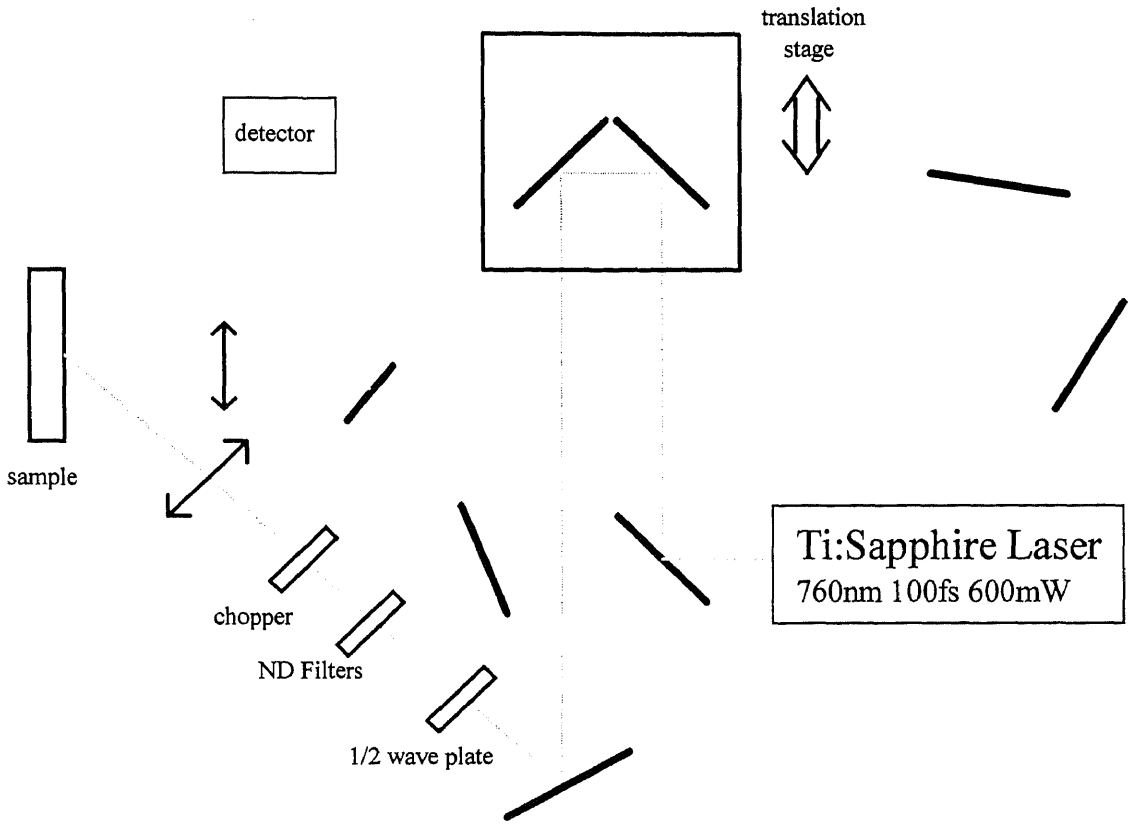

Fig.3.2 Time-resolved reflectivity measurement setup

Fig.3.3, Fig.3.4, and Fig.3.5 show several time resolved reflectivity transients of our samples. Fig.3.3 shows how the response changes with annealing time. The long tail means the photoconductive switch takes longer to shut off. In Fig.3.4, the switch exhibits a overshooting behavior that also shuts off slowly. The optimal material growth preparation condition is found to be 300°C and 1 minute rapid thermal annealing at 600°C, for the fastest photo-response (0.25ps, as depicted in Fig3.5), also with a high breakdown field.

Photo-conductivity and dark current measurement are done to insure the THz antenna is of low noise and high damage threshold.

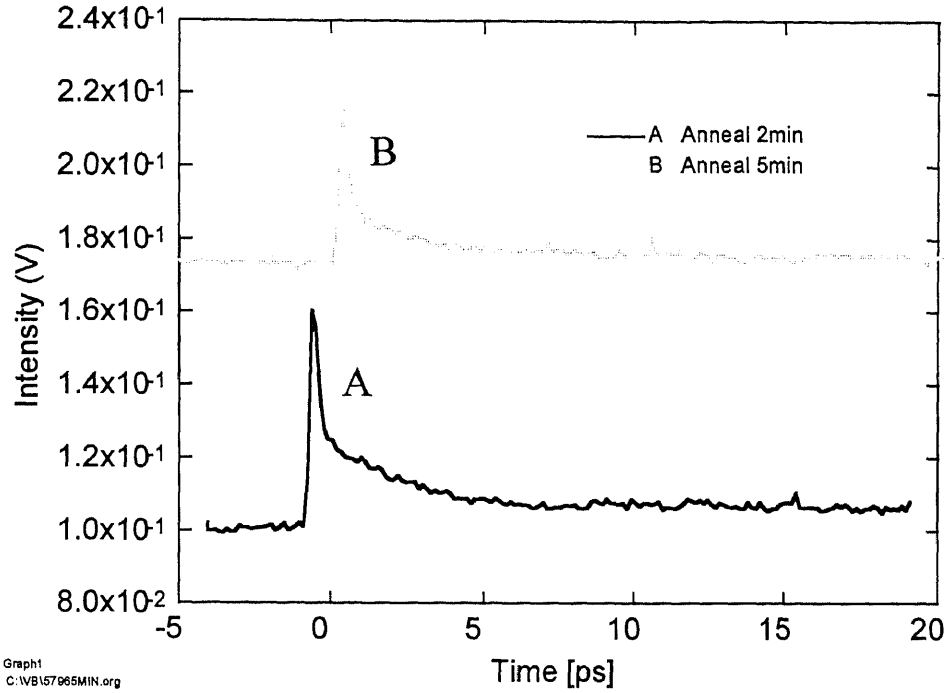

Fig.3.3 Time resolved reflectivity transients of low temperature grown GaAs depends on annealing time (2-minute and 5-minute). The long tail makes it longer for the photoconductive switch to shut off.

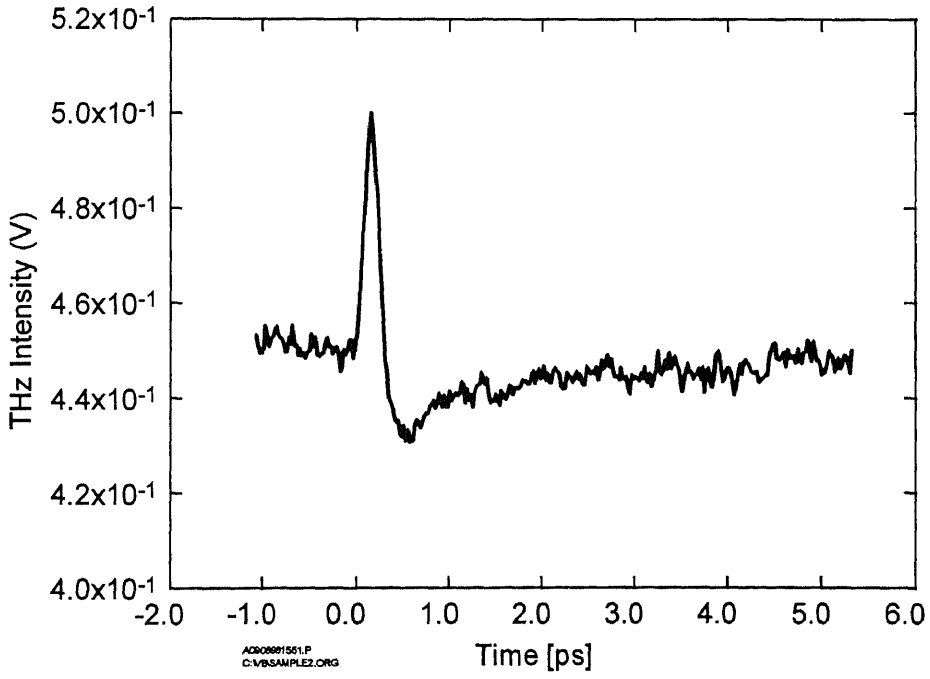

Fig.3.4 Time resolved reflectivity transients of low temperature grown GaAs exhibits a overshooting behavior that also makes a switch shuts off slowly.

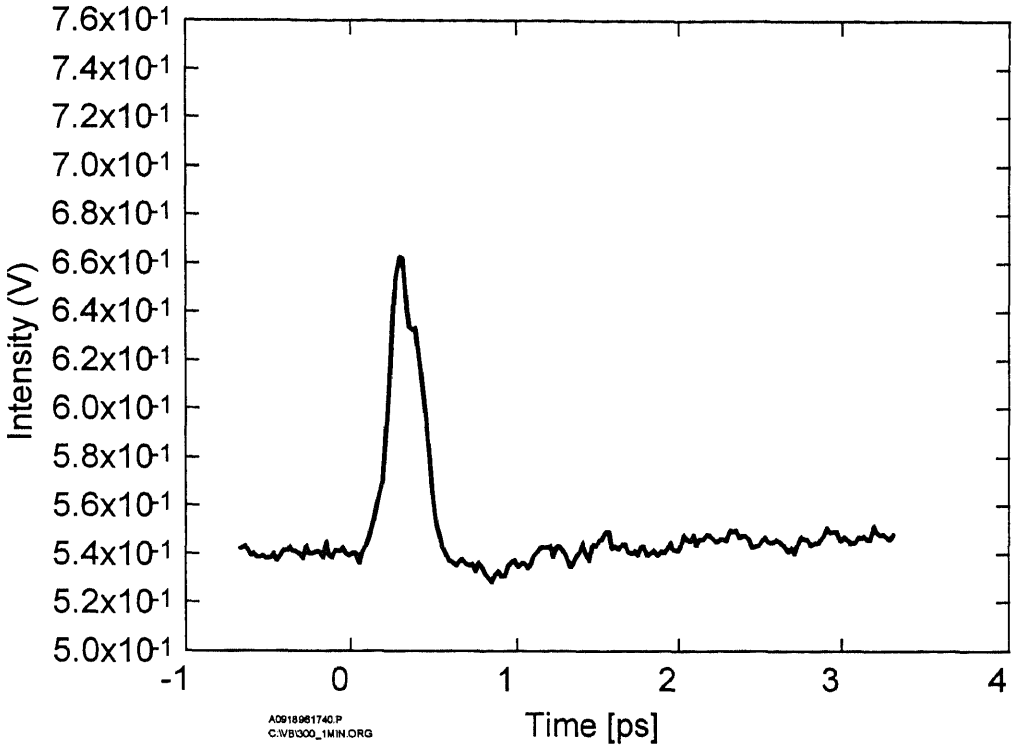

Fig.3.5 Time resolved reflectivity transients of low temperature grown GaAs with subpicosecond response. The optimal the material growth preparation condition is found to be 300°C and 1 minute rapid thermal annealing at 600°C, for the fastest photo-response (0.25ps).

3.2 Device Fabrication

3.2.1 Metal Deposition

The metal patterns are deposited using one of the usual schemes for ohmic contacts on n-type GaAs (800Å Au-Ge, 200Å Ni, 200Å Ti, 2000Å Au). Fig.3.6b inset shows a schematic diagram of the metal electrodes deposited on the structures. As described in chapter 2, we vary the dipole length and, gap size and electrode design.

We also fabricated three kinds of new designs of near field probes. The first new design integrates the aperture for near field imaging on the THz photoconductive antenna. We name this configuration as Integrated Backside Aperture (**IBSA** as shown in Fig3.7a),

an analogy to the optical near-field probes. The second design uses a 100μm thin wafer to reduce the distance between the short antenna and sample for near-field operation. It is called Thin Wafer No Aperture (**TWNA** as shown in Fig.3.7b). The last design is using SOS substrate to enable backside optical excitation (**BSOE** as shown in Fig.3.7c) to reduce the distance between the antenna and the sample.

3.2.2 Packaging and Wiring

The antenna is packaged on a IC chip carrier that has been cut in half, so that the antenna structure can stick out of the chip carrier as illustrated in Fig.3.8a. Some antennas are mounted in larger chip carriers which have a hole opening (Fig.3.8c) to allow the THz wave to pass through and to mount a Si lens.

An shown in Fig.3.8b, a 1mm radius Si lens can be mounted on the back of the antenna, to improve the THz coupled out to the free space. This technique can increase the detected current by a factor of 3-5. Alignment marks are made on the mask designed for metalization. These marks are used to align the Si lens with the antenna of our choice, when we mount the lens under a stereo microscope.

Structures made for near field spectroscopy use the package type shown in Fig.3.8a, without the Si lens, to minimize the distance between the antenna and the sample. But this mounting condition makes the near field chip (which is only 100μm thin) very fragile. A conceptually better package for future production will be using backside bonding to a thick silicon on sapphire (SOS) chip to provide support to the thin near field chip. Since the SOS is transparent to the laser excitation beam, it will not block the optical beam, as illustrated in Fig.3.9.

a) side view

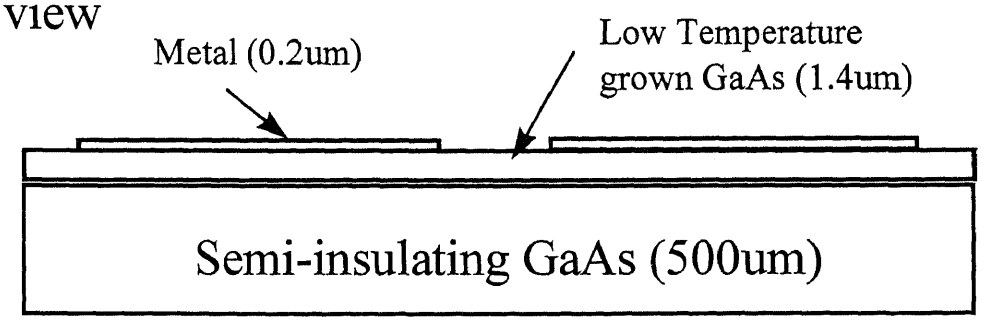

b) top view

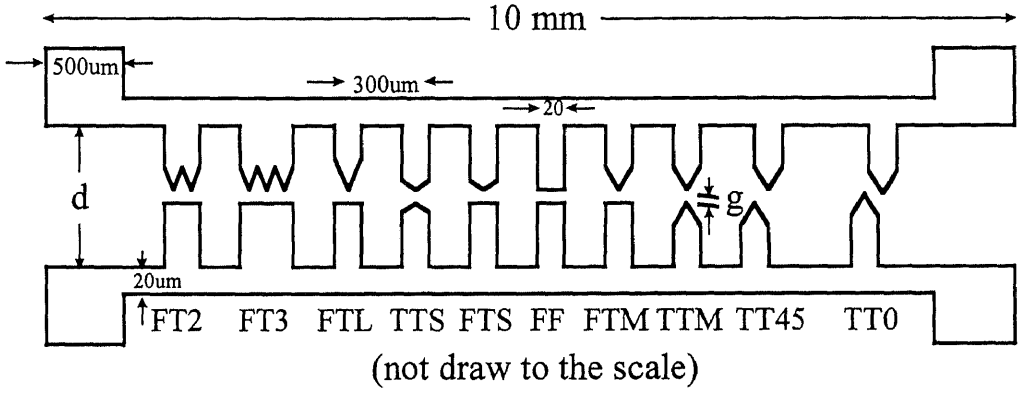

(not draw to the scale)

Dipole Lengths: 30 - 120 um; Gaps: 5 - 100 um
29 test patterns with 10 emitters in each test pattern

c) a microscopic picture of actual device TT0

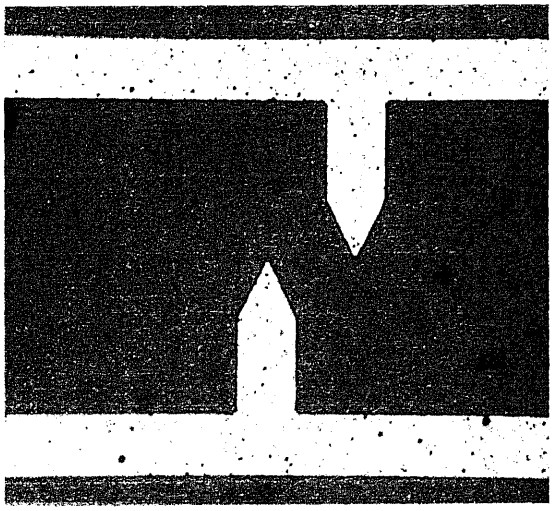

Fig.3.6 A schematic diagram of the test patterns for the new terahertz emitter and detector designs.

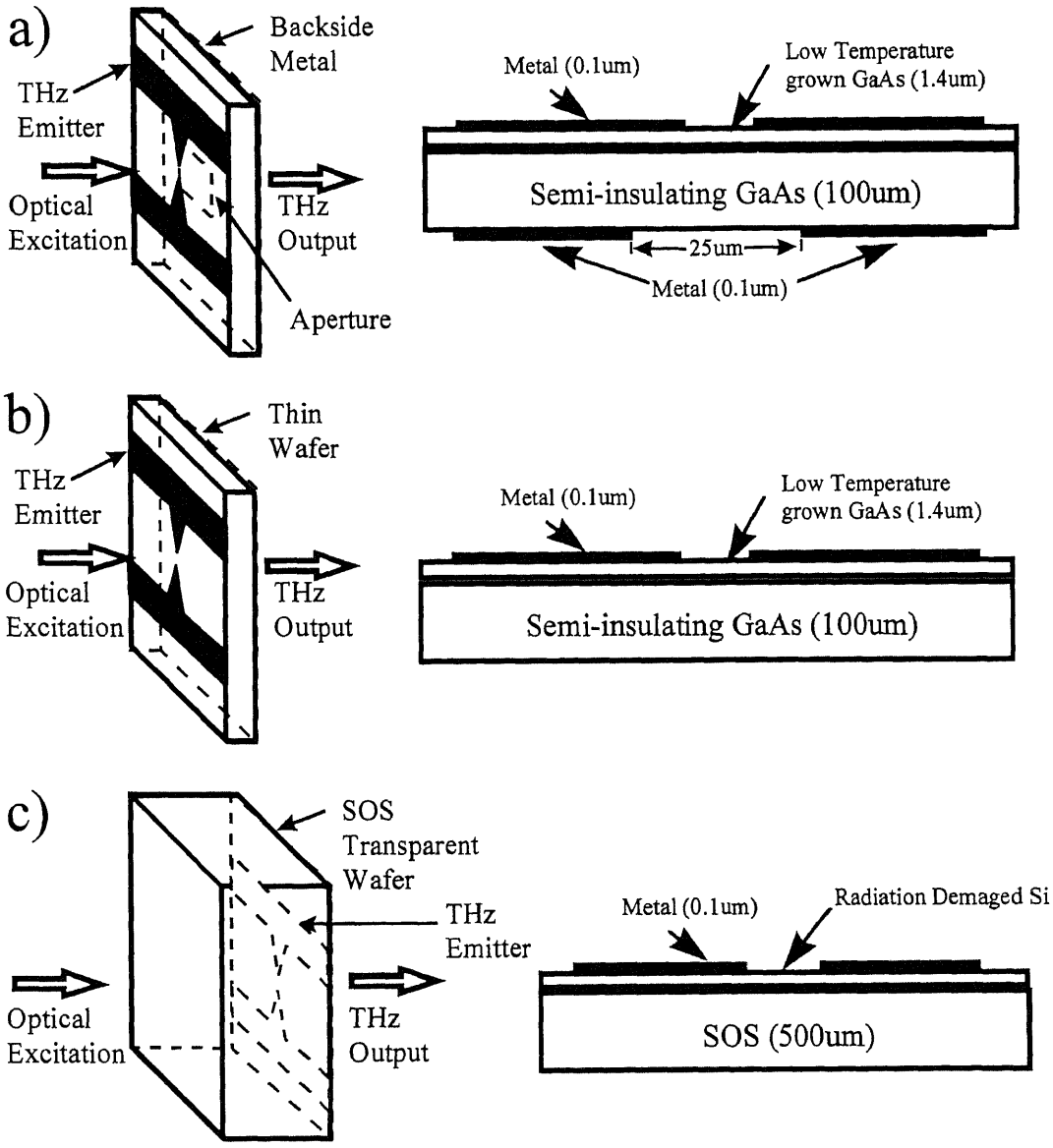

Fig.3.7 Three new designs of near-field terahertz probes: a) Integrated Backside Aperture (**IBSA**) integrates the aperture for near field imaging on the THz photoconductive antenna; b) Thin Wafer No Aperture (**TWNA**) using a 100μm thin wafer to reduce the distance between the short antenna and sample for near-field operation. c) using SOS substrate to enable Backside Optical Excitation (**BSOE**) to reduce the distance between the antenna and the sample.

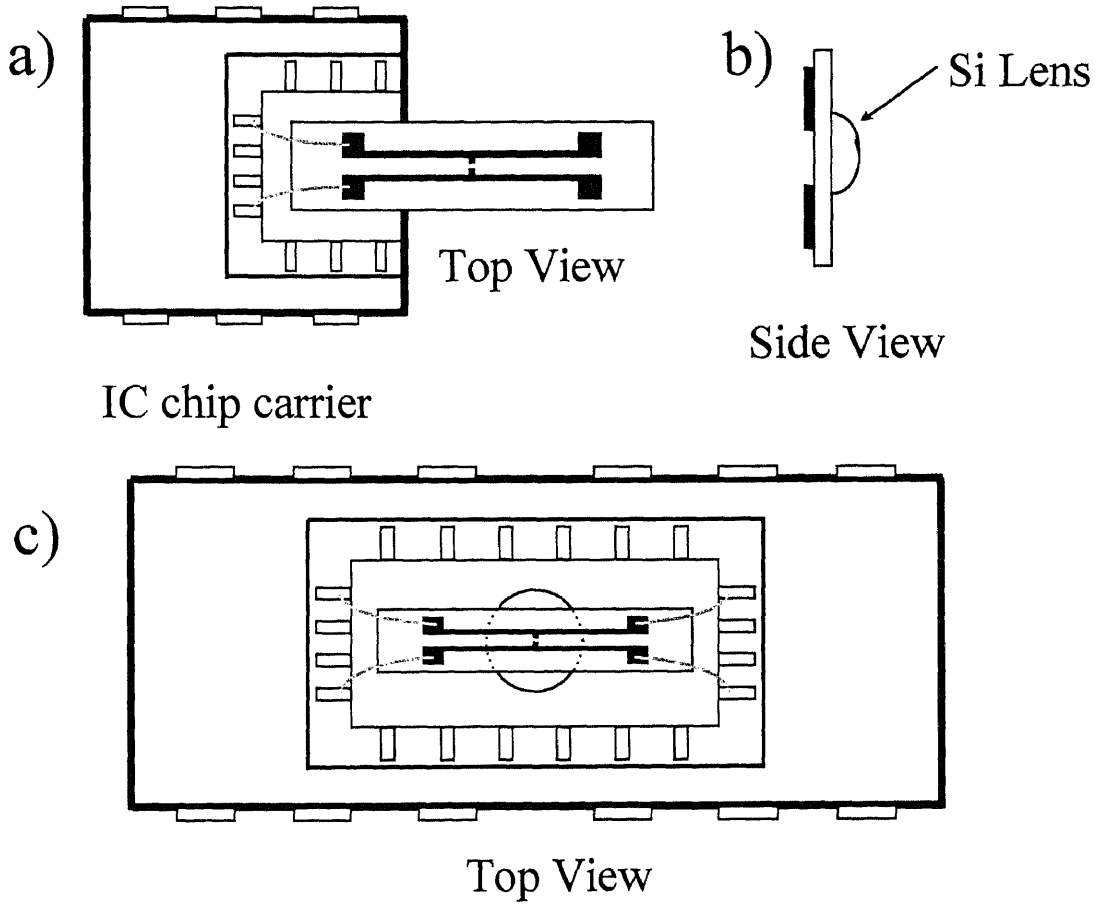

Fig.3.8 Package diagram. a) Top view of a package in a half IC chip carriers, the antenna protrudes out of the chip carrier; b) Side view of a antenna with a Si lens attached on the back; c) Top view of a package in a whole IC chip carriers, the antenna in placed in the center of the hole on the chip carrier.

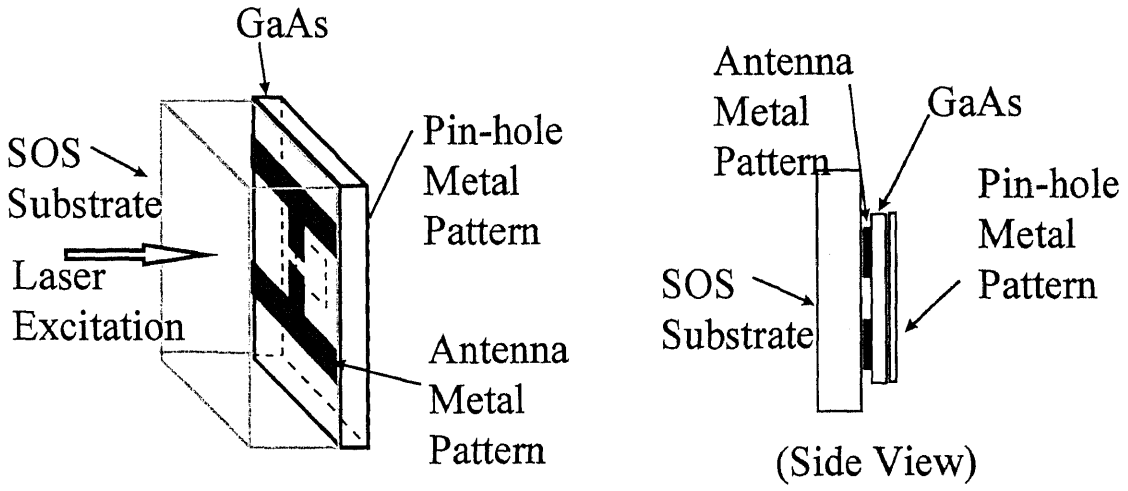

Fig.3.9 Better support for near field substrate using backside bonding.

3.2.3 Silicon Hyperhemispherical Lens

Substrate lenses are used on our integrated terahertz emitters and detectors to couple the radiation in and out of the chips more directionally and efficiently.[19,20] Due to the broadband nature of the terahertz radiation, we use aplanatic lens for this application.

An optical system free of both spherical aberration and coma is said to be aplanatic. An aplanatic lens can also be found for any particular pair of conjugate points, although in general it will need to be an aspherical lens. Except for a few special cases, no lens combination with spherical surfaces is completely free of both these aberrations. One special case important in microscopy is that of a single spherical refracting surface. It is very important, because of the small size (1mm radius) and the non typical material (Si) for the lens makes it very hard to fabricate any aspherical lens.

Fig.3.11 shows the simplified (when the substrate is made of the same material of the lens) operation of the substrate lens: a is the real image plane, while b is the apparent imaging plane, all measured from the center of the lens, with

$a = r / n;$ $b = r \bullet n$

The lens is used together with a paraboloid mirror to collect and collimate terahertz radiation out of the emitter, and focus the terahertz beam on to the detector. As shown in Fig.3.10 the apparent image points of the substrate lens is overlap with the focal points of the paraboloids. Note that the schematic diagram is not drawn to scale, the si lens is only as small as 1mm in radius, while the paraboloid is as large as almost 5cm.

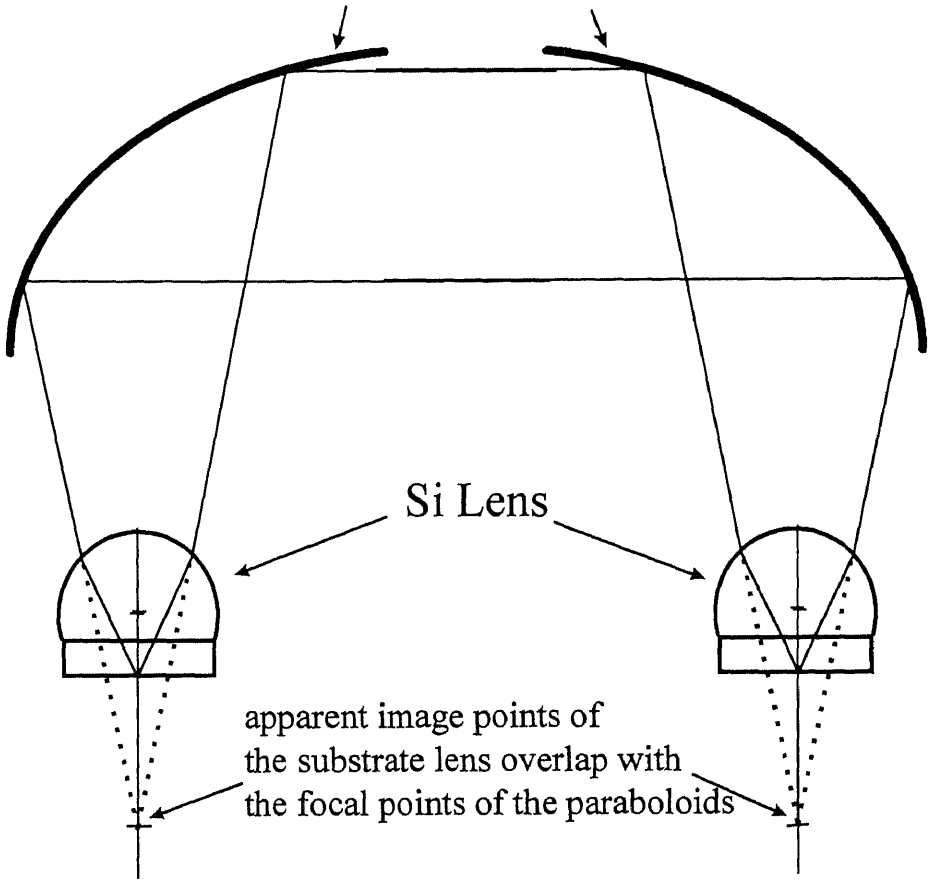

Fig.3.10 The lens is used together with a paraboloid mirror to collect and collimate terahertz radiation out of the emitter, and focus the terahertz beam on to the detector.

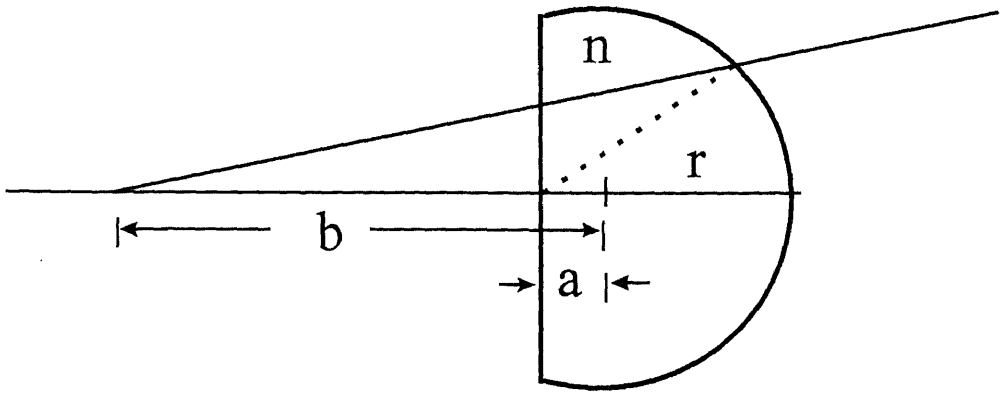

Fig.3.11 A simplified schematic diagram of the operation of the substrate lens, when the substrate is made of the same material of the lens.

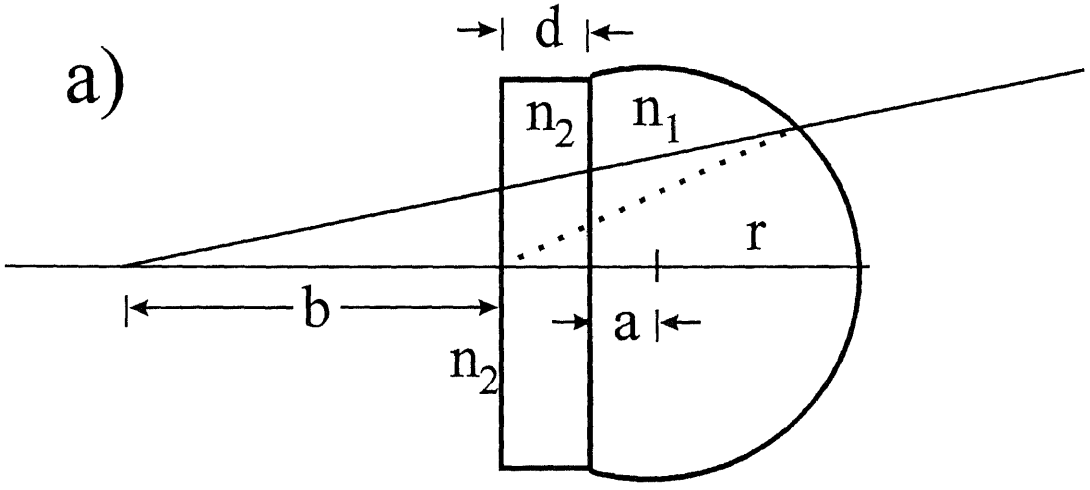

b) Si hyperhemispherical lens for 0.5 mm GaAs wafer

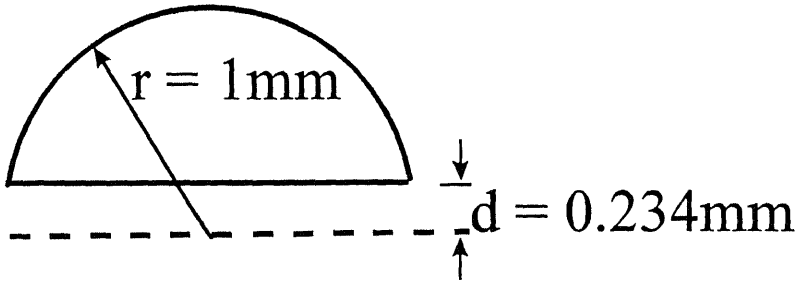

Fig.3.12 a) Si hyperhemispherical lens design for GaAs wafer (account for the difference in refractive indexes) b) The final dimensions of the lens.

Since the substrate is GaAs while the lens is Si, we have to account for the difference in refractive indexes Fig.3.12a:

$$r + a = r + r / n_1 + (n_1 - n_2) * d / n_2 - d$$

The design of the lens is shown in Fig.3.12b. The lens is fabricated by Hibshman Corp. with crystalline Si balls of very high resistivity (>10 KΩ cm) to minimize the transmission loss. After the cut, the backside is optically polished.

CHAPTER 4

CHARACTERIZATION OF THE TERAHERTZ ANTENNAS

In this chapter, we present the characterization of the new designs of more efficient terahertz (THz) radiation emitters and detectors enhanced by electric field singularities (EFS) using sharp and laterally offset electrodes. We compare the performance of the terahertz emission and different polarization properties resulting from these structures. An average THz radiation power of 3μW is achieved under 20mW excitation, calibrated by free space electro-optic sampling. This is the most efficient emitter to our knowledge for excitation power in the mW range. [29] Previous reported THz radiation powers of photoconductive switches are 38nW [39] and 10nW. [25] We also study the gap size dependence of the THz radiation, and find an absence of a positive electrode effect in the small gap limit.

4.1 Characterization System Setup with Dual Detection Schemes

In this work we describe powerful THz emitters and detectors by using new electrode geometries in the limit of small gaps that optimize the singular electric fields experienced by the photogenerated carriers. We compare the relative THz radiation power of various new dipole designs, and calibrate the absolute average power of the THz beam using free space electro-optic sampling .

The new THz emitters consist of two coplanar striplines with sharp indentations facing each other, as depicted in the inset of Fig.4.3. As described in chapter 2, we vary the separation between the parallel striplines *d* and the gap distance g. If *g* is small, then *d*

is approximately equal to the dipole length. The sharpness of the electrodes determines the peak value of the singular electric field. Moreover, the fringing fields are enhanced when laterally offset electrodes are used (i.e. structure TT0 in Fig. 1 inset). The offset angle provides additional control in maximizing the overlap of high electric field regions with the laser excitation spot. [29,30]

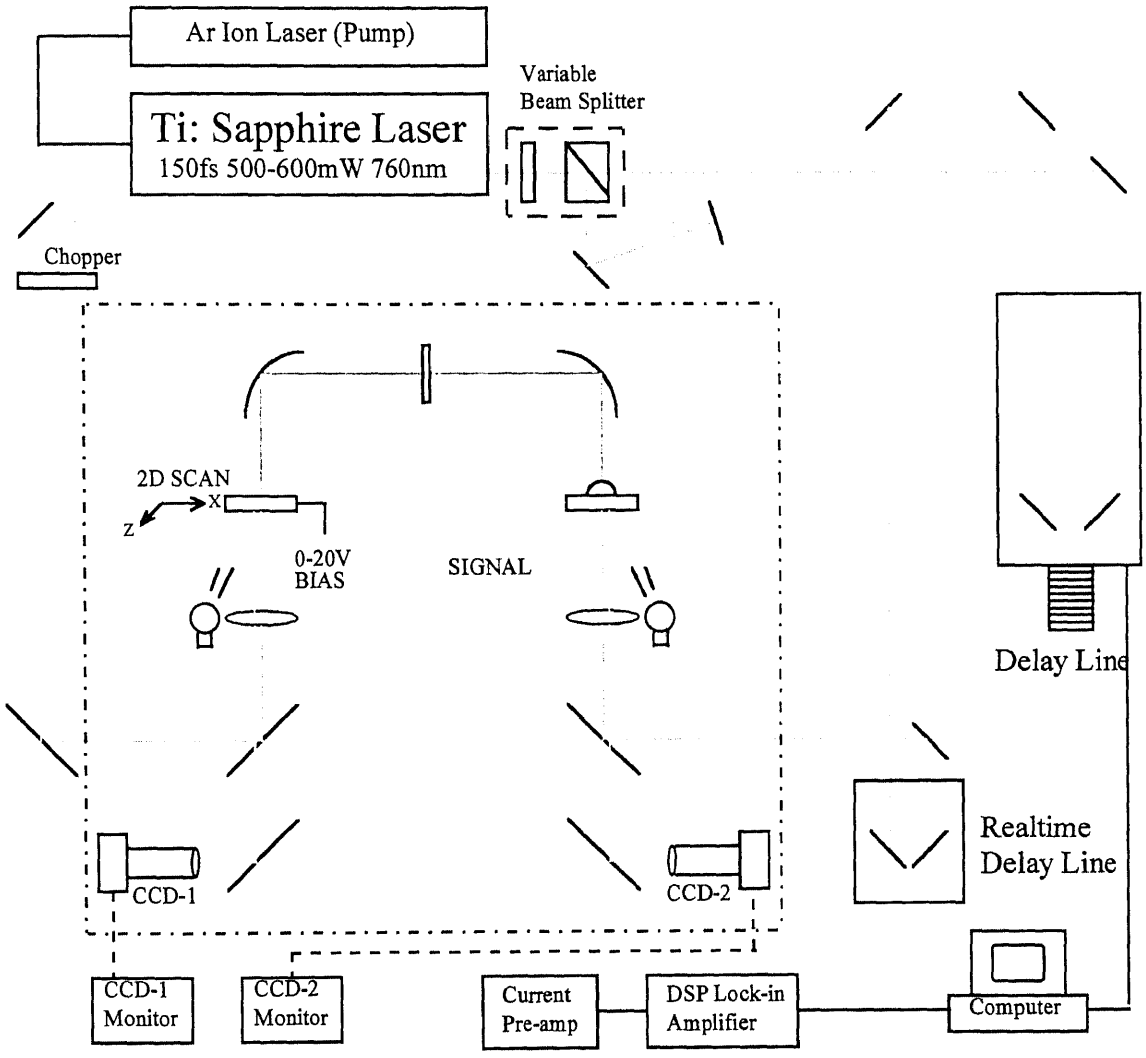

Fig.4.1 Experimental setup for the characterization of terahertz generation and detection using photoconductive antennas with scanning capabilities on the emitter side.

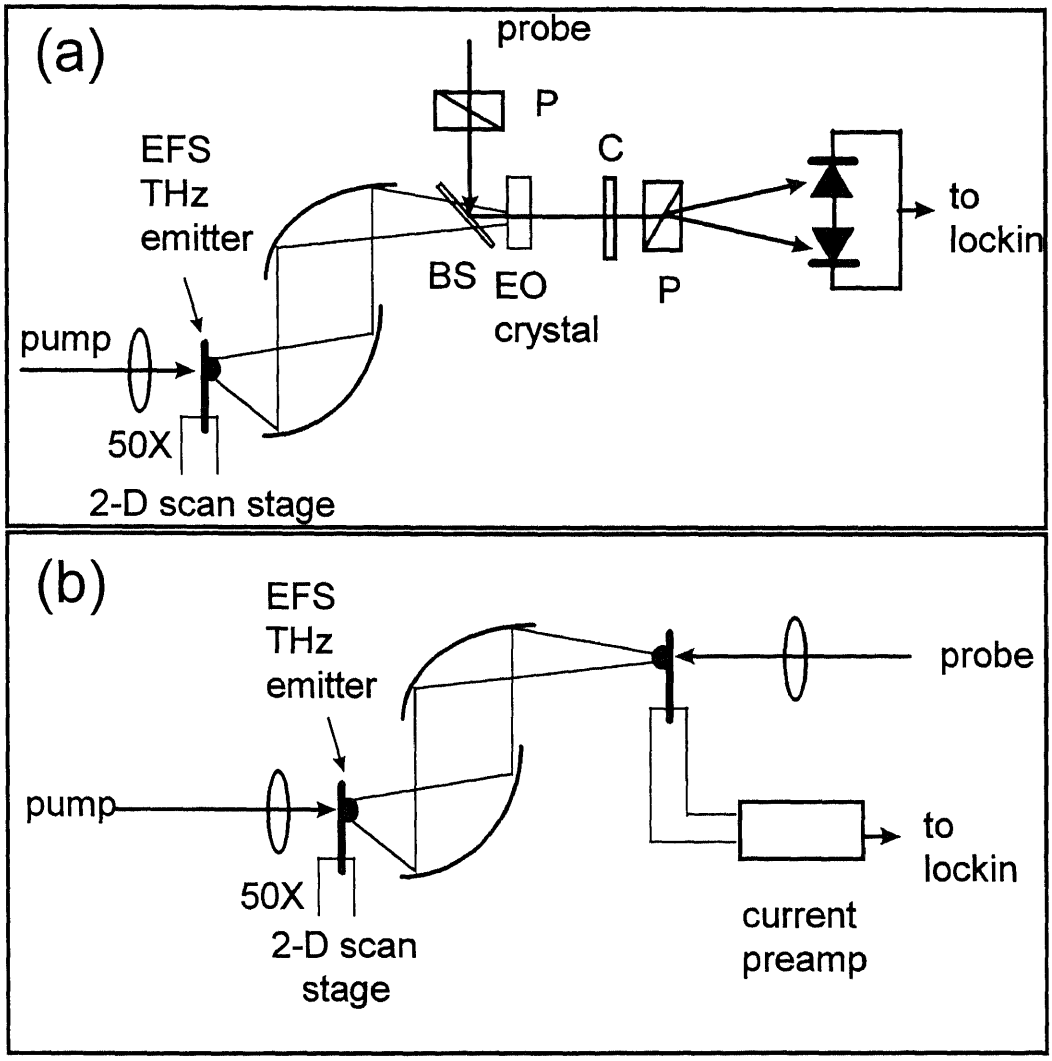

Fig.4.2 Experimental setup: (a) free spaceelectro-optic sampling; (b) photoconductive antenna. In both cases theTHz source is a singular electric field emitter with 20mW pump and 40V bias (~80μA).

As described in chapter 3, the photoconducting antennas are fabricated by conventional lithography on LT (low temperature) GaAs grown at ~250°C, and post annealed at 600°C for one minute. The metal patterns are deposited using one of the usual schemes for ohmic contacts on n-type GaAs (Au-Ge, Ni, Ti, Au). The lithography was optimized in order to provide as sharp features as possible. Fig. 4.3 inset shows a schematic diagram of the metal electrodes deposited on the structures.

First we measure and compare the THz emission intensity of each structure by using a standard coherent THz detection system with scanning capabilities on the emitter side.[31] The scanning ability enables us to trace the optimal excitation spot where the optical excitation is overlapped with the singular electric field near the sharp electrodes. The experiment setup is shown in Fig.4.1 in detailed and Fig.4.2(b) schematically. The peak and average THz power are calibrated with free space electro-optic sampling.[37] The experiment setup for the FSEOS is shown in Fig.4.2(a). On the emitter side, a short laser pulse (780nm, ~100fs) excites the sample through a 50X objective. The emitter is scanned with a spatial resolution of 0.4μm, and the terahertz signals are recorded for each pixel. The generated THz radiation is then collected with a pair of off-axis paraboloids. The detection side consists of a dual setup, antenna and free space electro-optic sampling. In the antenna detection scheme, the THz dipole antenna is fabricated on LT GaAs using a 75μm long and 20μm wide conventional dipole structure FF as shown in Fig.4.3 (inset) with a 5μm gap. A grid THz polarizer is inserted in the THz path and aligned with the detector to define the polarization of the detection perpendicular to the striplines. This antenna is gated by a delayed 780nm and 20mW short laser pulse. In the free space electro-optic sampling setup, a 2.2-mm-thick ZnTe crystal is used as a THz sensor [37], and probed with a 1.8mW laser pulse.

4.2 Performance Comparison in Terahertz Radiation Power of Various Designs

To take advantage of the singular electric field enhancement, the laser spot overlaps with one of the regions of highest electric field in the vicinity of one of the electrodes. This is

preferred to illuminating the whole gap region because doing this will require more optical power and eventually the total photocurrent is limited by the breakdown current. Fig.4.3 shows the measured peak THz power (proportional to the square of the peak THz electric field) of various structures for a fixed bias of 20V and for a 60μm dipole with a constant gap of 5μm. The excitation area is kept constant (~0.7μm in diameter) and we always excite the sharp singularities. Note that the conventional dipole antenna [34] also has areas of singular electric fields at the corners of the dipole edges. But in order to take advantage of this enhancement, the laser spot has to closely overlap these regions of high fields. Clearly, the sharpest triangular electrodes with a horizontal offset (pattern TT0, 5μm tip offset) give the highest emission intensity. Due to the high resistance of our samples and the small gap, we could apply a voltage as high as 60V (with a corresponding photocurrent of ~100μA) when exciting with several tens of mW of laser power. In that case, the electric field inside the 5μm semiconductor gap is as high as 120 kV/cm even if no singular electric field exists. According to the two dimensional static field simulations, the electric field can be a few times higher than that due to the shape of the electrodes and the lateral offset. This singular electric field is limited by the sharpness of the electrode edges obtained with conventional photolithography.

When the gap size is varied, emitters with sharp features and offsets consistently outperform other type of structures. Fig.4.4(a) shows the THz emission intensity for a few electrode structures with two different dipole lengths and as a function of the gap distance for a fixed 60V bias and 5mW excitation. When the gap distance is increased, the electric field decreases and hence the THz emission intensity. This is consistent with Fig. 4.4(a). The slope of this dependence varies with dipole length.

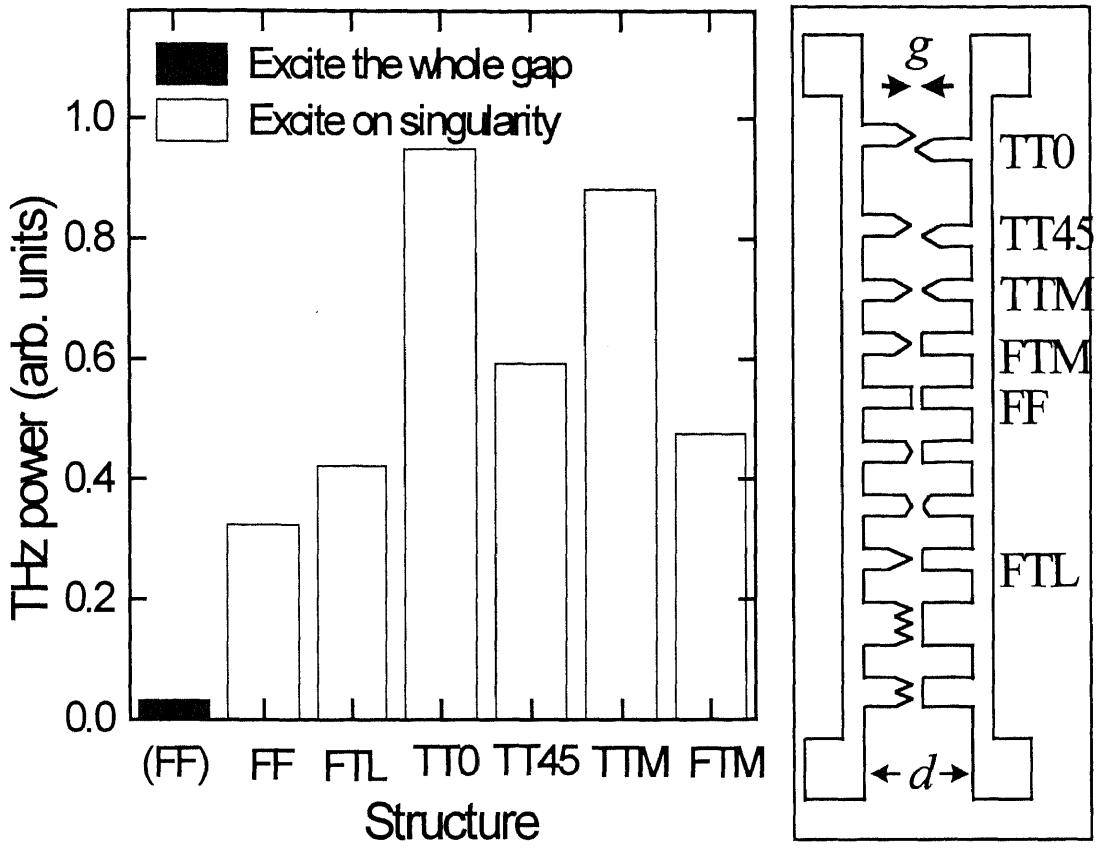

Fig.4.3 THz radiation power as a function of dipole structures measured in a 60μm dipole, 5μm gap, under 20V bias and 20mW excitation. Shown in the inset is a schematic diagram of the metal electrodes used in the new THz emitters and detectors.

4.3 Calibration of the Absolute Average Terahertz Radiation Power

As described in the previous section, the terahertz emitter radiation performance can be readily calibrated in conventional terahertz spectrometer setup shown in Fig.4.1 and Fig.4.2(b). We compared the radiation power from generator with different design approaches, and we found that the sharpest and horizontally offset structures with small gap size are the most efficient. But the an important specification for this high power terahertz generator - absolute radiation power level is still not available. In order to find out accurately how much terahertz radiation power of the terahertz beam generated by such structure, an other type of detection method has to be used.

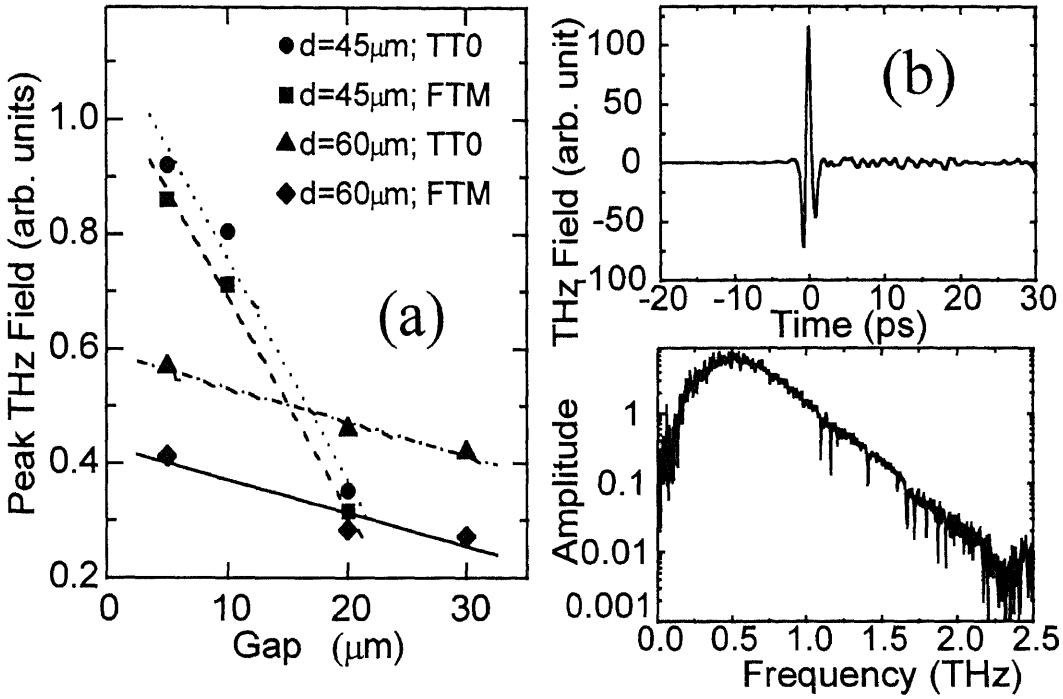

Fig.4.4 (a) peak THz field as a function of dipole length and gap distance with a fixed bias of 60V and 5mW excitation. The slope of this dependence varies with dipole length, but not electrode shape; The solid lines are fits to the experimental data; (b) a typical THz transient and spectrum when both emitter and detector have offset sharp shapes (TT0, 60μm long and 20μm wide dipole with 5μm gap).

An estimate of the power emitted by similar transmitters was roughly estimated by Van Exter et. al.[39], starting with the well-known equation for power emitted by a harmonically oscillating dipole in free space. But this method is far from direct. Several corrections have to be applied to this simple formula. First of all, the current, generated in the transmitting antenna through the creation of photocarriers, is nonharmonic. To calculate the emitted power they decompose the transient current into its Fourier components, and finally perform the frequency integration. Most of the radiation is emitted in the rising edge of the transient current and not in the 0.6 ps exponential decay time of the conductivity, which is equal to the carrier lifetime fro the radiation-damaged

silicon. (Note: it is less obvious in the case of our LT GaAs device with a ~0.2ps) Thus, the rise time is of vital importance and it proved to be slower than expected from the 70 fs laser pulse width. Using an exponential rise time as adjustable parameter, a good fit to the measured far-infrared spectrum was obtained with a rise time of slightly less than 200fs. As a second feature, it is important to note that the antenna is not an infinitely short dipole. The effective length of the antenna is probably more than the 30 μm separation for their device between the lines and depends on the current flow from the antenna into the transmission line. In the calculations an effective length of 35 μm is used. This length is roughly equal to a half wavelength of 1.5 THz radiation in the dielectric, resulting in a decrease in emission efficiency of about 50% and limiting the high-frequency end of the integration. As a last correction they mention that the antenna is situated at an interface between air and a dielectric medium with an index of refraction in the far infrared. It has been shown [59], that this situation results in an increase in emitted power by roughly a factor n when n is much bigger than 1. Furthermore, the emitted radiation is strongly directed into the dielectric and concentrated along the normal to the interface. The exact angular distribution of the radiation can be very complicated, [59,60,61] making it difficult to estimate the fraction of emitted radiation that is collimated into the THz beam. A first consideration is the reflection loss that occurs when the radiation is coupled through the silicon lens into the air. This reflection loss is about 30% at normal incidence. However, the angle for total internal reflection for silicon is 17°. Calculations show that with a spherical lens it is therefore impossible to capture more than 40% of THz radiation. [39] To estimate the actual fraction that ends up in the THz beam, a 5-mm-diameter diaphragm was placed in front of the silicon lens. As a result the power in the THz beam was reduced

by roughly a factor of 2. The diaphragm restricts the captured radiation to an emission cone of 19° (half angle). Calculations show the fraction of radiation within the cone to be only 7%, with reflection losses included. Consequently, they estimate that without the diaphragm only 15% of the total emitted radiation ends up in the THz beam, the rest being lost by (total internal) reflection and lens aberration. The complicated field profile at the dielectric lens diffracts out upon propagation to the paraboloidal mirrors roughly resembles a (Gaussian) TEM00 mode for each of the frequency components, with the diameter increasing as a function of wavelength. At a dc bias of 10 V and a laser power of 6 mW they found an average photocurrent of 1.1×10^{-6} A, corresponding to a peak current of about 1.8×10^{-2} A. Using this value and the method just described they calculate the total frequency-integrated power emitted by the transmitting antenna to be 75nW. Using their previously derived value of 15% to describe the coupling efficiency, they obtained 11nW in the collimated, freely propagating THz beam emitted from the transmitter. [39]

An alternative estimate of the transmitted power can be obtained at the receiving antenna, by combining the measured amplitude of the incident far-infrared field with the measured size of the focal spot.[39] The corrections that have to be applied are similar to those mentioned above for the transmitter, which makes the estimation equally indirect. Fist of all the response time of the receiving antenna is determined by its gating time and the rising timing of the transient conductivity. The Lorentz reciprocity theorem shows that the frequency dependence of the receiving antenna should equal that of the transmitting antenna [62]. Second, the boundary condition results in a complicated angular sensitivity of the receiving antenna and an increase in electric field by the factor $2n/(n+1)$ for radiation incident perpendicular to the interface. As a third and fourth correction they have

to mention the loss of high-frequency components due to the size of the antenna and the reflection losses at the front surface of the dielectric lens. Their measurements show that the size of the focal spot on the receiving antenna is wavelength dependent, being larger for longer wavelengths. The measured (FWHW) diameters of the focal spots were about 180 μm at 1.0 THz, 280 μm at 0.5 THz, and 460 μm at 0.25 THz. The deconvoluted induced peak voltage of about 35mV over the 35 μm antenna structure corresponds to a focused field of about 6 V/cm in the dielectric, if they correct for surface enhancement. These figures yield an average power of about 7nW in the air incident on the dielectric focusing lens of the receiver. This value is in reasonable agreement with the previously derived value of 11nW from the point of view of transmitter.

As described above, It is very hard to accurately estimate the power emitted by the terahertz transmitter, using the conventional photoconductive antenna detection technique. Besides the work horse (photoconductive dipole antennas) for free space terahertz beams detection, there are two other type of detection schemes available, liquid helium cooled bolometers and free space electro-optic sampling.

The liquid helium cooled bolometers is an incoherent detection technique. Compared to the coherent photoconductive antenna scheme, bolometers method do not provide phase information and have a lower sensitivity by three orders of magnitude. It is also a challenge to directly calibrate the bolometer in the terahertz / far infrared regime.

We calibrated the average power of the THz radiation using free space electro-optic sampling. [37] By using the wide bandwidth of the electro-optic crystal sensor, the high frequency cutoff problem associated with the dipole antenna can be avoided. And the flat simple shaped air/crystal interface allows accurate estimate of the reflection loss. In

the case of the dipole antenna detectors the coupling efficiency of the silicon lens is very hard to estimate, not only because of the shape but also the condition of the mount.

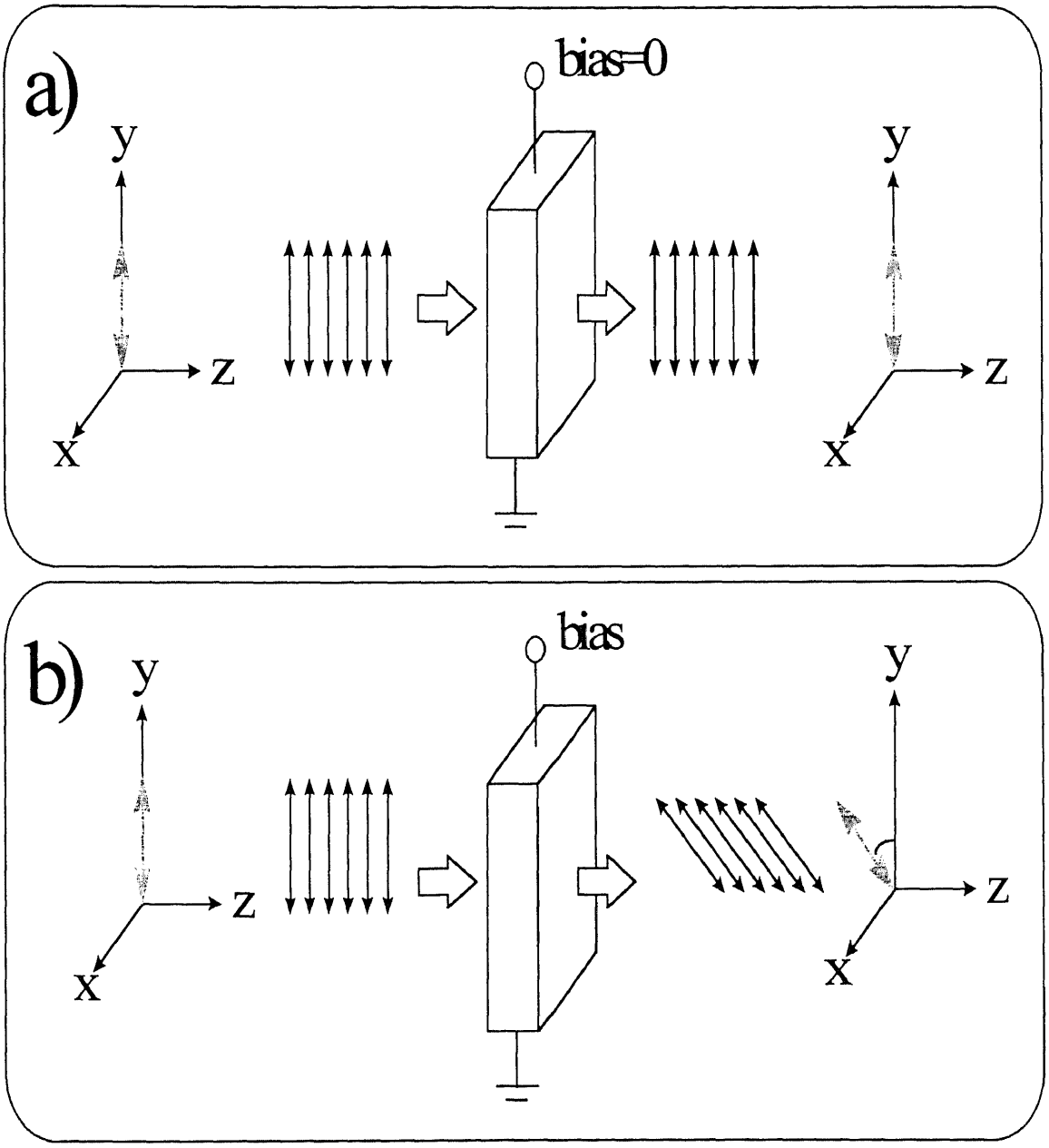

Fig.4.5 Operation principle of a electro-optic crystal: (a) the polarization of the incoming light remains unchanged through the unbiased EO crystal; (b) the polarization of the incoming light is rotated through the electrically biased EO crystal

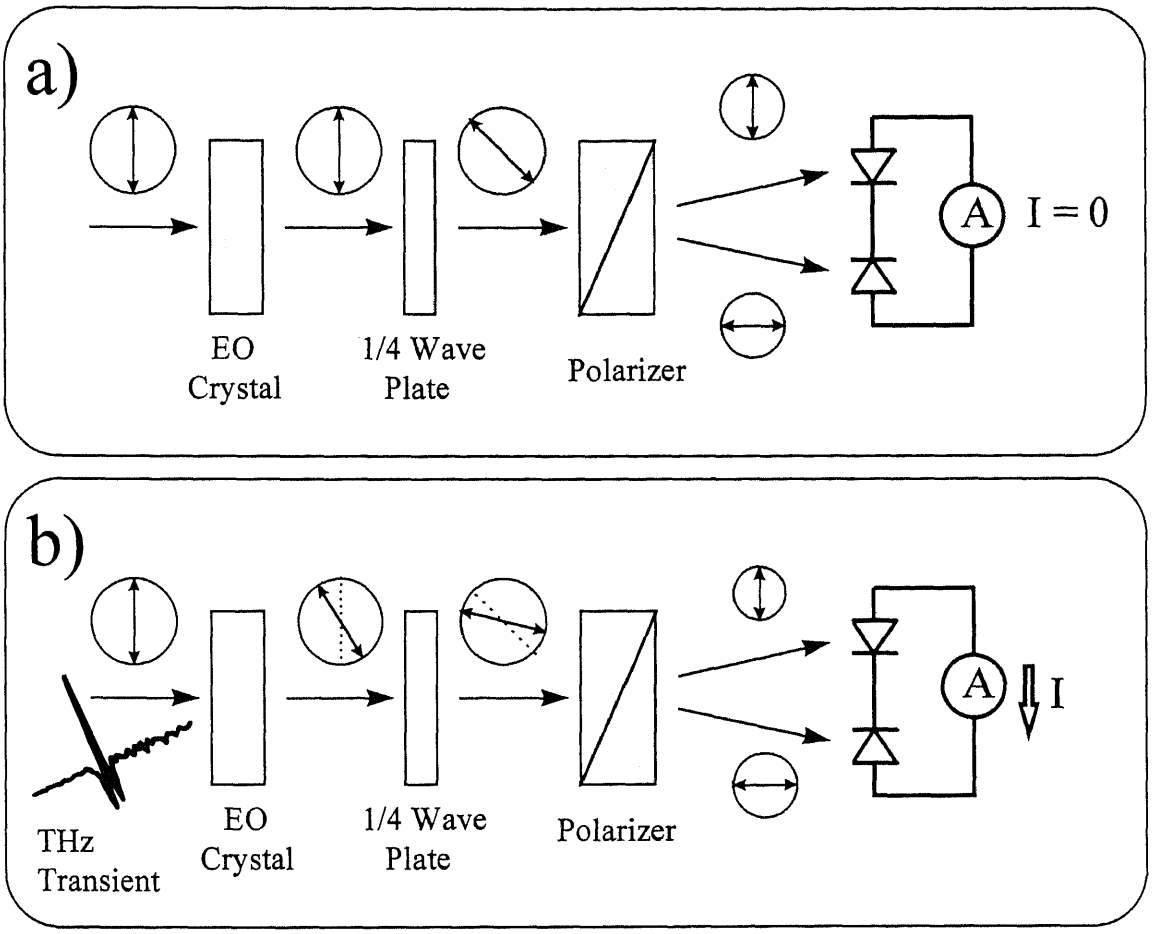

Fig.4.6 Operation principle of free space electro-optic sampling for terahertz detection: (a) the polarization of the incoming light remains unchanged through the unbiased EO crystal, and therefore no current flow in the balanced diode pair; (b) the polarization of the incoming light is rotated through the terahertz transient biased EO crystal, therefore light intensities on the diode pair are different. Current flow detected indicates the presence of the terahertz signal.

The principle for the operation of a electro-optic (EO) crystal is illustrated in Fig.4.5, where an electrical bias on the EO crystal induces a polarization rotation of the light passing through the crystal. In the free space electro-optic sampling terahertz detection experiment, the bias applied to the EO crystal is the transient terahertz electric field. This terahertz transient bias induces a small polarization rotation of the probing laser beam. When there is no terahertz transient bias, the probing light polarization remains the

same after passing through the crystal. A quarter wave plate and a Wollaston prism split the beam into two beams of equal intensity onto a pair of matched photo diodes. There will be no current flow when balanced, because the two diodes are connected back to back. The common mode noise is canceled by the diode pair. But when the terahertz transient impinges on the EO crystal, the polarization of the probe beam is modulated. And the polarization change breaks the balance of the two beams illuminating the diode pair. A net current can be detected under this situation. The principle of the free space electro-optic sampling is illustrated in Fig.4.6.

Fundamentally, the electro-optic effect is a nonlinear coupling between a low frequency electric field (terahertz pulse) and a laser beam (optical pulse) in the sensor crystal. Modulating the birefringence of the sensor crystal via an applied, polarized electric field will modulate the polarization ellipticity of optical probe beam passing through the crystal. The ellipticity modulation of the optical beam can then be polarization analyzed to provide information on both the amplitude and phase of the applied electric field (terahertz wave). Although the detection bandwidth of the EO crystal is much higher than the photoconductive sampling with Hertian dipole detectors, the sensitivity is not as high as the dipole detectors. This is because the interaction between the terahertz pulse and the probe laser pulse is limited to a very small distance (less < 1mm). This distance can not be increased by the use of thick EO crystal sensors, because the different refractive index for the terahertz (0.3mm FIR) and probe laser beam (800nm IR) are different. The velocity mismatch limits the interaction length and therefore sensitivity. So far the ZnTe crystal, where n(800nm)=2.853, and n(0.3mm)=3.178, provides the best tradeoff in group velocity matching and figure of merit for the EO crystals. [6] The group velocity mismatch is about

1ps/mm between the optical probe and the terahertz radiation in ZnTe. The optical beam travels faster than the THz radiation. So unless a crystal thinner than 0.5mm is used, the true terahertz waveform can not be obtained, assuming the THz radiation bandwidth is less than 2THz. Of course, the effective interaction length in a thick crystal can also be reduced by focusing one of the beams or by other methods to reduce the overlap of the two beams.

We use this free space electro-optic sampling technique to calibrate the absolute average power for the terahertz radiation emitted from our new dipole antennas. Assuming perfect velocity matching in the ZnTe crystal and using the experimental value of $\Delta I/I = 0.7\times10^{-3}$ for the change in photocurrent resulting from the polarization rotation, we obtain the peak electric field for the THz radiation. For a 45μm dipole under 20mW incidence and 40V bias (80μA photo current), the peak electric field is about 57V/cm, which leads to an average power density of 13.7W/cm^2 in free space. With a THz spot size of ~0.5mm and a duty cycle of 10^{-4}, the average THz power is about 2.7μW. [38] The operation under this power level does not affect the device lifetime or stability, which is primarily limited by the photocurrent level. In our case, the device lifetime will be reduced under continuous operation above 110μA.

4.4 Performance as Detectors and System Bandwidth Calibration

We also tested the performance of the singular electric field emitters as detectors. When using the structure TT0 in Fig. 4.3 (inset) with a 60μm long and 20μm wide dipole partially illuminating the 5μm gap near one of the sharp electrodes, the THz electrical field detected is increased by ~40% when compared to a conventional dipole (structure FF in

Fig.4.3 inset), without any appreciable increase in the noise level, as shown in Fig.4.7. [29,30] The frequency response was also comparable.

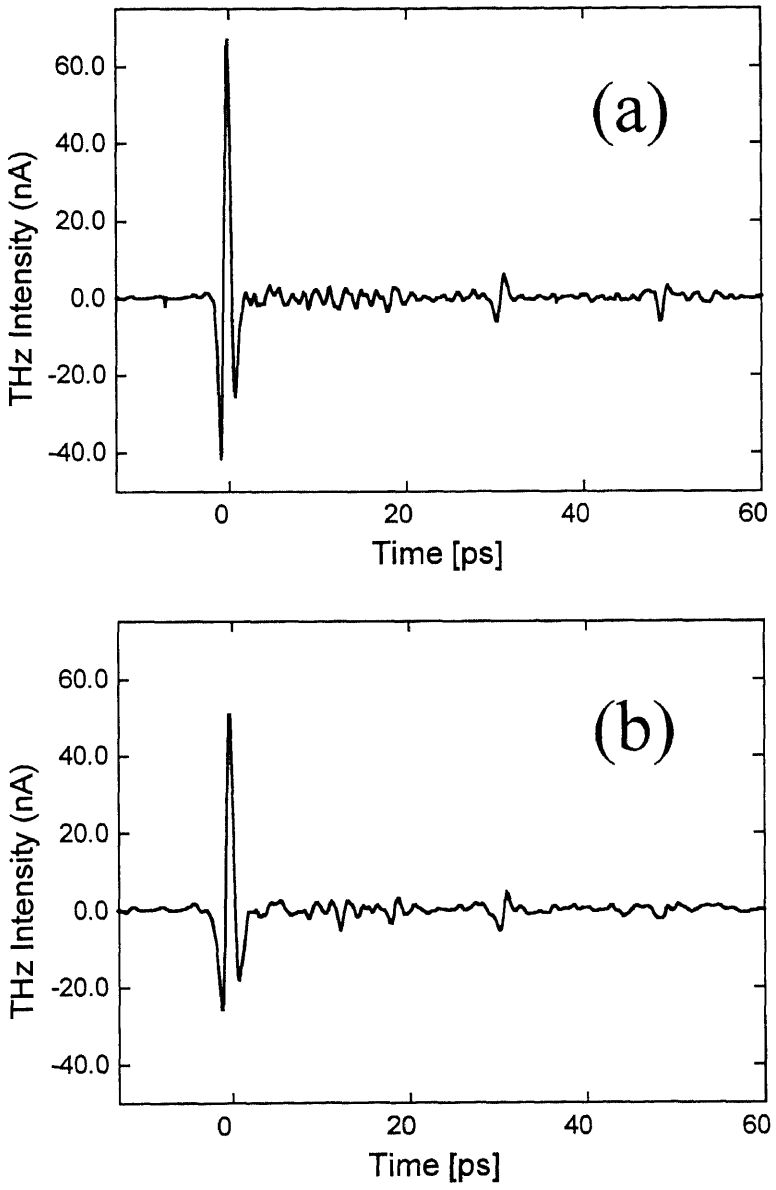

Fig.4.7 The THz signal detected using (a) offset dipole singular electric field detector; (b) regular dipole detector. The offset singular detector yields ~40% improvement over the regular dipole already using its singularity at the edge of the electrode.

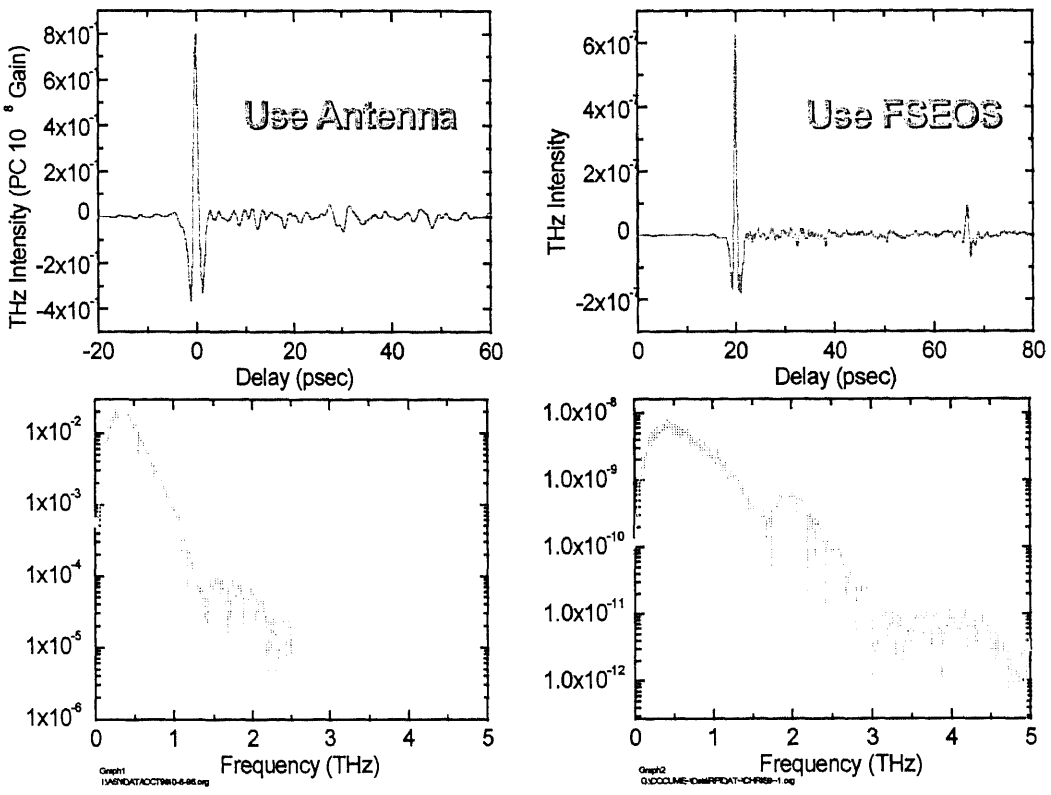

Fig.4.8 Comparison of time and frequency domain of the terahertz waveforms for (a) antenna detection with a 75μm LT GaAs dipole; (b) free space eletrio-optic smapling detection with a ZnTe crystal. A *60μm* dipole singular electric field emitter with a 5μm gap, under 40V DC bias and 20mW optical excitation, is used as the THz source.

Fig.4.3(b) shows a typical THz waveform and spectrum when both emitter and detector have offset sharp structures (TT0) as described above. The bandwidth extend beyond 2THz. Note that it is not the true bandwidth of the terahertz generated from the dipole emitter, because the dipole response of the receiver is limiting the system bandwidth.

However the true bandwidth can be calibrated using free space electro-optic sampling method, where the flat frequency response of the electro-optic crystal is much higher than the THz radiation bandwidth from dipole emitters. Fig.4.8(b) shows the true

bandwidth of the terahertz radiator is between 4-5THz. But with a dipole antenna the detection is limited at 2-3THz, as shown in Fig.4.8(a).

4.5 New Phenomena Discovered in the Characterization of the New Structures

4.5.1 Symmetric/Asymmetric Excitation Patterns as a Function of Gap Size

It was previously observed by many groups that the process of THz generation in biased structures (with gaps ranging from several tens of μm to a few cm) becomes particularly efficient when excited close to the anode.[31,32,33,34] However, a symmetrical THz emission intensity was reported for very large gap (3cm) structures.[35] The two-dimensional scans of the THz emission in our small gap structures also show an absence of this asymmetry. [29,30] This is shown in Fig.4.9 for several emitters (gaps of 5, 10, 30 and 90μm) where we plot a two-dimensional scan of the peak THz electric field when scanning the emitter and keeping the exciting beam fixed. When the gap is small (5, 10μm), the two-dimensional scan of the THz emission is perfectly symmetrical. A gradual transition to the positive electrode effect is observed for gaps larger than 20μm. For a 30μm gap, a slight asymmetry is observed. When the gap is very large (90μm), the asymmetry becomes very clear. This is opposite to earlier results of electro-optic sampling in coplanar striplines.[33]

At this point, the mechanism which causes this varying asymmetry as a function of gap size is unclear. However particular mechanisms may be ruled out based on our results. No significant change in this asymmetry is observed when we chop the electrical bias up to 100KHz. These high frequency bias results preclude the formation of Gunn domains (~1ms build up time) [35] and any static or quasi-static effects. We also found no change

in these results when the bias is changed from fractions of a volt to close to 100V. Other groups have reported the "positive electrode effect" in different materials such as SOS [32,36], semi-insulating GaAs [34], low temperature GaAs [31,33], n- and p-doped GaAs [33] and InP [10]. This indicates that the material details may not be responsible for this phenomena. It has been suggested that the trap-enhanced electric fields [34], resulting from the electrical and optical carrier injection, are responsible for the asymmetric field distribution in a gap of 80μm between two coplanar striplines. The region near the forward biased positive contact experiences an accumulation of electrons and a depletion of holes which is strongly enhanced by electron velocity saturation and geometric effects. The increased electron density results in larger electron occupancy of the deep traps. The current-voltage characteristics measured by the same group [34] also indicates this double injection current transport effect is reduced in smaller gaps (50μm). Our results neither support nor preclude this explanation, as these current-voltage measurements should be done with extreme care and removing most of the metal striplines.

4.5.2 Polarization of the THz Radiation as a Function of Emitter Structures

We also measured the dependence of the polarization of the THz radiation as a function of the offset angle and for different gap sizes. Due to the lateral offset of the electrodes, the carrier transport direction will be different in each structure. A grid THz polarizer is inserted in the THz path and aligned with the detector to define the polarization of the detection.

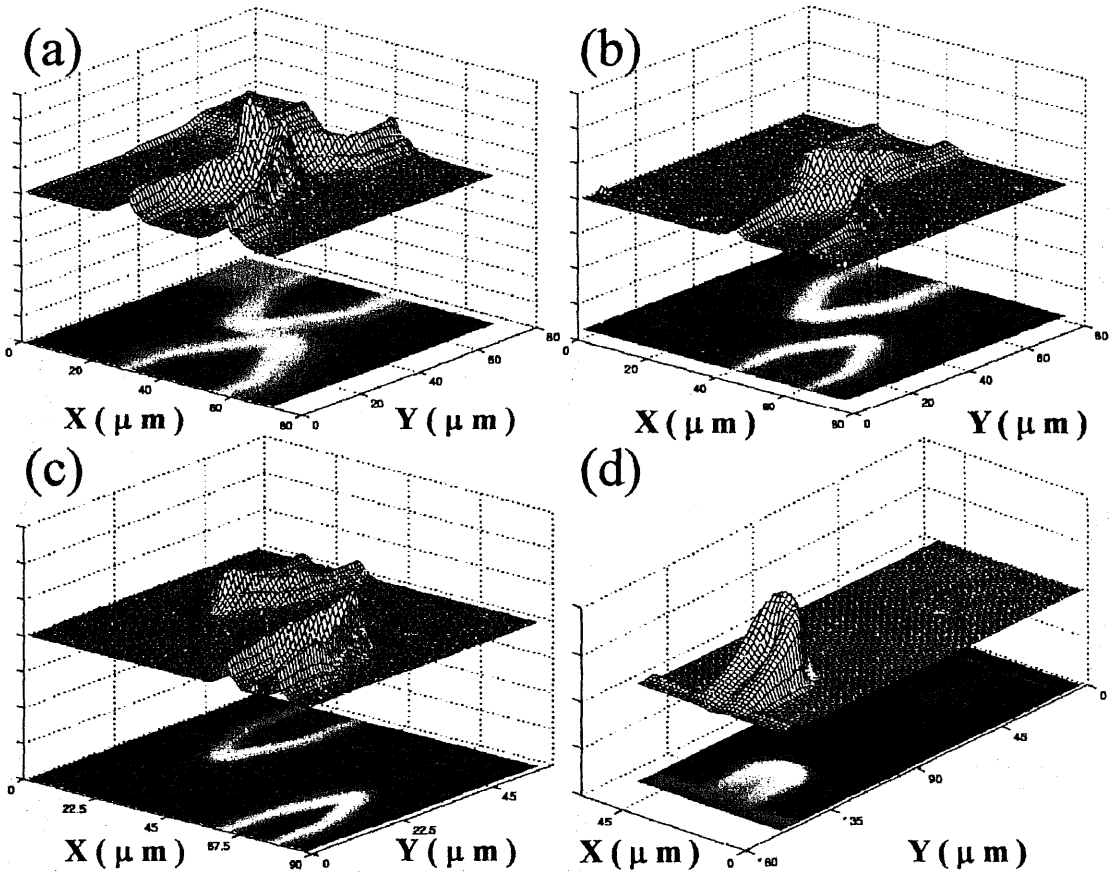

Fig.4.9 Two dimensional scans of the THz emission intensity from several singular electri field offset dipole emitters with gaps of (a) 5, (b) 10, (c) 30, (d) 90μm. The small-ga emitters in (a) and (b) show perfectly symmetrical THz emission; the 30μm gap emitter (c shows a slight asymmetry, and the THz emission from large gap emitters (d) is clearl asymmetrical, enhanced near the anode.

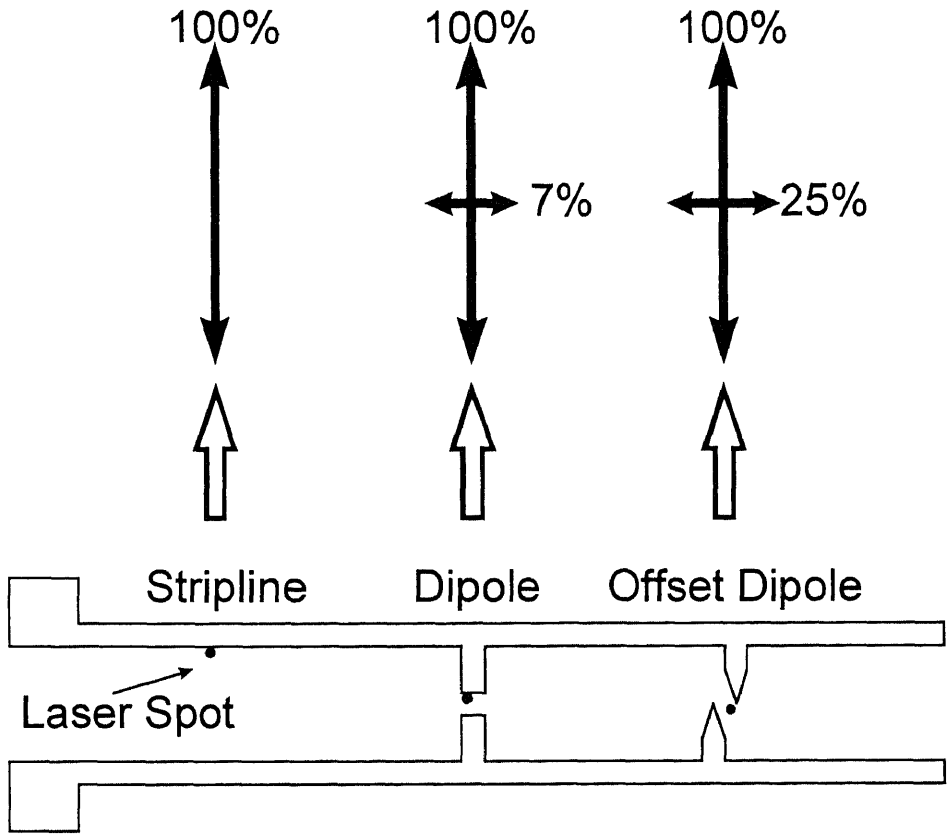

Fig.4.10 A comparison of the polarization of the THz emission from stripline, conventional dipole and offset dipole emitters. The percentage of the lateral electric field is relative to the vertical electric field in each structure. The difference is related to the direction of the carriers' flow in the semiconductor. It indicates that the THz generation in biased photoconducting antennas is determined to a large extent by carrier dynamics rather than nonlinear effects.

Three different structures are studied: a regular coplanar stripline, a conventional dipole and an offset dipole like those described earlier. The direction of the polarization is consistent with THz radiation emitted from accelerating carriers towards the other electrode. The stripline emitter gives very well polarized radiation while photoexciting near one of the metal lines. A conventional dipole (FF) shows a small (~7%) orthogonal electric field component. The THz radiation from the offset dipole has a considerable (~25%) orthogonal electric field component as shown in Fig. 4.10. [29] Therefore, the offset dipole structure not only gives the strongest radiation power in the dipole direction

but also in the orthogonal direction. This polarization rotation does not scale up proportionally to the offset angle or the gap size. This is consistent with the well known current surge model. In the offset dipole structure, the carriers' flow is tilted with respect to the stripline. In such offset structure, while the THz wave is generated in the semiconductor, it has components in both polarization directions, but only one direction is enhanced by the dipole formed by the straight electrode lines. Therefore the polarization of the THz emission from stripline and offset dipole emitters is related to the directions of the carriers' flow in the semiconductor as shown in Fig.4.11. [4]

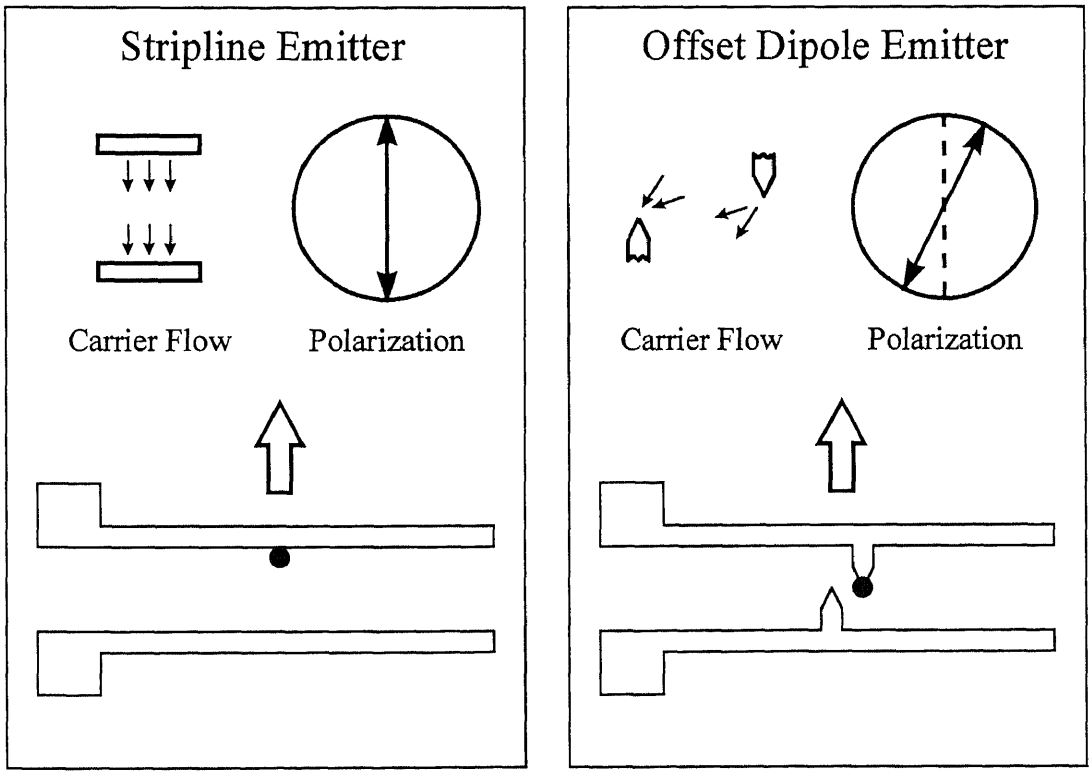

Fig. 4.11 The polarization of the THz emission from stripline and offset dipole emitters is related to the directions of the carriers' flow in the semiconductor. The THz radiation from the offset dipole has a considerable (~25%) orthogonal component.

4.6 Summary

In conclusion, we studied the performance of a new family of terahertz emitters and detectors based on electric field singularities with small gaps. We demonstrated that the THz emission efficiency can be improved by optimizing the singular electric field experienced by the photo-generated carriers. The highest efficiency is obtained using laterally offset sharp triangular electrodes, with a typical THz average power of 2~3μW under 20mW optical gating. [29] This is the most efficient emitter to our knowledge for excitation power in the mW range. Previous reported THz radiation powers of photoconductive switches are 38nW [39] and 10nW [25]. The enhancement originates from the higher electric field near the sharp electrodes. It has been estimated to be about 3~5 times higher than normal by simple 2-D static electric field simulation, and the radiation power is proportional to the square of electric field. The polarization direction of the emitted THz radiation follows the direction of carrier transport rather than the dipole orientation. These THz emitters also work as more efficient THz detectors. [29,30]

CHAPTER 5

IMPROVEMENT TO THE TERAHERTZ SYSTEMS BY USING SINGULAR ELECTRIC FIELD TERAHERTZ ANTENNAS

With the singular electric field terahertz emitters that reach the record high μW power level, we are able to impact terahertz spectroscopy / imaging technology with even higher band width, sensitivity, spatial resolution, and compactness. In this chapter, we demonstrate these improvements, where the singular electric field antenna played an important rolls. Of course the new antenna is not the only reason for these technological advances. We also used other techniques to make all these improvement possible. The purpose of this chapter is to demonstrate how the newly enhanced antenna can be integrated into various aspect of terahertz technology.

In the first section, we present a new approach for THz free space electro-optic sampling (FSEOS) system to reach shot noise limited detection. And we demonstrate the feasibility of a THz focal plane imaging system using real time delay scanning in FSEOS with our new THz source that, for the first time, requires only 20mW of laser power. The previous system using completely different approach requires more laser power and a strictly low noise laser.

We present new terahertz imaging probes with the highest spatial resolution to date, using near field techniques. The probe integrates the terahertz source in the front side of the wafer and aperture for near field imaging on the back side. The new high power emitter is used to compensate the power loss by including the sub-wavelength sized aperture.

In the third section, the improvement in performance of THz spectroscopy systems by combining the highly efficient THz generators and detectors with high speed modulation (90kHz) lockin detection is described. A modulation depth as low as $\sim 10^{-6}$, or as high as $\sim 10^{6}$ in term of signal to noise ratio, is achieved in our THz system with 1s time constant for the lock-in detection.

We demonstrate a compact all solid-state terahertz system in section 4, operating with a diode pumped Cr:LiSaF laser. The high efficiency of the new terahertz antenna is essential for the operation of the system, because of the relatively low excitation power this laser can provide.

5.1 High Frequency Modulated Lockin Free Space Electro-optic Sampling: a Real Time Delay Scanning Ultra Wide Band Terahertz Focal Plane Imaging System

In this section, we first compare the use of free space electro-optic sampling (FSEOS) with photoconducting antennas to detect terahertz (THz) radiation. For the same average THz power, signal to noise ratio and sensitivity are better with antenna detection whereas FSEOS detection can have as much bandwidth as the inverse of the laser pulse width. Using a singular-electric field THz emitter, we demonstrate the feasibility of a THz imaging system using real time delay scanning in FSEOS and only 20mW of laser power. With our new radio frequency chopping implementation the FSEOS detection is close to the shot noise limit. Further improvement on the SNR can only be accomplished by increasing the THz power. Our improved signal to noise ratio, that enables real time scanning T-ray imaging, is clearly a result of using the more powerful singular electric field emitters. As described in chapter 4, we also calibrate the new THz emitters with FSEOS.

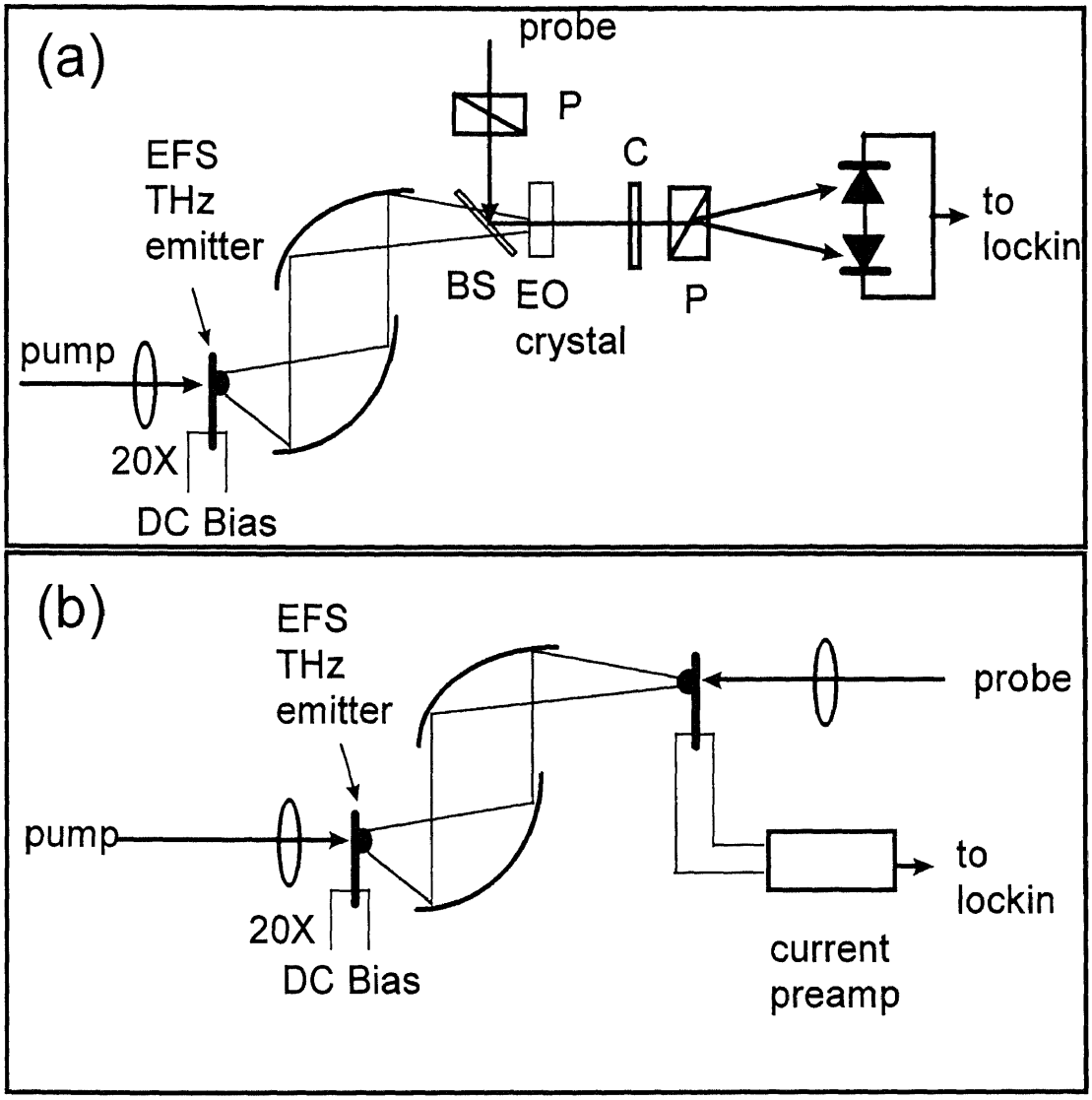

Fig.5.1 Experimental setup: (a) free space electro-optic sampling; (b) photoconductive antenna. In both cases the THz source is a singular electric field emitter with 20mW pump and 40V bias (~80μA photo current).

Traditional coherent terahertz (THz) detection schemes involve the use of gated photo-conducting antennas as detectors for freely propagating THz electromagnetic waves. This is true both for THz spectroscopy [17,25,29,31,39] and for THz imaging systems [26]. Recently, some groups have used free-space electro-optic sampling (FSEOS) as an alternative detection scheme.[37,63,64,66] The advantage of the latter is

the higher detection bandwidth that can be as high as 37THz.[65] Although previous reports of FSEOS measurements showed reasonable signal to noise ratios (SNR), a detailed comparison between both techniques for the *same* laser power is still missing. It is one purpose of this dissertation to present such a comparison, especially in the limit of low laser power and to show the feasibility of a real time imaging system based on FSEOS and high frequency chopping.

In order to carry out this comparison, we use a compact THz system with a common generator and dual detection capability as shown in Fig.5.1. Both pump and probe beams are derived from a mode-locked Ti:sapphire laser (100fs, 800nm). The emission of freely propagating THz waves is achieved by exciting a singular-electric field photoconductive antenna [29,31] with pulses from this laser. This emitter was fabricated on low temperature GaAs (LTG) with dipole lengths of 45 and 60 μm and biased at ~40V. The excitation power is kept fixed at 20mW. The detection side consists of a dual setup. Fig.5.1 (a) shows the FSEOS setup where the detector is a 2.2mm thick ZnTe crystal. A pair of balanced photodiodes is used to analyze the polarization rotation that the THz field induces in the visible probe beam. Fig.5.1 (b) shows the antenna (75μm LTG dipole) detection scheme. The probe power used in the FSEOS detection is 1.8mW (0.9mW on each photodiode). In the antenna detection scheme, we use a 20mW laser beam to gate the antenna.

When the chopping frequency is kept at a few kilohertz, the antenna detection scheme always has a better SNR (almost 2 orders of magnitude in our system). The electro-optic sampling technique is very sensitive to laser noise, which can be quite substantial in an Ar-pumped Ti-sapphire laser and at low frequencies. This is because one

has to detect very small changes in polarization (typically ~10^{-4}-10^{-5}). The antenna detection scheme detects a dramatic photocurrent change induced by the THz field. The laser noise influence can be overcome by modulating the visible pump beam at high frequencies (1MHz). This typically lowers the laser noise by ~30dB. Chopping at such high frequencies cannot be done in the antenna detection scheme though because the high gain transimpedance amplifiers required to amplify the photocurrent typically only have a low frequency response.

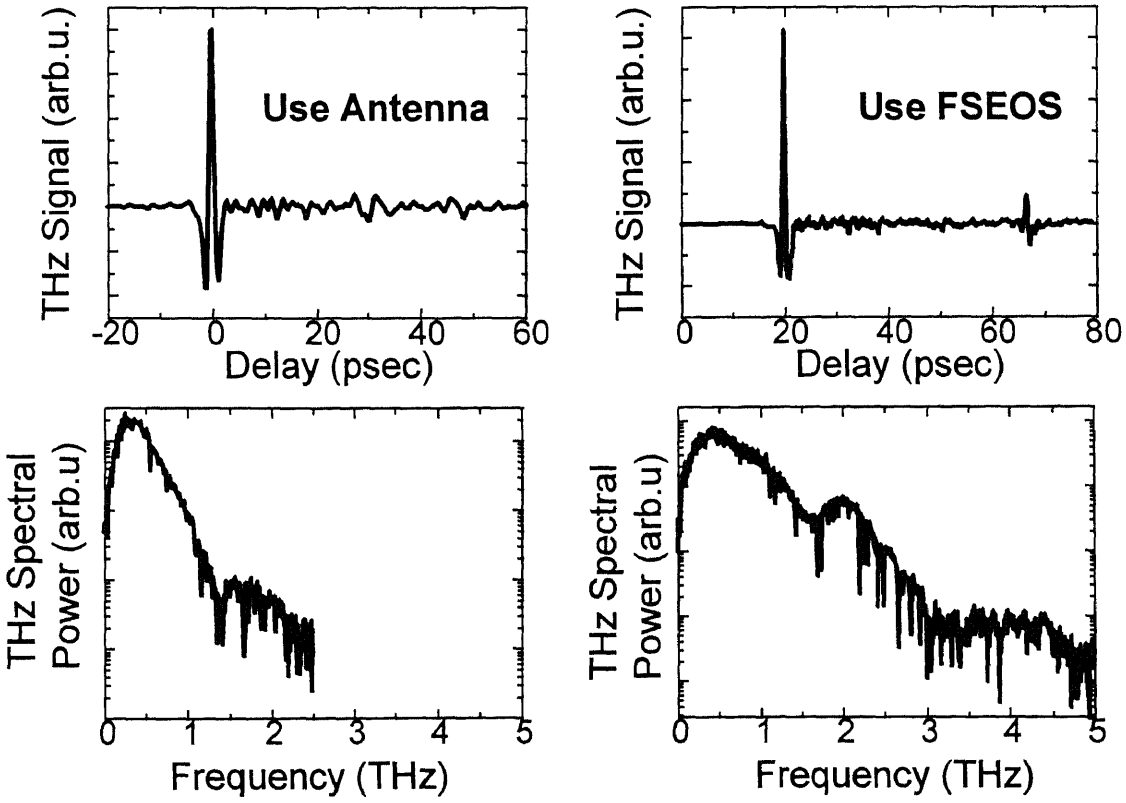

Fig.5.2 Comparison of time and frequency domain of the terahertz waveforms for (a) antenna detection with a 75μm LT GaAs dipole; (b) free space eletrio-optic smapling detection with a ZnTe crystal. A *60μm* dipole singular electric field emitter with a 5μm gap, under 40V DC bias and 20mW optical excitation, is used as the THz source.

After the chopping frequency is optimized (~1MHz), the measured THz signal has a SNR $>10^4$ in the electro-optic sampling detection scheme when acquired with a 100ms time constant. This becomes comparable to the performance of the antenna detection. Even with a short 1ms time constant, the SNR is till $\sim 2\times10^3$. That makes the THz imaging using real time delay scanning feasible with FSEOS, just like with antennas. In the electro-optic sampling case, as shown in the later section of this chapter, the balanced photodiode pair already works close to the shot noise limit. Therefore the improved SNR is the contribution from more THz power generated by our more powerful singular electric field photoconductive antenna [29,31].

Even when the THz generation is carried out in photoconductive switches that inherently have a low frequency response (<4THz), the higher bandwidth of the electro-optic detection is evident. This is shown in Fig.5.2 and Fig.5.3 where we compare the performance of both systems using a 60μm dipole singular electric field emitter with a 5μm gap (Fig.5.2) and a shorter 45μm dipole with a 5μm gap (Fig.5.3). The roll-off beyond 0.5THz is due to the response of the emitter. The FSEOS results indicate that the real response of these emitters has a much slower roll-off that extends beyond 3-4THz, while the antenna detection cuts off at 2THz. Previous reports of THz detection by FSEOS with high SNR (~10^4 [64], comparable to our results with 1MHz chopping) or wider bandwidth (~7THz) [63], required much more laser power (i.e. ~1.5W [63]) pumping a non-resonant unbiased THz source. Further increase of bandwidth (upto 37THz) [65]an be achieved at the expense of lowering SNR.

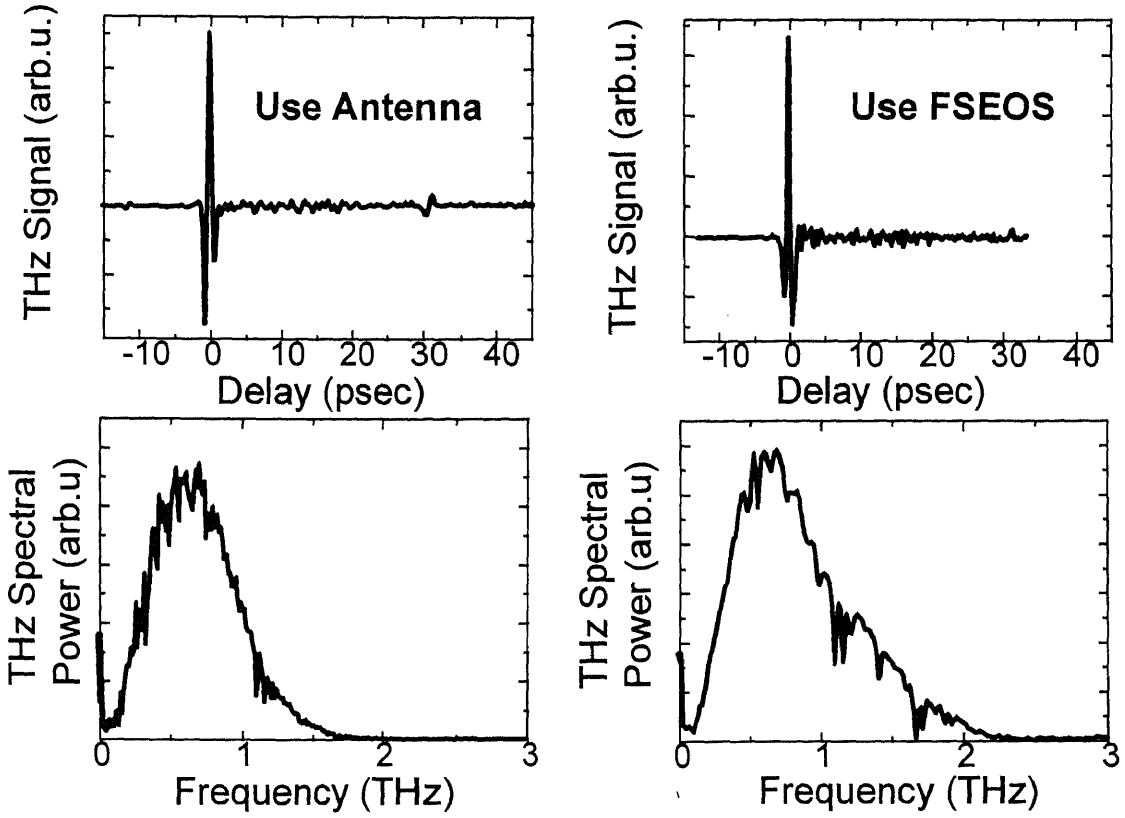

Fig.5.3 Comparison of time and frequency domain of the terahertz waveforms for (a) antenna detection with a 75μm LT GaAs dipole; (b) free space eletrio-optic smapling detection with a ZnTe crystal. A *45μm* dipole singular electric field emitter with a 5μm gap, under 40V DC bias and 20mW optical excitation, is used as the THz source.

In electro-optic detection there is a clear trade-off between sensitivity and frequency response that is determined by the choice of crystal and its thickness. A thicker crystal produces a longer interaction length, but on the other hand it reduces the frequency response due to group velocity mismatch. Due to the dispersion in ZnTe, where n(800nm)=2.853 and n(300μm)=3.178, the group-velocity mismatch is around 1ps/mm between the optical probe and THz radiation.[37] Our electro-optic crystal is quite thick (2.2mm), but due to the use of paraboloids to focus the THz radiation in the crystal, the effective interaction length is determined by the corresponding depth of focus of the THz

beam. [66] Assuming the THz beam is focused onto the sensor crystal with diffraction-limited spot size, the effective thickness of the crystal is comparable to the FIR wavelength. The product of this effective crystal thickness and group velocity mismatch should be less than the pulse duration to obtain the actual THz waveform. Besides this dispersion effect, the high frequency response of the electro-optic crystal is limited by the first TO phonon resonance of the crystal (5.3 THz for ZnTe) [37]. The bandwidth of the antenna detection process is also determined by two factors, the photocurrent response (i.e. carrier lifetime) and the frequency-dependence of the antenna structure. In general, the low-frequency cutoff of the detectors results from the collection efficiency of the dipole, while the upper frequency limit is determined by the photocarrier response. The photocurrent response is the convolution of the transient photoconductivity and the THz electric field across the semiconductor.

One important point of comparison is the performance of both techniques in a terahertz imaging setup using rapid delay scanning and measuring the time dependence of the THZ waveforms in real time.[26] This operation mode is easily achieved with the antenna detection but it is not obvious in FSEOS. We will show that real time scanning can be used in FSEOS detection provided that the appropriate chopping techniques are used. The experimental setup is shown in Fig.5.4: a frequency synthesizer generates two synchronized frequencies at 0.9 MHz and 0.9007 MHz. An acousto-optical modulator (AOM) modulates the pump beam at 0.9MHz. The lockin amplifier is referenced at the difference of the two frequencies through RF mixing, and operates at a low time constant $\leq$1ms. The real time waveform is measured at the analog output of the lockin amplifier and captured on an oscilloscope.

With a typical photocurrent of 1mA on the photodiode, the shot-noise limited relative noise floor is 20pA/Hz$^{1/2}$. After increasing the chopping frequency to 0.9 MHz, we found that the noise floor in the measured signal is around 110pA/Hz$^{1/2}$, only 5 times of the shot noise. This makes the FSEOS technique reach a comparable SNR in terahertz imaging using real time delay scanning, but with much higher detection bandwidth. Compared to the antenna detection scheme, more supporting equipment is required in the FSEOS setup, but this could be conceivably integrated into one unit.

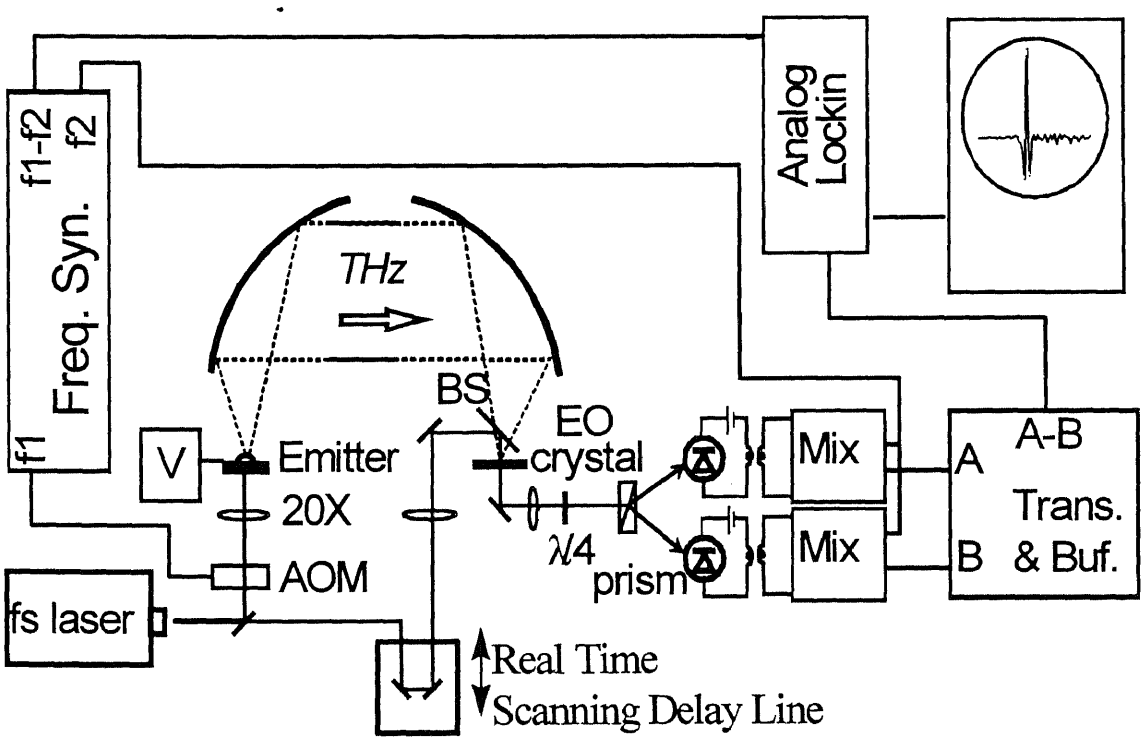

Fig.5.4 Experimental setup using mixer based MHz chopping and fast phase sensitive detection for real time free space electro-optic sampling. The frequency synthesizer generates two synchronized frequency at 0.9MHz and 0.9007MHz. The AOM modulate the pump beam at 0.9MHz. The lockin amplifier is referenced at the difference of the two frequencies through RF mixing, and operates at a low time constant ≤1ms. The real time waveform is captured on an oscilloscope. This radio frequency narrow band detection method can eliminate the 1/f low frequency noises and achieve shot noise limited detection.

Table 5. 1 Comparison Between Free Space Electro-optic Sampling Versus Photoconducting Antenna Detection

	Free Space E.O. Sampling	Antenna Detection
Power requirement	25mW	40mW
Signal to noise ratio [a]	10^4	10^4
Bandwidth	3 - 7 THz	1 - 2 THz
Real time scanning	Yes [b]	Yes
MHz chopping	Yes	No
Supporting equipment	Some	Minimal
Real time scanning total system cost	++	+
Stability	++	+
Ease of alignment	++	+

[a] With lockin detection of 100 ms time constant
[b] Provides that fast chopping and a fast lockin are used

Finally, the use of FSEOS detection allows us to calibrate the THz electric field and power emitted from singular electric field emitters. The THz beam is focused on the crystal with a spot size of ~0.5mm in diameter. The corresponding depth of focus determines the maximum effective thickness of the crystal. The calculated half wave field E_π is 91kV/cm, where the Fresnel loss is considered. Assuming perfect velocity matching in the ZnTe crystal and using the experimental value of $\Delta I/I = 0.7\times10^{-3}$ for the change in photocurrent resulting from the polarization rotation induced by the THz transient field, we obtain an electric field of 57 V/cm for the THz field. This corresponds to a THz power density of 13.7 W/cm^2. For a THz spot size of 0.5mm and a pulse duty cycle of 10^{-4}, the average THz power detected is 2.7μW. This is the most efficient emitter reported up to date under low optical power excitation. Previous reported THz radiation power values

from photoconducting antennas are 38nW [39] and 10nW [25], under 5-10 mW of optical excitation. Using optical rectification from unbiased GaAs, a typical average power of 0.3μW under 1.5W excitation has been reported. We also calibrated the true frequency response of such emitters with FSEOS. The near 4THz usable bandwidth is primarily limited by the lifetime of photo-generated carriers. This is consistent with the lifetime (~250fs) of our LTG measured using pump and probe time-resolved reflectivity.

In conclusion, a comparison between the two coherent THz detection techniques (FSEOS and antenna detection) is presented in Table 5.1, with an emphasis on single-pixel terahertz imaging. We showed that the FSEOS system can be used in real time single-pixel THz imaging with comparable SNR and larger bandwidth, when fast chopping and a fast lockin are used. Using the FSEOS setup, we also calibrated the THz power and bandwidth being radiated from singular electric field emitters. These emitters produce far-infrared radiation with an average power of ~3μW under 20mW of visible pumping.

5.2 Near Field Probes: the Highest Spatial Resolution for Terahertz Imaging

In this section, we present three new designs of integrated terahertz near field imaging probes for sub-wavelength spatial resolution. The new designs either integrate a 25 μm aperture on the back of a photoconductive antenna, and/or use a 100 μm thin wafer to enable the placement of a sample extremely close to the source. The sample can be conveniently scanned on the back of the integrated near field emitters, resulting in a simpler setup and alignment than using terahertz near field tips. A less than 50 μm spatial resolution terahertz image is obtained with the new device.

With the new development on real-time T-ray imaging, Time-domain Terahertz Spectroscopy (THz-TDS) has extended its applications from an extremely valuable and sensitive tool for materials studies to a variety of analytical imaging applications such as: chemical mapping, and a host of commercial applications such as safe package inspection, industrial process control, food inspection, biology and medicine.[26] But due to the long wavelength of the THz radiation, the spatial resolution is essentially limited by diffraction to several hundred micrometers and frequency dependent over the large bandwidth of the THz pulses. We have recently shown a near field imaging approach to create high-resolution "T-ray" images. In previous work, the near field probe was made with a small conical aluminum tip with a Cr/Ni alloy. Removal of the aluminum cone and polishing of the Cr/Ni tip results in the small, circular aperture. The probe is then placed at the focal point of the THz beam. A resolution of 140 μm was obtained with the tip probe. [53] In this work we describe three kinds of new designs of near field probes. The first new design integrates the aperture for near field imaging on the THz photoconductive antenna. We name this configuration as Integrated Backside Aperture (**IBSA** as shown in Fig.5.5a), an analogy to the optical near-field probes. The second design uses a 100μm thin wafer to reduce the distance between the short antenna and sample for near-field operation. It is called Thin Wafer No Aperture (**TWNA** as shown in Fig.5.5b). The last design is using SOS substrate to enable backside optical excitation (**BSOE** as shown in Fig.5.5c) to reduce the distance between the antenna and the sample. The IBSA and TWNA designs are analogies to microwave near-field probes. All designs eliminate the needs for refocusing the THz beam to incorporate the near field tip. The sample can be conveniently

scanned on the back of the integrated THz near field emitter for high resolution images. Therefore the setup is simpler and easier to align than using near field tips.

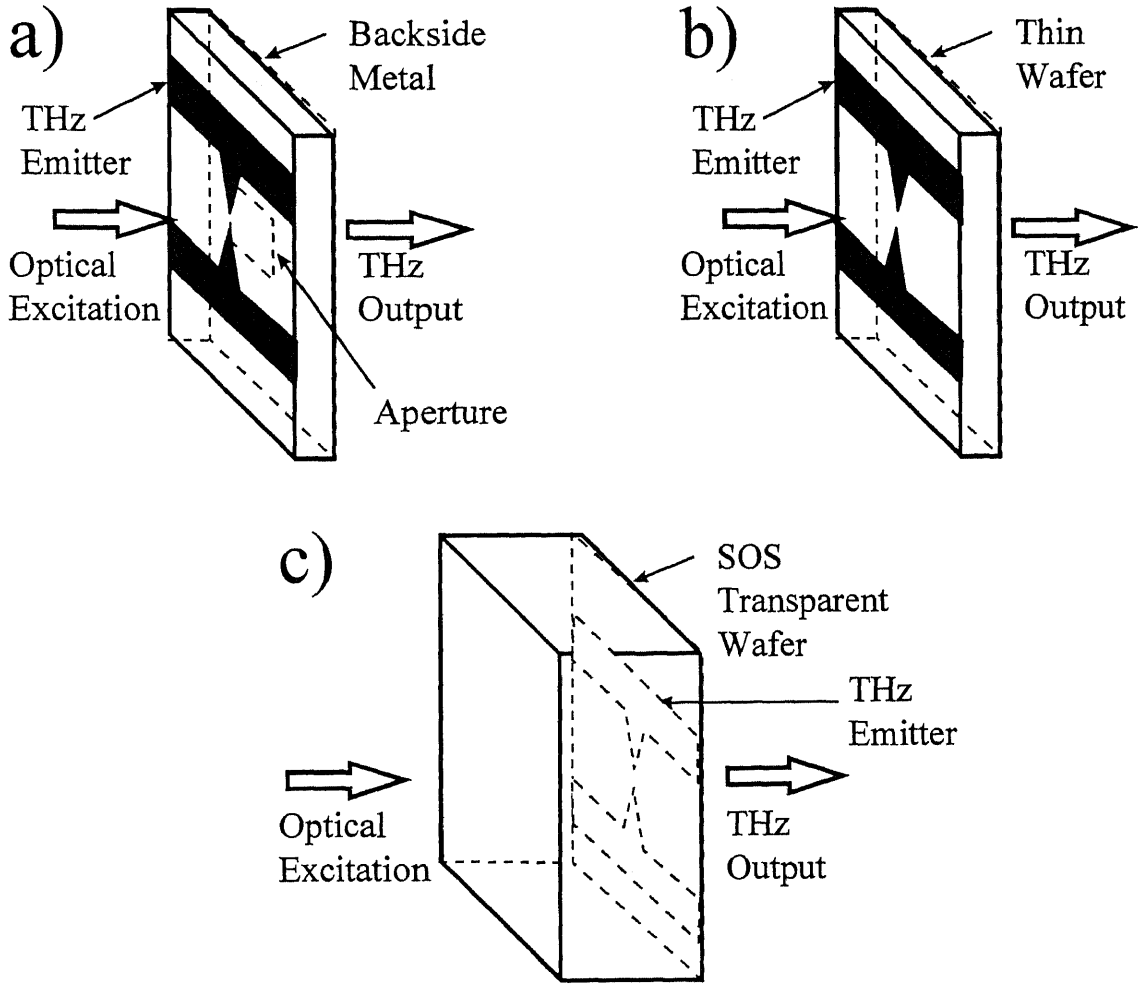

Fig.5.5 Three new designs of near-field terahertz probes: a) Integrated Backside Aperture (**IBSA**) integrates the aperture for near field imaging on the THz photoconductive antenna; b) Thin Wafer No Aperture (**TWNA**) using a 100μm thin wafer to reduce the distance between the short antenna and sample for near-field operation. c) using SOS substrate to enable Backside Optical Excitation (**BSOE**) to reduce the distance between the antenna and the sample.

The IBSA integrated near field probes (as shown in Fig5.5a) are fabricated on annealed low temperature GaAs (LTG). The metal patterns are deposited on both the

front and the back side of the wafer by conventional lithography. The front side metal patterns define the photoconducting antenna for terahertz generation. On the back side the metal patterns construct an aperture for near field imaging. A regular GaAs wafer if as thick as 500μm. To insure near field operation at all THz frequencies, the wafer is ground to 100 μm thick before the metal patterns are deposited.

It is a well known principle of microwave engineering that the most efficient way to couple far-field radiation to a device of dimension much smaller than the photon wavelength is to attach the device across the terminals of an antenna. [54,55] It is easy to apply this rule to near-field terahertz probes, considering the terahertz generation principle in photoconductive switches. The terahertz wave is originated in the semiconductor from the current surge induced by the femto second optical excitation, and then coupled into the dipole antenna. We make near field emitters simply by using a dipole antenna with a dipole length shorter than 100μm. In the TWNA structure (as shown in Fig.5.5b), in order to insure the sample can be place within the near field range for all THz frequencies, the wafer is polished down to 100 μm thick. Or alternatively in the BSOE structure (as shown in Fig.5.5c), we use a short dipole antenna fabricated on silicon on sapphire (SOS). Because the sapphire substrate is transparent to the 800 nm excitation pulses from Ti:sapphire mode locked laser, we can excite the antenna through the substrate. In that way, the dipole antenna can be placed very close to the sample without the wafer in between. Although these approaches do not provide the ultimate imaging resolution as the near-field probe with apertures, they require less sophisticated device processing and are more towards a unity efficiency.

The terahertz imaging resolution is essentially diffraction limited. As shown in Fig.5.6, an image of a razor blade taken with conventional terahertz antenna probe made on a regular 500μm thick wafer. A strong frequency dependence on the image resolution is illustrated. Only above 1.25 THz, the image of the blade becomes clear but still limited by diffraction. Image obtained at lower frequency is hampered by the diffraction pattern. A spatial resolution of about 400 μm has been achieved at frequencies above 1.25 THz.

Recently we presented significantly more powerful THz emitter with sigular electric field photoconductive antennas fabricated on LTG. [29,31] We also applied this technique in the development of near-field THz probes, for example in the TWNA structure introduced above. The emitter (60μm long dipole with a 10μm gap in the middle) is fabricated on a 100μm thin wafer, allows a minimum antenna to sample distance of less than 200μm. The very high signal to noise ratio enables the real-time acquisition of THz waveforms for each pixel. Fig.5.7 An image of a 50μm gold wire taken with TWNA near-field probe. A strong frequency dependence on the image resolution is illustrated. A spatial resolution of less than 100 μm has been achieved at a frequency of 1 THz. Because the THz-time domain spectroscopy provides not only the intensity but also the phase information, another interesting diffraction phenomena is observed. We can clearly see the pulse delay caused by diffraction. For a emitter made on 500μm thick regular wafer, Fig.5.8 shows the THz pulse delay increases with the progressive intrusion of a razor blade sample. The pulse delay is caused by diffraction: The thin wafer no aperture (TWNA) emitter is used. Terahertz transient obtained in 1-D scan with a razor blade is presented in 3-D and 2D. The dipole antenna is placed almost in contact with the sample.

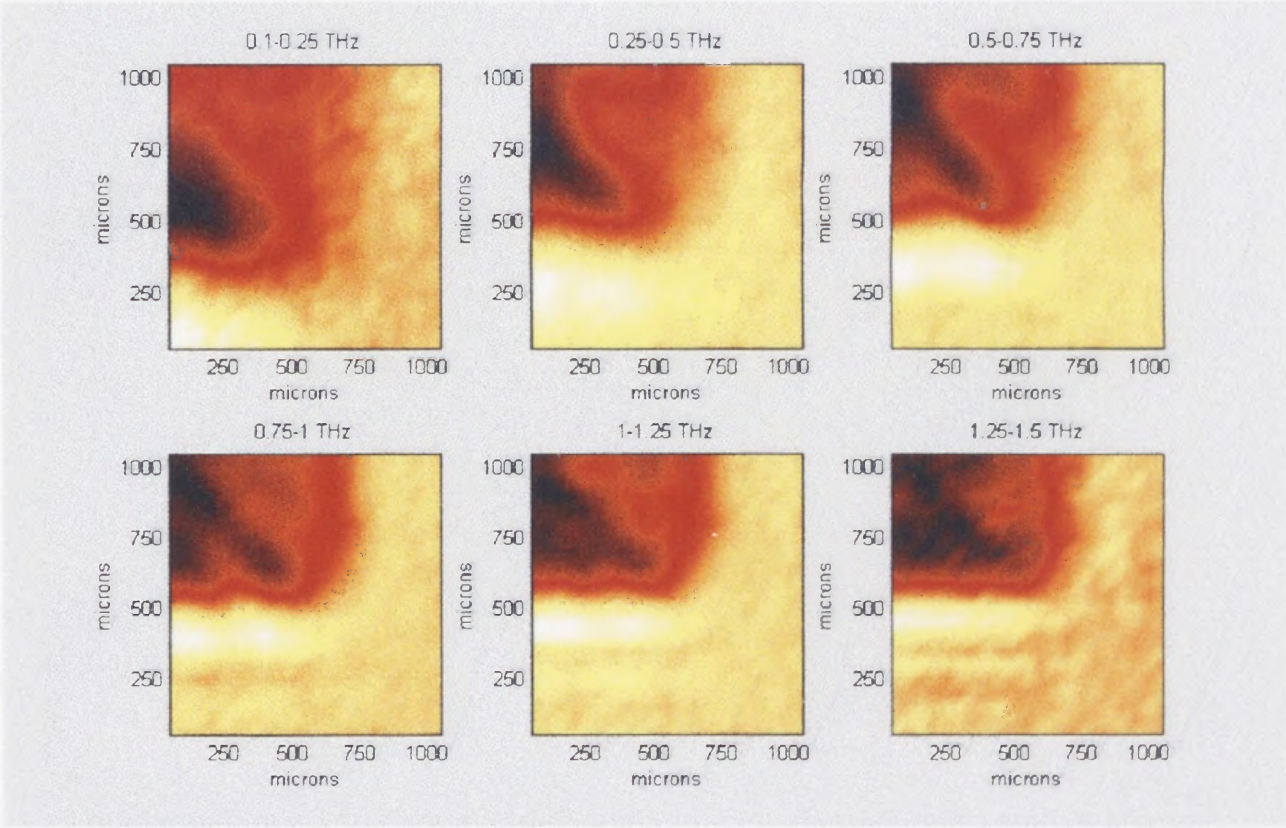

Fig.5.6 An image of a razor blade taken with conventional terahertz antenna probe made on a regular 500μm thick wafer. A strong frequency dependence on the image resolution is illustrated. Only above 1.25 THz, the image of the blade becomes clear but still limited by diffraction. Image obtained at lower frequency is hampered by the diffraction pattern. A spatial resolution of about 400 μm has been achieved at frequency above 1.25 THz.

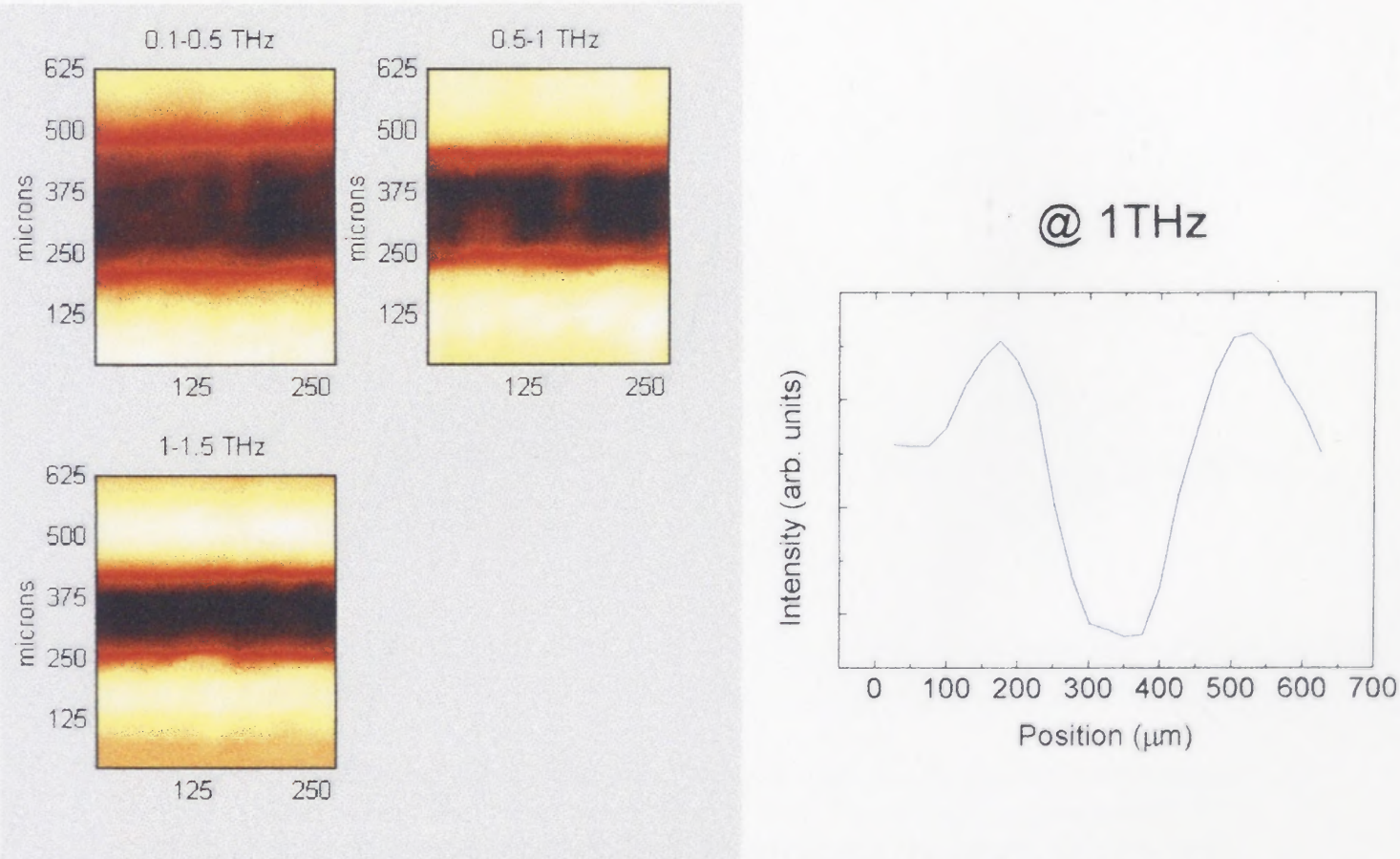

Fig.5.7 An image of a 50μm gold wire taken with TWNA near-field probe. A strong frequency dependence on the image resolution is illustrated. A spatial resolution of less than 100 μm has been achieved at frequency 1 THz.

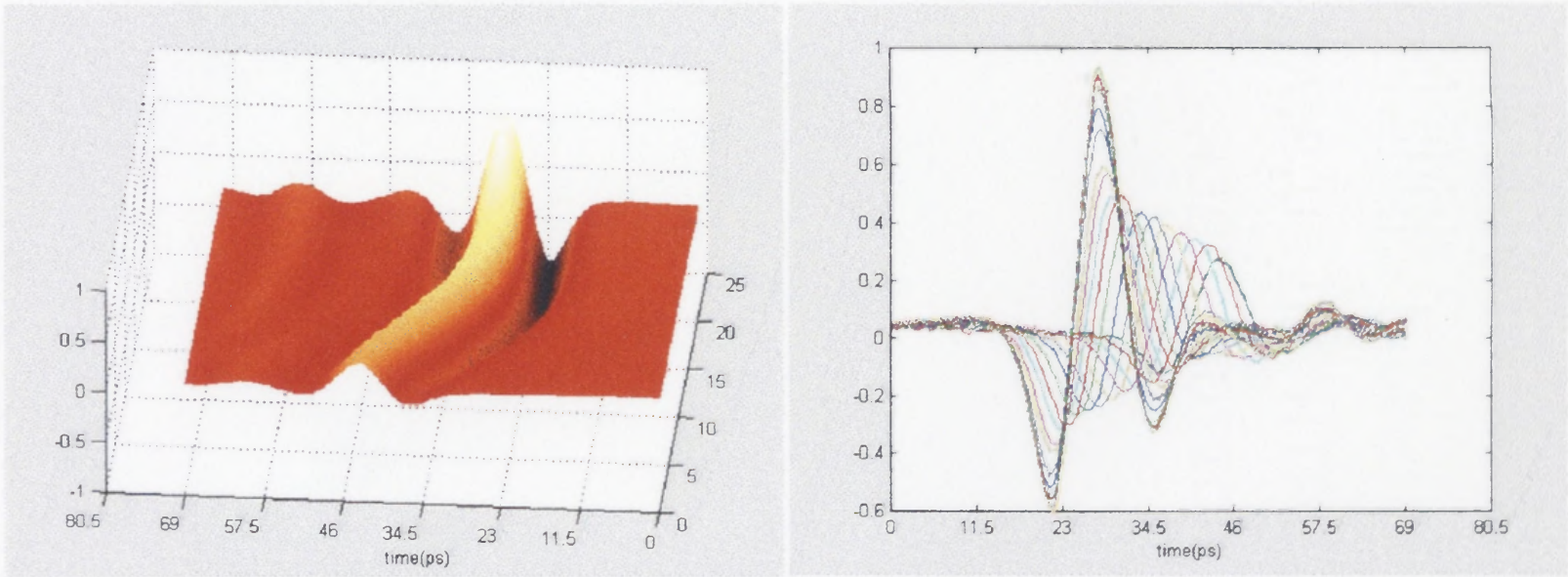

Fig.5.8 A pulse delay caused by diffraction: The thin wafer no aperture (TWNA) emitter is used. Terahertz transient obtained in 1-D scan with a razor blade is presented in 3-D and 2D. The dipole antenna is placed almost in contact with the sample. The THz pulse delay increases with the progressive intrusion of a razor blade sample. Terahertz transient obtained in 1-D scan with a razor blade is presented in 3-D and 2D.

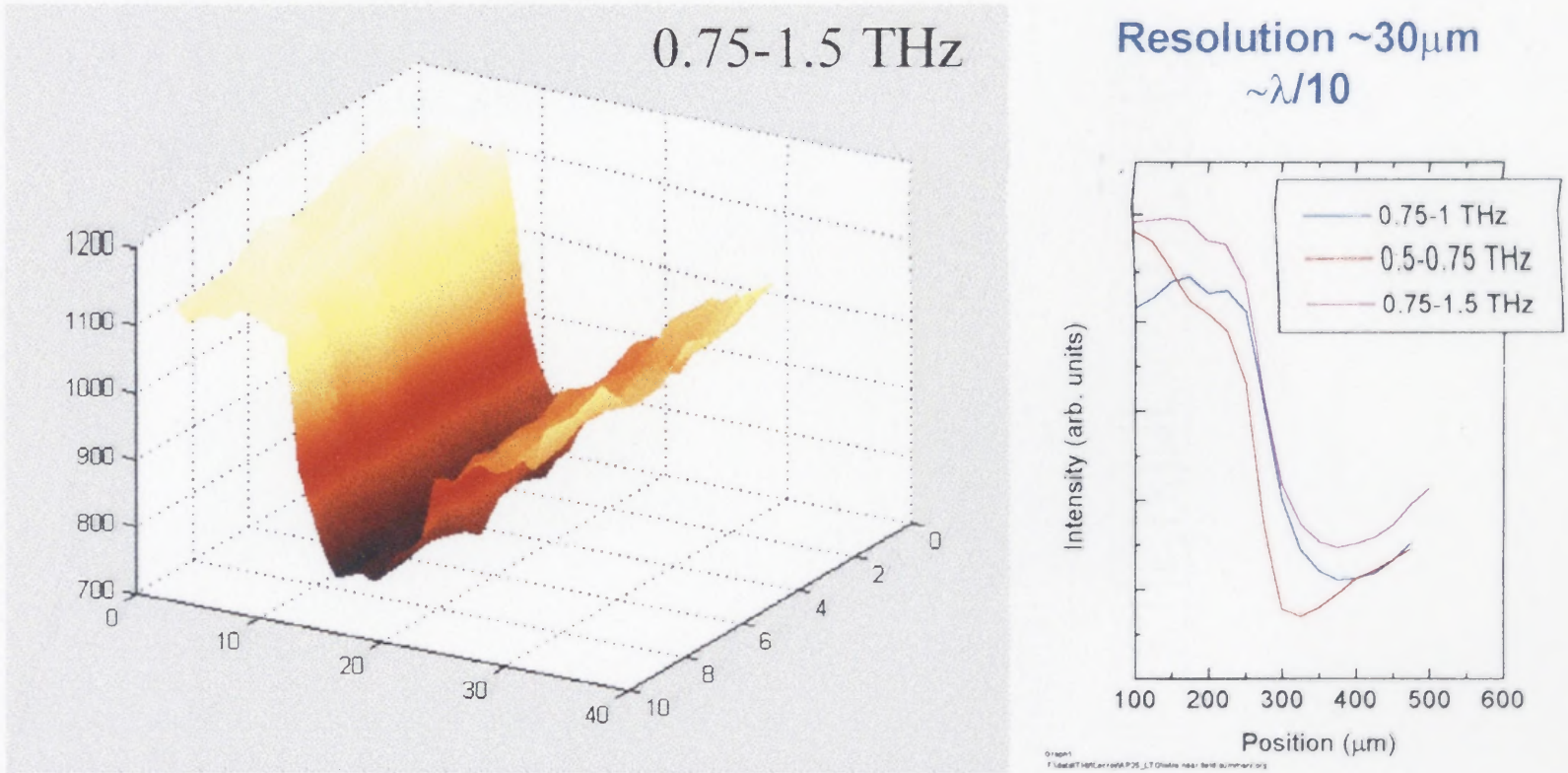

Fig.5.9 The ultimate spatial resolution is obtained with the IBSA structures using a pin hole. The probe (60μm long dipole with a 10μm gap in the middle) is fabricated on a 100μm thin wafer with a 25 μm × 25 μm aquare aperture on the back aligned with the front side emitter. An shown in Fig.5.2.5, a spatial resolution of <50 μm is achieved.

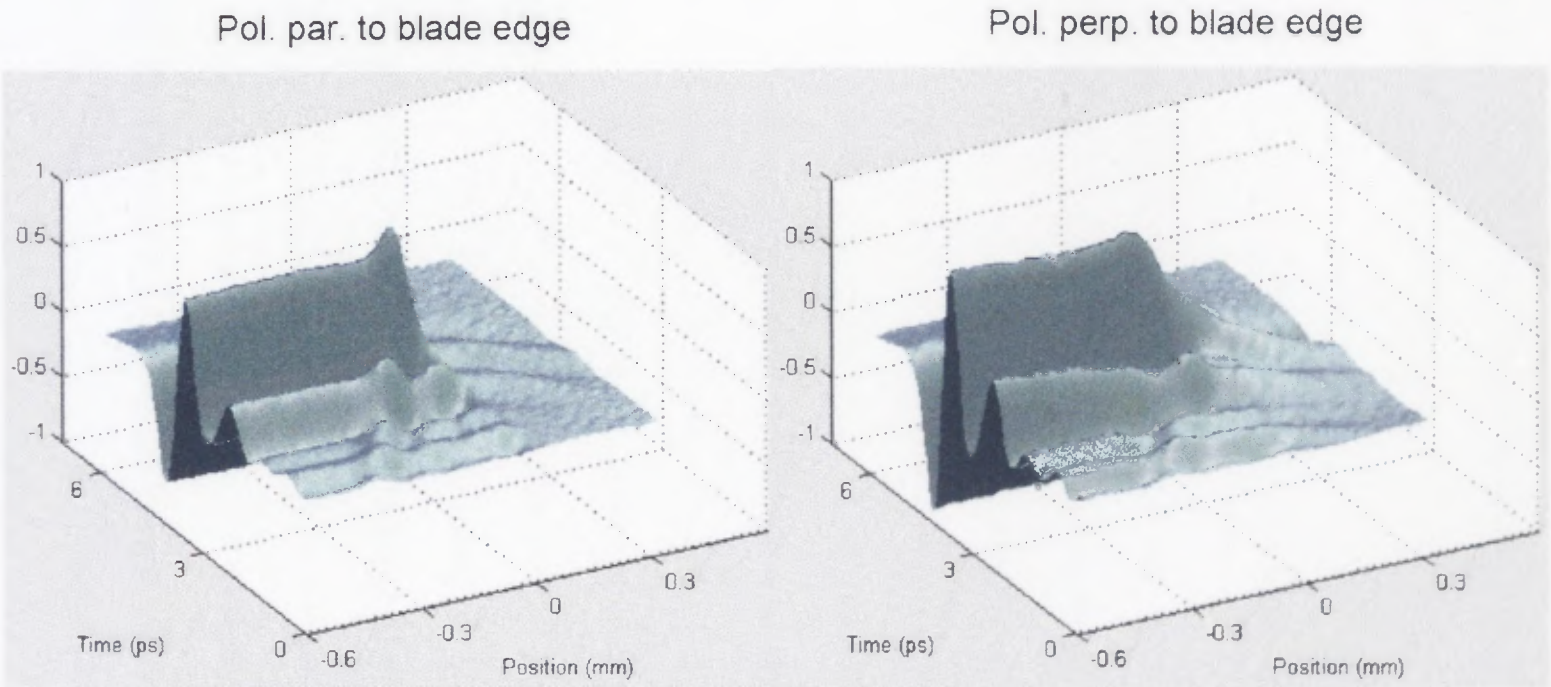

Fig.5.10 Two lines scans (vertical and horizontal respectively) with SOS emitter using backside excitation. The dipole antenna is placed almost in contact with the sample. Terahertz transient obtained in 1-D scan with a razor blade is presented in 3-D and 2D. In the 3-D plot, the x direction is scanning direction, y axis is time, and z axis is terahertz transient field intensity. The spatial resolution is better when the polarization is parallel to the edge.

In conclusion, we presented three types of integrated near-field probes for sub-wavelength spatial resolution terahertz imaging. We demonstrated a 50μm THz image resolution using a device on thin wafer with integrated backside aperture. Simpler designs also yield a spatial resolution of ~100μm.

5.3 Highest Terahertz Sensitivity in Visible Pump and Terahertz Pump Measurement

As discussed in chapter 1, the conventional application for the terahertz generation and detection is for studies of ultrafast semiconductor material in visible pump terahertz probe experiment. Pure optical measurements, typically carried out under high carrier densities (~10^{17} cm^{-3}), are often obscured by photo-induced absorption effects, hot phonon effects, band-gap renormalization and other non-linear high carrier density effects[67,68,69]. Similarly, photoconductive measurement are sensitive to device geometry, illumination uniformity and external electric fields. In contrast the FIR terahertz measurement is unambiguous. It avoids the aforementioned difficulties. Moreover, this method is a non-contact and non-destructive for short life time (~400fs resolution) and conductivity measurement. Due to fact that free carriers strongly absorb at terahertz frequencies, combined with the high signal to noise ratio of coherent terahertz detection, visible pump terahertz probe experiment reveals the carrier dynamics in LTG-GaAs material at extremely dilute photo-excitation densities (~10^{15} cm^{-3}) unambiguously. [70]

In this section we demonstrate a more sensitive visible pump and terahertz probe measurement, by using the enhanced terahertz antennas and optimizing the chopping frequency and current pre-amplifier. A modulation as low as ~10^{-6} by photo-generated

carriers is observed in our system, which inherently indicate a signal to noise ratio as high as ~10^6 of our THz system. With our terahertz system, the estimated minimal detectable photo-excitation density is as dilute as 10^{12} cm^{-3}.

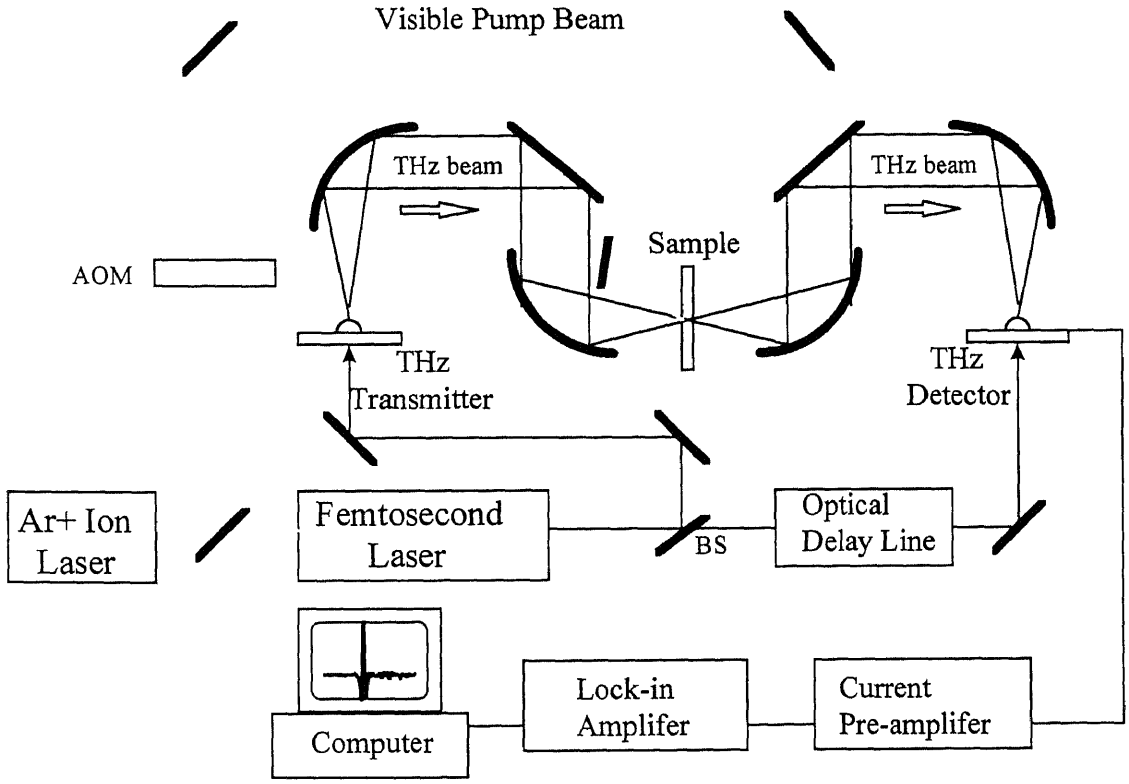

Fig.5.11 Experimental setup for visible pump and terahertz probe experiment for extremely dilute photo generated carrier density.

The experimental setup is illustrated in Fig.5.11. As presented in section 1 of this chapter, we have significantly reduced the laser noise influence by modulating the visible pump beam at high frequencies (1MHz) in the electro-optic sampling detection. Chopping at such high frequencies cannot be done in the antenna detection scheme though because the high gain transimpedance amplifiers required to amplify the photocurrent typically only have a low frequency response. The MHz bandwidth pre-amplifier we tried brings in more

noise itself than the laser noise it suppressed at this frequency. After extensive trials, we found a current pre-amp with a 100KHz bandwidth. Working with a Acousto-Optic Modulation (AOM) chopping at ~88KHz gave the lowest noise (amplifier noise plus the laser noise). When a time constant of 1 second is used for the lockin detection, a modulation as low as $\sim 10^{-6}$ by photo-generated carriers is observed in our system, which inherently indicate a signal to noise ratio as high as $\sim 10^{6}$ of our THz system.

5.4 Compact Terahertz System Using All Solid State Diode Pumped Cr:LiSaF Laser

Typical terahertz system requires a mode locked Ti:sapphire in a box of about 1.5 meter×0.5meter ×0.3 meter. This sub-picosecond laser itself has to be pumped by a visible beam of at least 5W. It is typically delivered by a Ar+ ion laser about 2 meter×0.2meter ×0.2 meter. Besides the laser, the optical steering and terahertz collecting / steering components, there are electric instruments such as lockin amplifier, current pre-amplifier, scanning delay lines and two dimensional scanning stage (for focal plane imaging). So although the photoconductive antenna itself is a micron size device, the server units are very clumsy in size.

For many applications, the current system is too complicated to be handled by a novice. In order to commercialize the terahertz time domain spectroscopy and imaging systems, the size of the system has to be reduced and simplified to make it more user friendly. Ideally, as discussed in chapter 7 as future research directions, a portable terahertz system has to be excited by a mode locked fiber laser, and the photoconductive switches have to be integrated with fiber optics. Then the integrated optical parts should be assembled into a box together with the lockin amplifier and a digital oscilloscope (or a

DSP card linked to a computer). Although every individual technology mentioned above is somewhat available now, there is still an unsolved issue in the way. Despite the emergence of mode-locked fiber lasers, there is no semiconductor material that provides subpicosecond response at the 1.3 μm (0.95eV) or 1.55 μm (0.77eV) wave lengths. The typical materials used for terahertz applications are GaAs (to 840nm, gap~1.42eV) and Si (to 1.07μm, gap~1.12eV), for which the processing technologies are somewhat mature in the microelectronics industry.

The next best thing is to replace the Ti:sapphire mode-locked laser with a diode pumped femtosecond laser. As an experiment, we use a Cr:LiSaF diode pumped laser build by Sergio Tsuda at Bell-Labs, Lucent Technologies. The laser is pumped with a 1.5W 674nm GaAlAs Diode laser. The total size of the laser (including the diode laser) is comparable to the Ti:sapphire laser. Therefore the size of the system is reduced by eliminating the need for a gas (Ar+ ion) laser. The laser power output is ~40mW when mode locked. After going though all the laser monitoring instruments and beam steering optics, 2~3mW is delivered to each antenna (emitter and detector). This power is much lower than what we normally used (20-30mW) for the peak performance. On the other hand, the laser stability is poor comparing to the commercial Ti:sapphire laser. We still manage to get a signal to noise ration above a 1000 with a 300ms time constant for the lockin detection.

A THz photo-conductive antenna excitation efficiency comparison of GaAlAs diode pumped Cr:LiSaF laser vs. argon ion laser pumped Ti:sapphire laser at comparable power is shown in Table 5.2.

Table 5.2. THz Photo-conductive Antenna Excitation Efficiency comparison of GaAlAs Diode pumped LiSaF Laser vs. Argon Ion Laser Pumped Ti-Sapphire Laser at Comparable Power

	Signal	Noise	SNR	time const.
Cr:LiSaF Laser[a]	0.45nA	0.35E-3nA	1285	300ms
Ti-Sapphire Laser[b]	2.3nA	0.45E-3nA	5110	300ms

(a) Using LiSaF laser in regular 2 paraboloids THz setup, singular electric field emitter (D45-G5 TT0) with Si lens, under 60V bias (0.092mA) and 3.25mW optical excitation, singular electric field detector D60-G5 TT0 detector with Si lens(1mm) gated by 2.1mW optical power. 1.5KHz mechanic chopping.

(b) Using Ti:sapphire laser in regular 2 paraboloids THz setup, singular electric field emitter (D45-G5 TT0) with Si lens, under 60V bias (0.062mA) and 3.4mW optical excitation, singular electric field detector D60-G5 TT0 detector with Si lens(1mm) gated by 2.1mW optical power. 1.5KHz mechanic chopping.

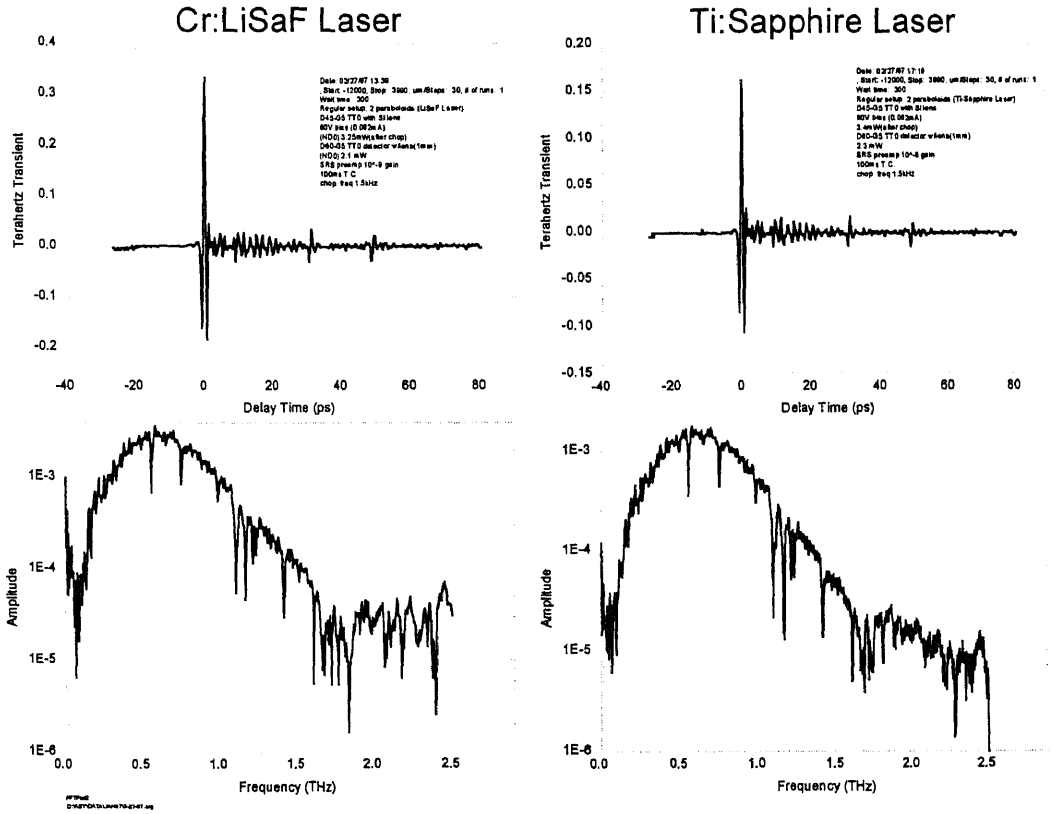

Fig.5.12 Terahertz transient waveforms and spectrums obtained from the same pair of photoconductive antennas excited by argon ion laser pumped Ti:sapphire mode-locked laser and diode pump Cr:LiSaF laser under comparable laser power. The time constant is 100ms for both waveforms

The diode pumped system performance becomes close to the gas laser pumped system at comparable power levels, as shown in Fig.5.12. Because of the high efficiency terahertz emitters and detectors, the system carries an adequate signal to noise ratio for some applications. The cost for this type of system is estimated at less than half of the Ar+ pumped system, while the size is reduce by half at the same time.

5.5 Summary

In conclusion, we demonstrated how the newly enhanced antenna can be integrated into various aspects of terahertz technology. We presented a new approach for THz free space electro-optic sampling (FSEOS) system used to reach shot noise limited detection. And we demonstrate the feasibility of *a THz focal plane imaging system using real time delay scanning in FSEOS* with our new THz source that, for the first time, requires only 20mW of laser power. The previous systems using completely different approach requires more laser power and strictly low noise laser. Next, we presented new *terahertz imaging probes with 30μm sub-wavelength spatial resolution.* The probe integrates the new terahertz antenna in the front side of the 100μm thin wafer and aperture for near field imaging on the back side. And we showed the improvement on performance of conventional THz spectroscopy systems by combining the highly efficient THz generators and detectors with high speed modulation (90kHz) lockin detection: A *modulation depth of as low as* $\sim 10^{-6}$, or as high as $\sim 10^{6}$ in term of signal to noise ratio, is achieved in our THz system with 1s time constant for the lock-in detection. And last we demonstrated a *compact all solid-state terahertz system*, operating with a diode pumped Cr:LiSaF laser. The high efficiency

of the new terahertz antenna is essential for the operation of the system, because of the relatively low excitation power this laser can provide.

CHAPTER 6

APPLICATION DEMONSTRATIONS

In this chapter, we demonstrate some applications with the new improved terahertz time domain spectroscopy and imaging systems. However, there is no intention what so ever for the author to cover too many application aspects in this dissertation. The theme for this work is to push the terahertz generation/detection, and imaging technologies to a new height. A general review of the applications are included in chapter 1 as introduction. We will only demonstrate some applications in this chapter, either as a direct by product of our research, or as evidence to the performance of the systems equipped with our new devices.

6.1 Volatile Organic Chemical Sensors

The feasibility of a microsensor has been demonstrated to monitor the composition and concentration of volatile organics which are characteristically emitted during thermoplastic processing. The volatile organics are to be monitored using a pulsed Terahertz spectroscopy technique which simultaneously identifies organic compounds through their characteristic absorptions in the far infrared regime. Such a technology would provide a compact, portable, and real time diagnostic tool of atmospheric volatile organics. Moreover, by monitoring the concentration of volatiles along the length of the thermoplastics reaction chamber, one could potentially monitor online the evolution of volatile emissions and develop active feedback to the processing parameters to optimize the thermoplastic processing.

Plastics processing operations produce air emissions consisting of both volatiles and particles at levels as high as 5% of the actual tonnage of resins processed annually in the United States. Volitiles are usually emitted during extrusion and injection from heated cylinders and molds and may consist residual monomers, moisture, solvents, decomposition products of thermoplastic resins and their additives. The identification of volatiles and the development of analytical techniques for measuring their concentration on the factory floor are of paramount importance in establishing or revising threshold limit values which would minimize overexposure and lead to corrective action. Moreover, by monitoring the concentration of volatiles along the length of the thermoplastics reaction chamber, one could potentially monitor online the evolution of the volatile emissions and develop active feedback to the processing parameters to optimize the thermoplastic processing. These can not be achieve with the Fourier Transform Infrared Interferometry (FTIR), evanescent wave spectroscopy or Mach-Zender Interferometry. The terahertz time domain spectroscopy has a clear advantage over the later two techniques because of its high signal sensitivity owing to its coherent nature, and over the FTIR for its relatively compact size. As we showed in chapter 5, the size of the terahertz system can be further reduced with the use of diode pumped mode-locked lasers.

The sensor under development offers the capability of in-situ pollution monitoring, online sensing and control of plastic extruders including the evolution of solvents which are added during the extrusion process.

The operation of this device will be based on the far-infrared absorption of organic molecules which exhibit characteristic signatures in that frequency range. It should be particularly noted here that polar organic compounds strongly absorb in the far infrared

and, therefore, are readily identifiable. Table.6.1 [71] listed several volatile organic chemicals emitted during thermoplastics processing and their FIR peak absorption.

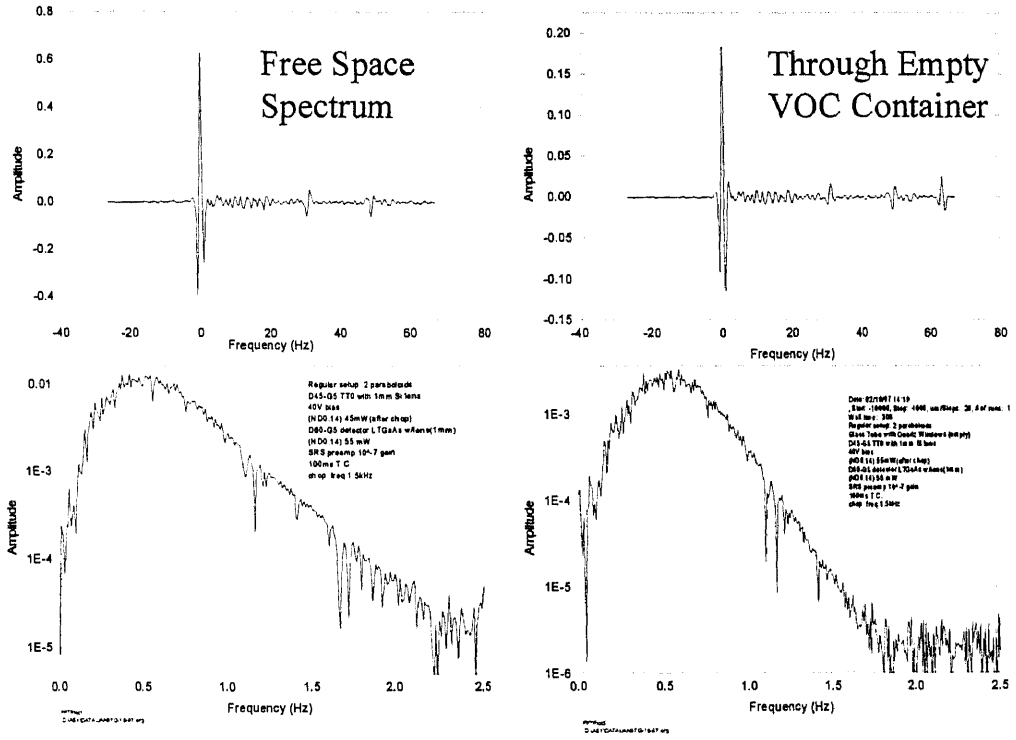

Fig.6.1 Terahertz waveform and spectrum through free space and empty VOC cell with quartz widows. The bandwidth is reduced because of the high frequency cut of quart.

We demonstrated this strong absorption of saturated acetone gas in a 54mm and a 139mm long VOC cell with quartz windows in Fig.6.2. As shown in Fig.6.1, the quartz window cuts off the high frequency components. The future designs sapphire windows are desired. Fig.6.3 normalize the absorption spectrum by the background. From the Fig.6.3, we estimated that a minimal acetone gas layer of ~5mm thick is detectable by our terahertz system at room temperature and pressure. Further research is proposed to determine the sensitivity limit, and compare with other competing techniques.

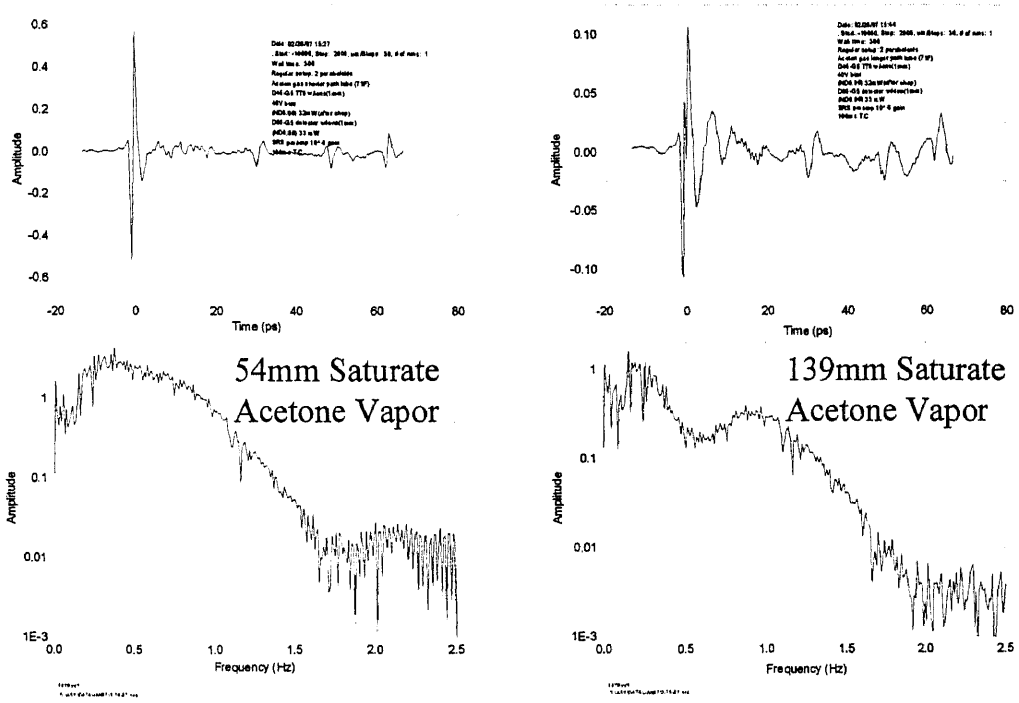

Fig.6.2 Terahertz waveform and spectrum through a 54mm and a 139mm VOC cell filled with saturated acetone gas at room temperature.

Table.6.1 VOC emitted during thermoplastics processing and their FIR peak absorption

Chemical	FIR peak absorption (cm-1)	Plastic
acetone	20, 110, 130	PE, PP
ethyl chloride	175-300	PVC
acetic acid	176	PE, PP
butyric acid	78, 72	PE
benzene	80 (broad)	PVC, PS

Source: S. H. Patel and M. Xanthos, "Volatile emission during thermoplastics processing", Advances in Polymer tech. 14, 67 (1995)

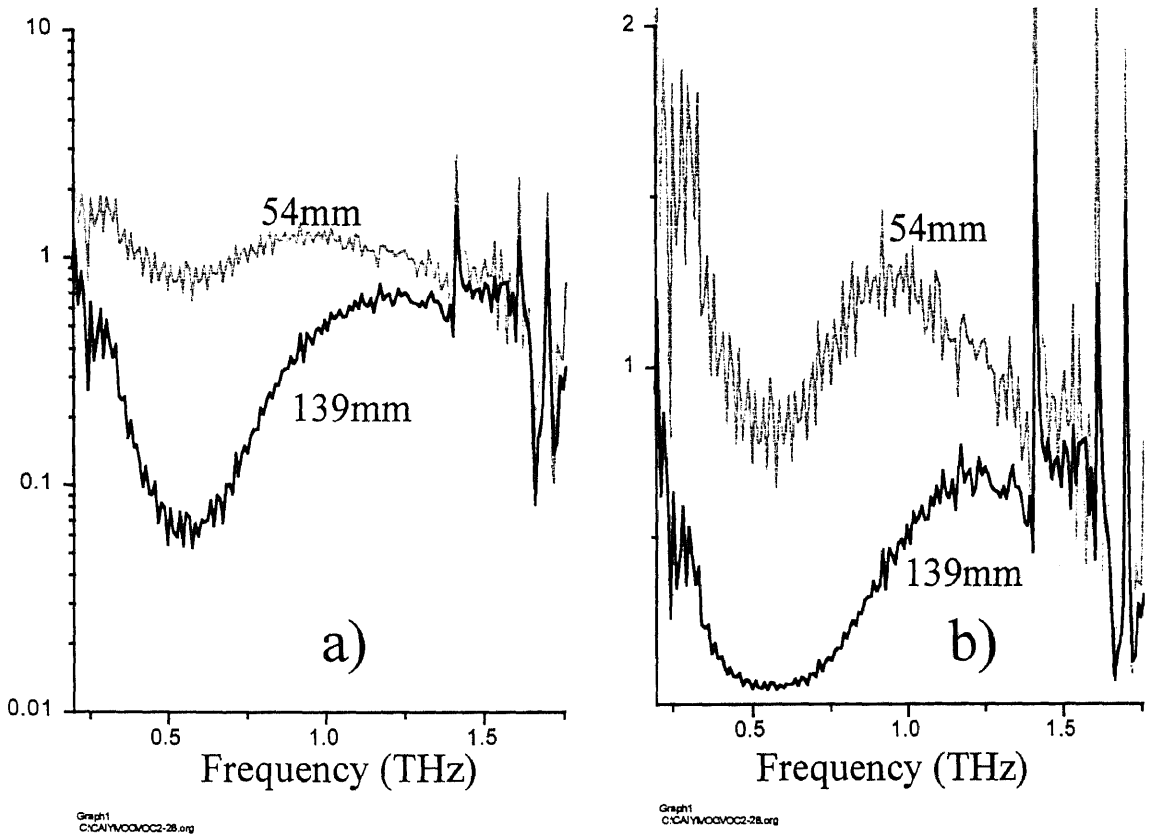

Fig.6.3 Terahertz absorption spectrum through a 54mm and a 139mm VOC cell filled with saturated acetone gas at room temperature, normalized by the background spectrum. a) is in logarithmic scale and b) in linear scale.

The proposed instrument is compact, portable, and suitable for real time monitoring of numerous VOCs. The sensor is projected to have a minimum detection limit in the 0.1 to 0.01% (1000-100ppm) range and be integrated with fiber-optic technolgy. The fabrication of the device is based on low-temperature grown GaAs technology which allows for high degree of electronic and photonic integration. In addition to offering important advantage of miniaturization, the technology offers high throughput and low cost per device. The prototype VOC sensor is being setup in laboratory at NJIT.

6.2 Photo Induced Conductivity Measurement

In chapter 5, we demonstrated a more sensitive visible pump and terahertz probe measurement, by using the enhanced terahertz antennas and optimizing the chopping frequency and current pre-amplifier. A modulation as low as $\sim 10^{-6}$ by photo-generated carriers is observed in our system, which inherently indicate a signal to noise ratio as high as $\sim 10^{6}$ of our THz system.

Due to fact that free carriers strongly absorb at terahertz frequencies, combined with the high signal to noise ratio of coherent terahertz detection, visible pump terahertz probe experiment has been reported revealing the carrier dynamics in LTG-GaAs material at extremely dilute photo-excitation densities ($\sim 10^{15}$ cm^{-3}) unambiguously. [70]

We applied this system into investigation of semi-insulating GaAs. We use 185mW 500nm (2.4eV) visible CW laser pumping a 5 mm^2 area. The photo-excited carrier density in the semi-insulating SI-GaAs is estimated to be $\sim 3\times 10^{13}$ cm^{-3} (assuming 1ns lifetime and 10^{-4}cm absorption depth). The peak THz signal detected when modulating the visible pump beam is 60μV (peak to peak). The minimal detectable THz signal when modulating the visible pump beam is 3μV (peak to peak). So minimal detectable photo induced carrier density should be 1.5×10^{12} cm^{-3}. Therefore our terahertz system is estimated to detect a minimal photo-excitation density is as dilute as 10^{12} cm^{-3}. The terahertz signal under this weak modulation depth is shown in Fig.6.4. The signal is obtained when the visible beam pumping the SI-GaAs is chopped for lockin detection, therefore the measured signal strength is the indication of the photo-generated carrier density. Due to fact that free carriers strongly absorb at terahertz frequencies, combined with the high signal to noise ratio of coherent terahertz detection, visible pump terahertz probe experiment has been

reported revealing the carrier dynamics in LTG-GaAs material at extremely dilute photo-excitation densities (~10^{15} cm^{-3}) unambiguously. [18 in chapter 5]

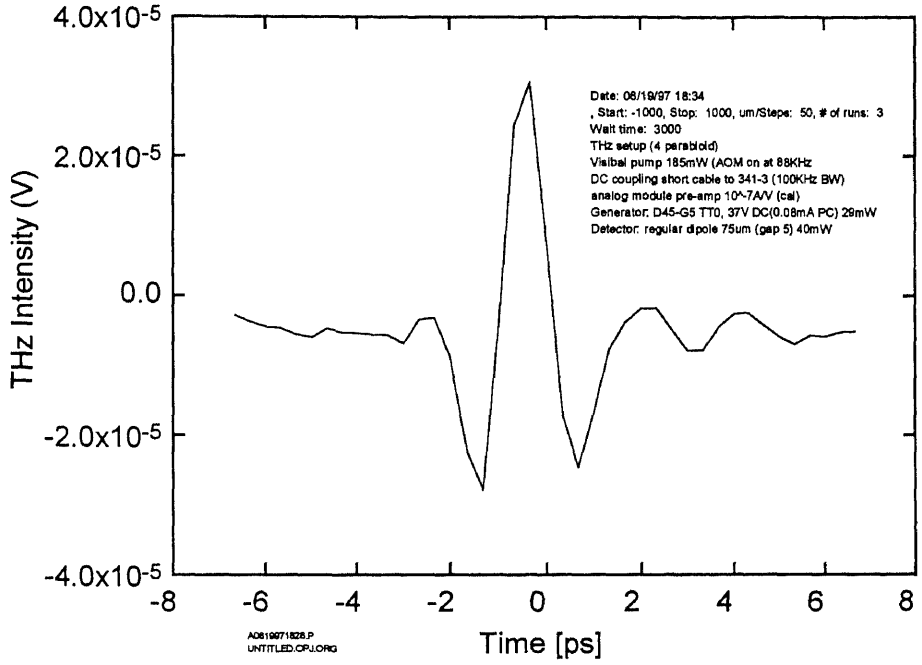

Fig.6.4 Signal obtained while the visible beam pumping the SI-GaAs is chopped for lockin detection, therefore the measured signal strength is the indication of the photo-generated carrier density. The photo-excited carrier density in the semi-insulating SI-GaAs is estimated to be ~3×10^{13} cm^{-3}.

We also measured the silicon nanocluster-thin-films. The nanoclusters laser ablated on quartz substrate by Vijayalakshmi and Grebel [72]. The signal to noise ratio is very low. But it is still surprise us that it can be detected, considering it is a thin film (low absorption) and granular sample (low mobility). The sample is reported to have a very high nonlinearity ($\chi^{(3)}$ value as high as 1.4×10^{-4} esu at λ = 532nm). The terahertz photoconductivity measurement is sensitive to the carriers' mobility. Our attempt on

probing the photo-generated carrier dynamics of samples with extremely low mobility, such as organic crystals and amorphous silicon, were not successful.

6.3 Summary

In this chapter, we first demonstrated that the new improved terahertz system can be used as very sensitive chemical sensors. And we presented the results of a more sensitive visible pump and terahertz probe measurement that detects a minimal photo-excitation density is as dilute as 10^{12} cm^{-3}. We only demonstrated these two applications in this chapter, either as a direct by product of our research, or as evidence to the performance of the systems equipped with our new devices. There are other technological advances presented in this thesis, such as low power real time ultra-wide-band FSEOS imaging and sub-wavelength spatial resolution near-field imaging, that will inspire more new applications.

CHAPTER 7

CONCLUSION REMARKS

7.1 Summary of Research Results

This dissertation presents a systematic study of a new family of more efficient THz antennas, range from the engineering simulation, device fabrication, system characterization and its applications. We, for the first time, design the THz dipole antennas with a relatively sophisticated shapes to optimize the fringing electric field in the regime where the THz pulse is generated. We presented the results of the characterization of these devices, which demonstrate that this is the most efficient THz emitters, to our knowledge, with a record high THz average power of 2-3μW with mW laser excitation. The previous state-of-the-art THz radiation power under similar condition reported are 38nW [39] and 10nW [25].

With the singular electric field terahertz emitters that reach the record high μW level power level, we are enabled to impact the terahertz spectroscopy imaging technology with even higher band width, sensitivity, spatial resolution, and compactness. We present several demonstrations on these improvements, where the singular electric field antenna played important rolls. The advances include:

(1) The significant improvement on performance of THz spectroscopy systems by combining the highly efficient THz generators and detectors with high speed modulation lockin detection: A modulation depth as low as ~10^{-6}, or as high as ~10^{6} in term of signal to noise ratio, is achieved with our THz system with 1s time constant for the lock-in

detection. The improved terahertz system is estimated to detect a minimal photo-excitation density as dilute as 10^{12} cm^{-3}.

It is important because that pure optical measurements, typically carried out under high carrier densities (~10^{17} cm^{-3}), are often obscured by photo-induced absorption effects, hot phonon effects, band-gap renormalization and other non-linear high carrier density effects[15,16,17]. Similarly, photoconductive measurement are sensitive to device geometry, illumination uniformity and external electric fields. In contrast the FIR terahertz measurement is unambiguous. It avoids the aforementioned difficulties. Moreover, this method is non-contact and non-destructive for short life time (~400fs resolution) and conductivity measurement. Due to fact that free carriers strongly absorb at terahertz frequencies, combined with the high signal to noise ratio of coherent terahertz detection, visible pump terahertz probe experiment reveals the carrier dynamics at extremely dilute photo-excitation densities unambiguously.

(2) With our new approach for THz free space electro-optic sampling (FSEOS) system to reach shot noise limited detection, we demonstrate the feasibility of a THz focal plane imaging system using real time delay scanning in ultra wide band FSEOS with our new THz source that, for the first time, requires only 20mW of laser power. The previous art system using completely different approach requires 1.5W of laser power and strictly low noise laser. This technique is going to enable terahertz T-ray imaging with higher band width requirement, such as chemical mapping related applications.

(3) We present new integrated terahertz imaging probes with the highest spatial resolution. The probe integrates the terahertz source in the front side of the wafer and aperture for near field imaging on the back side. The new high power emitter is used to

compensate the power loss by sub-wavelength sized aperture. We demonstrated a ~30μm THz image resolution using a device on thin wafer with integrated backside aperture. This advancement will solve the diffraction limited resolution problems in some applications, such as the T-ray studies of biological tissue samples.

(4) We demonstrated a compact all solid-state terahertz system, operating with a diode pumped Cr:LiSaF laser. The high efficiency of the new terahertz antenna is essential for the operation of the system, because of the relatively low excitation power this laser can provide. The diode pumped system performance becomes close to the gas laser pumped system at the comparable power level, as shown in Fig.5.4.1. Because of the high efficiency terahertz emitters and detectors, the system carries a adequate signal to noise ratio for some applications. The cost of this type of system is estimated less than half of the Ar+ pumped system, while the size is reduce by half at the same time. This is an important step for some applications, such as portable chemical sensors that we have discussed in chapter 4.

In the last chapter, we demonstrated a few applications empowered by this high sensitivity, including chemical sensing, photo induced conductivity measurement of Si nano-cluster-thin-film, semi-insulating GaAs. There are more technological advances presented in this dissertation, whose applications are not discussed, such real time THz imaging with wide band electro-optic crystal THz sensors, and sub-wavelength spatial resolution terahertz imaging. As enable techniques, they have a broad band applications throughout the terahertz technologies.

7.2 Direction for Future Research

The trends in terahertz research were (1) more terahertz power; (2) less laser power; (3) higher sensitivity; (4) higher bandwidth; (5) higher spatial resolution; (6) real time; and (7) compact. We believe these will still be the directions in the future.

Like any other technologies, there is no remedy for all problems. We started the dissertation with more terahertz power generated from the singular electric field antennas. The gap is 5 microns in size made possible by IC lithography, and DC biased at (<40V). As pointed out earlier, our generators give the highest terahertz power (3 μW) with very low laser power (mW) [29], with the highest sensitivity. It is another direction of active research that use high voltage pulse (45,000V) biasing (another way to create higher electric field within the gap) and about a watt laser power to excite device with a 3 cm gap [35]. This configuration delivers 100 times more terahertz power, while everything in the server systems (bias, laser power, device size) is thousands times more comparing to our devices. The reported results are detected with incoherent method. It looks noisy and has a little lower bandwidth. Further research is needed to determine the sensitivity level of this system. Because of the use of high voltage pulser, one would expect more noise. Moreover with the needs for laser amplifier high voltage pulser, it makes the already sophisticated terahertz system even more cumbersome. Another interesting research direction will be to implement the high voltage pulser together with our singular electric field technique in a small gap and low laser power system.

We also addressed real time scanning with higher bandwidth using free space electro-optic sampling (FSEOS) detection [40] and our singular electric field emitter. Again there is another approach to reach even higher band width (~37 THz) [65] with

unbiased terahertz emitters without dipole structures. The difficulty in this direction is the lower terahertz power (i.e. 0.3μW) but more laser power (i.e. 1.5W).

Higher spatial resolution is achieved with our integrated near-field terahertz probes evolved with our singular electric field antennas. The highest spatial resolution (~30 μm at about 1THz) [75]. There is still many aspects that requires further improvements.

It has aroused tremendous amount of interests after the terahertz imaging was first demonstrated [26] in 1996. There is a trade off between real time and sensitivity. We demonstrated lower laser power high bandwidth FSEOS real time imaging systems as an example [74]. Our improved sensitivity can be "translated" into faster imaging speed. The same principle also applies terahertz imaging systems using antenna detection. The terahertz imaging discussed in this dissertation are all based on one pixel focal plane imaging systems, where the sample under investigation is mechanically scanned in two dimensions. Another approach in this research is to use large unfocused terahertz beam spot to illuminate the whole imaging area (as we use flush light for CCD imaging) and scanning the detector two dimensionally. This method however is limited by the already too weak terahertz source. Further research is needed to investigate the possibility of using focal plane array.

Another important research direction is to integrate terahertz antennas with fiber optics, as shown in Fig.7.1. This will minimize the effect in optical alignment. And with the use of a mode-locked fiber laser (also an active research area), the terahertz system can be integrated into a very small portable unit. As pointed out in chapter 6, this approach is not immediately feasible, because the lack of semiconductor materials with

sub-picosecond response at the fiber laser wavelength. Ultrafast material research is expected to link them together in the future.

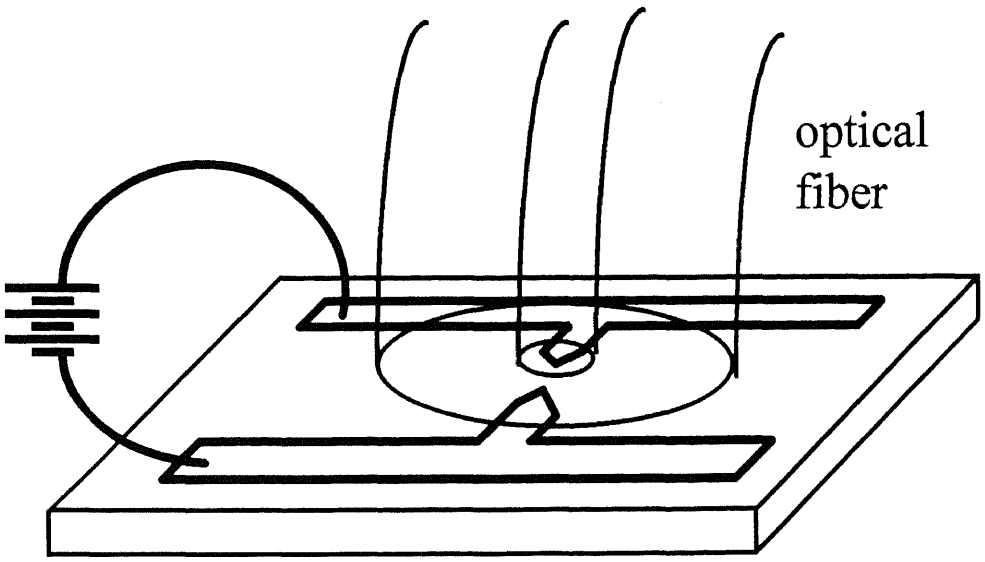

Fig.7.1 Conceptual integration of terahertz antennas with fiber optics.

REFERENCE

[1] R. L. Fork and C. V. G. Shank, *Applied Physics Letters*, vol. 38, pp. 671, 1981

[2] D. E. Spence, P. N. Kean, and W. Sibbett, "60 fsec pulse generation from a self-modelocked Ti:Sapphire laser", *Optics Letters*, vol. 16, pp. 42-44, 1991

[3] W. H. Knox, "The revolution in femtosecond near-infrared pulse generation", *Optics and Photonics News*, pp. 10-14, 1992

[4] D. Kopf, K. J. Weinarten, L. R. Brovelli, M. Kamp, and U. Keller, "Diode-pumped 100-fs passively mode-locked Cr:LiSaF laser with an antiresonant Fabry-Perot saturable absorber", *Optics Letters*, vol. 19, pp. 2143-5, 1994

[5] N. H. Rizvi, P. M. W. French, and J. R. Taylor, "50-fs pulse generation from a self-starting cw passively mode-locked Cr:LiSrAlF$_6$ laser", *Optics Letters*, vol. 17, pp. 877-879, 1992

[6] S. Tsuda, W. H. Knox, E.A. De Souza, W. Y. Jan, and J. E. Cunningham, "Low-loss intracavity AlAs/AlGaAs saturable Bragg reflector for femtosecond mode locking in solid-state lasers", *Optics Letters*, vol. 20, pp. 1407-1409, 1995

[7] D. H. Auston, *Picosecond Photoconductors: Physical Properties and Applications, Picosecond Optoelectronic Devices*, C. H. Lee, Ed. Orlando, Florida: Academic Press, pp.73-117, 1984

[8] D. H. Auston, *IEEE Journ. Quantum Electr.*, volQE-19, pp. 639-648, 1983

[9] G. W. Chantry, H. M. Evans, J. W. Fleming, and H. A. Gebbie, "TPX, a new material for optical components in the far infrared spectral region", *Infrared Physics*, vol. 9, pp31-33, 1969

[10] J. M. Chwalek, J. F. Whitaker, and G. A. Mourou, " Submillimeter wave response of superconducting Yba/sub 2/cu/sub 3/o/sub 7-x/ using coherent time-domain spectroscopy", *Electronics Letters*, vol. 27, pp. 447-448, 1991

[11] D. H. Auston, *Ultrafast Optoelectronics, in Ultrafast Laser Pulses and Applications, vol. 60, Topics in Applied Physics*, W. Kaiser, Ed. Heidelberg: Springer-Verlag, pp.183-233, 1988

[12] D. H. Auston, *Applied Physics Letters*, vol. 26, pp.101-103, 1975

[13] G. Mourou, C. V. Stancampiano, A. Antonetti, and A. Orszag, "Picosecond microwave pulses generated with a subpicosecond laser-driven semiconductor switch", *Applied Physics Letters*, vol. 39, pp.295-296, 1981

[14] R. Heidemann, T. Pfeiffer, and D. Jager, "Optoelectronically pulsed slot-line antennas", *Electronics Letters*, vol. 19, pp. 316-317, 1983

[15] A. P. DeFonzo, M. Jarwala, and C. Lutz, "Transient response of planar integrated optoelectronic antennas", *Applied Physics Letters*, vol. 50, pp 1155-1157, 1987

[16] Y. Pastol, G. Arjavalingam, J. M. Halbout, and G. V. Kopcsay, "Characterization of an optoelectronically pulsed broadband microwave antenna", *Electronics Letters*, vol. 24, pp. 1318, 1988

[17] D. H. Auston, "Picosecond photoconducting Hertian dipoles", *Applied Physics Letters*, vol. 45, pp.284-286, 1984

[18] P. R. Smith, D. D. Auston, and M.C. Nuss, "Subpicosecond photoconducting dipole antennas", *IEEE Journal of Quantum Electronics*, vol. 24, pp. 255-260, 1988

[19] C. Fattinger and D. Grischkosky, "Point source terahertz optics", *Applied Physics Letters*, vol.53, pp. 1480-1482, 1988

[20] C. Fattinger and D. Grischkosky, "Terahertz beams", *Applied Physics Letters*, vol.54, pp. 490-492, 1989

[21] D. H. Auston, K. P. Cheung, J. A. Valdmanis, and D. A. Kleinman, "Cherenkov radiation from femtosecond optical pulses in electro-optic media", *Physical Review Letters*, vol. 53, pp. 1555-1558, 1984

[22] M. C. Nuss, D. H. Auston, and F. Capasso, "Direct subpicosecond measurement of carrier mobility of photoexcited electrons in gallium arsenide", *Physical Review Letters*, vol. 58, pp. 2355-2358, 1987

[23] D. H. Auston and M. C. Nuss, "Electro-optical generation and detection of femtosecond electrical transients", *IEEE Journal of Quantum Electronics*, vol. 24, pp. 184-197, 1988

[24] Van Exter et al, "Characterization of an Optoelectronic Terahertz Beam System", *IEEE Transaction on Microwave Theory and Techniques*, vol. 38, no. 11, pp. 1684-1691, 1990

[25] S. E. Ralph and D. Grischkosky, "Terahertz Beams: Generation and Spectroscopy", *Mat. Res. Soc. Symp. Proc.*, vol. 261, 1992, pp. 89-100, 1992

[26] B. B. Hu, and M. C. Nuss, "Imaging with terahertz waves", *Optics Letters*, vol. 20, no. 16, pp. 1716-1718, 1995

[27] I. Brener, Y. Cai, J. Lopata, J. Wynn, L. Pfeiffer, and J. Federici, "Singular Electric Field Terahertz Emitters and Detectors", *Ultrafast Electronics and Optoelectronics Conference, Technical Digest*, p54, Incline Village, Nevada, 1997

[28] I. Brener, Y. Cai, J. Lopata, J. Wynn, L. Pfeiffer, and J. Federici, "Design and Performance of Singular Electric Field Terahertz Emitters and Detectors", *Conference on Lasers and Electro-Optics / Quantum Electronics and Laser Science Conference, Technical Digest*, p66, Baltimore, Maryland ,1997

[29] Y. Cai, I. Brener, J. Lopata, J. Wynn, L. Pfeiffer, and J. Federici, "Design and Performance of Singular Electric Field Terahertz Photoconducting Antennas", *Applied Physics Letters*, October 13, 1997

[30] Y. Cai, I. Brener, J. Lopata, J. Wynn, L. Pfeiffer, and J. Federici, "Singular Electric Field Terahertz Emitters and Detectors", *Trends in Optics and Phtotonics Series volume*, Vol. 13, pp.237-240, 1997

[31] I. Brener, D. Dykaar, A. Frommer, L. N. Pfeiffer, J. Lopata, J. Wynn, K. West, and M. C. Nuss, *Optics Letters* 21, p.1924, 1996

[32] D. Krokel, D. Grischkowsky, and M. B. Ketchen, *Appl. Phys. Lett.* 54, p1046, 1989

[33] U. D. Keil, D. R. Dykaar, *IEEE Journal of Quantum Electronics* 32, p1664, 1996

[34] Stephen E. Ralph, and D. Grischkowsky, *Appl. Phys. Lett.* 59, p1972, 1991

[35] E. Budiarto, J. Margolies, S. Jeong, J. Son and J. Bokor, *IEEE Journal of Quantum Electronics.* 32, p1839, 1996

[36] E. Sano and T. Shibata, *Appl. Phys. Lett.* 55, p2748, 1989

[37] Q. Wu, X. C. Zhang, *Appl. Phys. Lett.* 68, p1604, 1996

[38] The experimental error for the THz average power calibration is estimated to be under 50%. It is primarily determined by the accuracy of the THz spot size measurement at the focal point.

[39] M. V. Exter and D. Grischkowsky, *IEEE Transaction on Microwave and Techniques* 38, p1684, 1990

[40] I. Brener, Q. Wu, Y. Cai, X. C. Zhang, J. Lopata, J. Wynn, L. Pfeiffer, J. Stark, and J. Federici, "Coherent Terahertz Detection: Free Space Eletric-optic Sampling versus antennas detection", *Conference on Lasers and Electro-Optics / Quantum Electronics and Laser Science Conference, Technical Digest*, p136, Baltimore, Maryland, 1997

[41] X. Zhou, S. Alexandrou, and T. Y. Hsiang, "Monte Carlo investigation of the intrinsic mechanism of subpicosecond pulse generation by nonuniform gap illumination." *J. Appl. Phys.*, vol. 77, pp. 706-711, 1995

[42] X. Zhou, S. Alexandrou, and T. Y. Hsiang, "Monte Carlo investigation of the intrinsic mechanism of subpicosecond pulse generation by nonuniform gap illumination." In 1994 *Conf. Laser and Electro-Optics (CLEO'94)*, Anaheim, CA, May, paper CThI20, 1994

[43] X. Zhou, "On the physics of femto-second electrical pulse generation in transmission-line gaps." *Optoelectronics-Devices and Technologies*, vol. 10, pp.491-504, 1995

[44] X. Zhou, "Numerical physics of subpicosecond electrical pulse generation by nonuniform gap illumination." *IEEE Journal of Quantum Electronics*, vol. 32, p1672, 1996

[45] G. Rodriguez, S. R. Caceres, and A. J. Taylor, " Modeling of terahertz radiation from biased photoconductors: transient velocity effects", *Optics Letters*, vol. 19, p1994, 1994

[47] E. Sano and T. Shibata, "Fullwave analysis of picosecond photoconductive switches" *IEEE Journal of Quantum Electronics*, vol. 26, pp.372-377, 1990

[48] X. C. Zhang, B. B. Hu, J. T. Darrow, and D. H. Auston, *Appl. Phys. Lett.* 56, 1011, 1990

[49] X. X. Zhang, J. T. Darrow, B. B. Hu, D. H. Auston, M. T. Schmidt, P. Tham, and E. S. Yang, *Appl. Phys. Lett.* 56, 2228, 1990

[50] B. I. Greene, J. F. Federici, D. R. Dykaar, A. F. J. Levi, and L. N. Pfeiffer, *Opt. Lett.* 59, 893, 1991

[51] B. I. Greene, J. F. Federici, D. R. Dykaar, R. R. Jones, and P. H. Bucksbaum, *Appl. Phys. Lett.* 59, 893, 1991

[52] S. L. Chuang, S. Schmitt-Rink, B. I. Greene, P. N. Saeta, and A. F. J. Levi, "Optical Rectification at Semiconductor Surfaces", *Physical Review Letters*, vol. 68, p102, 1992

[53] S. Hunsche, M. Koch, I. Brener, and M. C. Nuss, *Trends in Optics and Photonics Series volume*, Vol. 13, p233, 1997

[54] D. B. Rutledge, D. P. Neikirk, and D. P. Kasilingam, in *Infrared and Miliilmeter Waves*, edited by K. J. Button, Academic, New York, Vol. 10, Ch.1, 1983

[55] R. D. Grober, R. J. Schoelkopf, and D. E. Prober, *Appl. Phys. Lett.*, 70, p1354, 1997

[56] A. J. Lochtefeld, M. R. Melloch, J. C. P. Chang and E. S. Harmon, *Appl. Phys. Lett.* 69, p1465, 1996

[57] Z. Liliental-Weber, H. J. Cheng, S. Gupta, J. Whitaker, K. Nichols and F. W. Smith, *Journ. Electr. Mat.* 22, p1465, 1993

[58] M. R. Melloch, J. M. Woodall, N. Otsuka, K. Mahalingam, C. L. Chang and D. D. Nolte, *Materials Science and Engineering* B22, p31, 1993

[59] W. Lukosz and R. E. Kunz, "Light emission by magnetic and electric dipoles close to a plane interface. I. Total radiation power," *J. Opt. Soc. Amer.*, vol 67, p. 1067, 1977

[60] C. Fattinger and D. Grishkowsky, "Beams of terhertz electro-magnetic pulses," in Proc. *Picosecond Electronics and Optoelectronics Topical Meeting (Salt Lake City, UT)*, Mar. 8-10, p. 225, 1989

[61] D. B. Rutledge and M. S. Muha, " Imaging antenna arrays," *IEEE Tran. Antennas Propagat.*, vol. 67, p. 1067, 1977

[62] G. D. Monteath, *Applications of the Electromagnetic Reciprocity Principle*. Oxford: Pergamon Press, 1973

[63] Q. Wu, and X. C. Zhang, "7 THz bandwidth GaP electro-optic sensor", *Appl. Phys. Lett.*, 70, p1784, 1997

[64] Q. Wu, M. Litz, and X. C. Zhang, *Appl. Phys. Lett.* 68, p2924, 1996

[65] Q. Wu, and X. C. Zhang, "Free-space electro-optic sampling of mid-infrared pulses", *Appl. Phys. Lett.*, 71, p1285, 1997

[66] Q. Wu, and X. -C. Zhang, "Design and characterization of traveling-wave electro-optic THz sensors", *IEEE Jornal of Selected Topics in Quantum Electronics on Ultrafast Electronics, Photonics, and Optoelectronics*, 2, p693, 1996

[67] S. Gupta, M. Y. Frenkel, J. A. Valdmanis, J. F. Whitaker, F. W. Smith and A. R. Calawa, *Appl. Phys. Lett.* 59, p3276, 1991

[68] B. Nabet, A. Youtz, F. Castro, P. Cooke and A. Paolella, *Appl. Phys. Lett.* 67, p1748, 1995

[69] Y. Kostoulas, L. J. Waxer, I. A. Walmsley, G. W. Wicks and P. M. Fauchet, *Appl. Phys. Lett.* 66, p1821, 1995

[70] S. S. Prabhu, S. E. Ralph, M. R. Melloch, and E. S. Harmon, "Carriers dynamics of low temperature grown GaAs observed via Terahertz spectroscopy", *OSA Trends in Optics and Photonics on Ultrafast Electronics and Optoelectronics*, vol.13, Martin Nuss and John Bowers (ed.), 1997

[71] S. H. Patel and M. Xanthos, "Volatile emission during thermoplastics processing", *Advances in Polymer Tech.* 14, p67, 1995

[72] S. Vijayalakshmi, H. Grebel, J. F. Federici, A. M. Johnson, *Quantum Electronics and Laser Science Conference*, QThG48, Baltimore, Maryland, 1997

[73] Max Born, and Emil Wolf, *Principles of Optics*, Pergamon Press, pp.584-590, 1980

[74] Y. Cai, I. Brener, Q. Wu, X. C. Zhang, J. Lopata, J. Wynn, L. Pfeiffer, J. Stark, and J. Federici, "Direct Comparison Between Free Space Electro-Optic Sampling and Antenna Detection", *Applied Physics Letters*, (submitted)

[75] S. Hunsche, Y. Cai, I. Brener, M. C. Nuss, J. Wynn, J. Lopata, and L. Pfeiffer, "Near field time-resolved imaging with far-infrared dipole sources", *Conference on Lasers and Electro-Optics Conference*, California, 1998 (submitted)

[76] S. Alexandrou, C.-C. Wand, R. Sobolewski, and T. Y. Hsiang, " Generation of subpicosecond electrical pulses by nonuniform illumination of GaAs transmission-lin gaps," *IEEE Journal of Quantum Electronics*, vol. 30, pp.1332-1338, 1994